Development of Liquid Phase Sintering Technique with Sm-based Alloy Binder for $Sm_2Fe_{17}N_3$ Permanent Magnets

Sm 基合金を使用した液相焼結による $Sm_2Fe_{17}N_3$ 永久磁石作製方法の開発

April 2018

Waseda University

Graduate School of Advanced Science and Engineering

Department of Advanced Science and Engineering

Research of Life Science and Medical Bioscience

Kohei OTOGAWA

乙川　光平

Contents

Chapter3 Magnetic Properties of Sm-based Alloy Binder Added $Sm_2Fe_{17}N_3$ Sintered Magnets

Chapter 4 Development of Sintering Process to Maximize the Potential of the Sm-based Alloy Binder for Improvement of the Magnetic Properties of $Sm_2Fe_{17}N_3$ Compacts

Chapter 1

General Introduction

1.1 Necessity of high-performance permanent magnets

Many permanent magnets had been developed so far and many of them were developed by Japanese researchers, for example, the KS steel by Honda *et al*. (1917) , the MS steel by Mishima *et al*. (1931), the ferrite magnet by Takei *et al*. (1933), the Fe-Cr-Co by Kaneko *et al*. (1971), the Sm_2Co_{17} by Tawara *et al*. (1975), the $Nd_2Fe_{14}B$ by Sagawa *et al*. (1983) and the $Sm_2Fe_{17}N_3$ by Iriyama *et al*. (1987) [1,2]. Permanent magnets were mounted in various devices, for example, speaker, magnetron of microwave oven, magnetic field generator of magnetic resonance imaging apparatus, driving motor and so on. In particular, the main use of the permanent magnet is in the driving motor, since approximately 60% of electric energy is consumed to drive the motors in Japan, and the mainstream structure of the driving motor is an interior permanent magnet (IPM) motor. Therefore, the improvement of the magnetic properties of the permanent magnet gives remarkable influence on the improvement of efficiency of the driving motor. Namely, the development of the high-performance permanent magnet will significantly contribute to energy saving. In addition, the electric vehicle and hybrid electric vehicle that mount IPM motors as driving source has been extensively developed and thus, the demand of the high-performance permanent magnet is expected to increase.

1.2 Technical terms of magnetism

The parameters that characterize the permanent magnet are defined using magnetization curve with a field hysteresis (Fig. 1.1). If magnetic field (H) is applied to a magnet, magnetic moments (m) of each atom in the magnet tend to be aligned to the same direction. The sum of the magnetic moments per unit volume is defined as magnetization (M). Magnetic polarization (J) is defined as the product of M and permeability of vacuum (μ_0). The value of magnetization is defined as saturation magnetization (M_s) and that of magnetic polarization is defined as saturation polarization (J_s) where all the magnetic moments are completely aligned to same direction. The value of the magnetization when the applied magnetic field is zero is defined as residual magnetization or remanence (M_r). A characteristic of ferromagnets is a finite residual magnetization. When temperature increases, the ferromagnet loses its residual magnetization, and becomes paramagnetic. This phase transition temperature is defined as the Curie temperature (T_C). The value of the applied magnetic field where magnetization becomes zero in the hysteresis loop is defined as coercivity (H_{cj}). Magnetic flux density (B) is defined as $B=M+\mu_0 H$. The efficiency of the permanent magnet is evaluated by the maximum energy product ((BH)$_{max}$) which is the maximum value of the product of B and H on the B-H curve. The theoretical maximum value of (BH)$_{max}$ is $M_s^2/4\mu_0$.

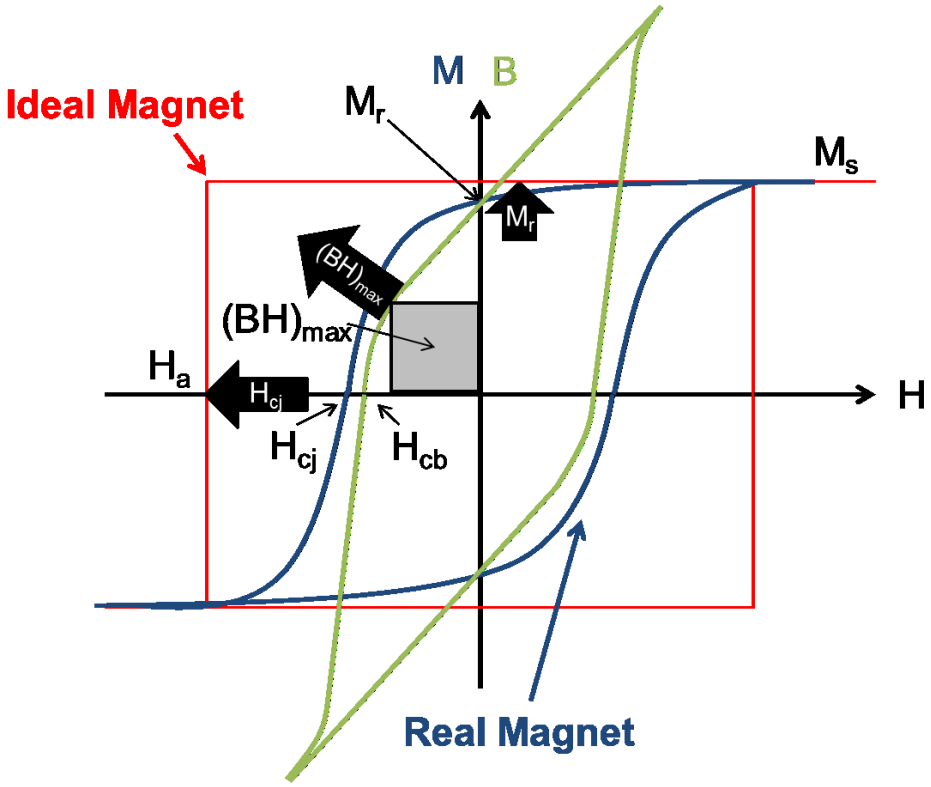

Figure 1.1 Magnetization curve of permanent magnet

To put permanent magnets into practical use in driving motor magnets, two issues are important. The first is the improvement of remanence. For this purpose, enhancing the saturation magnetization, improving the crystal orientation, and enhancing the density of the magnetic phase are performed. The second is the improvement of coecivity. For this purpose, enhancing the anisotropy field (H_a), the refinement of the grain size, rounding the grain shape, and controlling the grain boundary layer are performed. Note that anisotropy field is defined as the value of the applied magnetic field to saturate the magnetization of uniaxial magnetic anisotropy compound along its magnetization hard-axis.

It is known that both the SI unit system and cgs Gaussian unit system are commonly used. In this thesis, Gaussian unit system is mainly used, but in some cases, SI unit system is used when the data in the literature are referred. Table 1.1 shows the unit conversion table.

Table 1.1 unit conversion table

unit name	unit symbol	SI unit	cgs unit (Gaussian unit)	cgs→SI
magnetic field	H	A/m	Oe	1[Oe]=$10^3/4\pi$[A/m]
magnetic flux density	B	T	G	1[G]=10^{-4}[T]
volume magnetization	M	A/m	emu/cm^3	1[emu/cm^3]=10^3[A/m]
mass magnetization	σ	(A・m^2)/kg	emu/g	1[emu/g]=10^3[(A・m^2)/kg]
maximum energy product	$(BH)_{max}$	J/m^3	G・Oe	1[G・Oe]=$10^{-1}/4\pi$[J/m^3]
magnetic permeability	μ	H/m	bare number	1[bare number]=$4\pi\times10^{-7}$[H/m]

1.3 Magnetic property and issue of rare-earth permanent magnets

Rare-earth permanent magnets mean permanent magnets made of ferromagnetic compounds that are composed of rare-earth elements and transition metal elements. As shown in Fig. 1.2, many high-performance ferromagnetic materials are composed of rare-earth elements and transition metal elements. In general, transition metal elements show high Curie temperatures but low anisotropy fields, whereas rare-earth elements generally show low Curie temperatures but high anisotropy fields. Therefore, intermetallic compounds made of these two kinds of elements can be high-performance permanent magnets that have high Curie temperatures and high anisotropy fields. The properties of the representative rare-earth permanent magnets are described below.

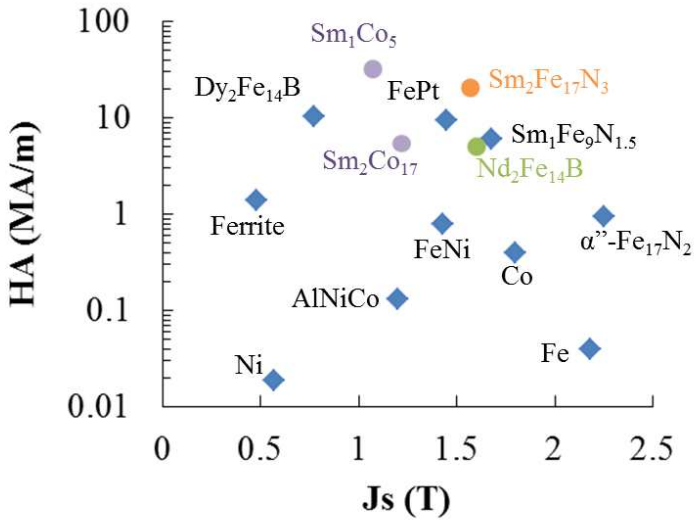

Figure1.2 Saturation magnetization and anisotropy field of ferromagnetic materials.

1.3.1 $Nd_2Fe_{14}B$ magnet

$Nd_2Fe_{14}B$ magnet was firstly reported by Sagawa *et al*. in 1983 [3]. The $Nd_2Fe_{14}B$ sintered magnet is the most high-performance magnet at present. For $Nd_2Fe_{14}B$, J_s=1.61[T], T_C=585[K] and H_a=8[T]. General production procedure of the $Nd_2Fe_{14}B$ magnet is as

follows: First, molten Nd-Fe-B metal is rapidly quenched by a strip casting method. Its metallographic structure is fine and precipitation of primary α-Fe phase did not present. The rapid quenching alloy is coarsely ground using a hydrogen grinding method. The coarse powder is further pulverized into few micrometer fine grains by a ball milling method or jet milling method. This fine powder is pressed in a magnetic field and a highly crystal orientated green compact is prepared. The green compact is sintered in inert atmosphere and dense bulk magnet is obtained. Finally, this sintered magnet is annealed. This annealing process maximizes the magnetic property because it controls a structure of boundary layer. The highest $(BH)_{max}$ of 59 MGOe with B_r = 1.56 [T] and H_{cj} = 8.2 [kOe] has been reported [4]. However, the coercivity of the $Nd_2Fe_{14}B$ magnets drastically decreases down to 2 kOe at 200 ˚C, which is the operation temperature of the driving motor for EV [5]. Therefore, pure $Nd_2Fe_{14}B$ cannot be put to practical use, but Dy-doped $Nd_2Fe_{14}B$ sintered magnets were mounted in driving motors for EV. $Dy_2Fe_{14}B$ shows large H_a of 16T [6], and thus partial substitution of Dy for Nd increases the coercivity of the $Nd_2Fe_{14}B$ sintered magnet. Accordingly, the Dy-doped $Nd_2Fe_{14}B$ sintered magnet shows high heat resistance. However, Dy doping causes a decrease in the magnetization because the magnetic moment of the Fe atom and that of the Dy atom couples antiferromagnetically. Therefore, 8% Dy-doped $Nd_2Fe_{14}B$ is the optimized composition, and the sintered magnets with this composition are mounted in the driving motor for EV at present. However, this 8% Dy-doped $Nd_2Fe_{14}B$ sintered magnet shows coercivity of 8 kOe at 200 ˚C [7]. However Dy is a rare element and more than 90% of Dy is produced in China. In 2011, the price of Dy was drastically increased owing to the change in China's policy, as shown in Fig. 1.3 [8]. Accordingly, a Dy-free permanent magnet with high heat resistance is desired. The $(BH)_{max}$ of a Dy-free hot-deformed $Nd_2Fe_{14}B$ permanent magnet reaches 24 MGOe at 200 ˚C which is comparable to 8% Dy-doped $Nd_2Fe_{14}B$ sintered magnet [5]. However, its coercivity is only 5kOe at 200 ˚C and further improvement is necessary.

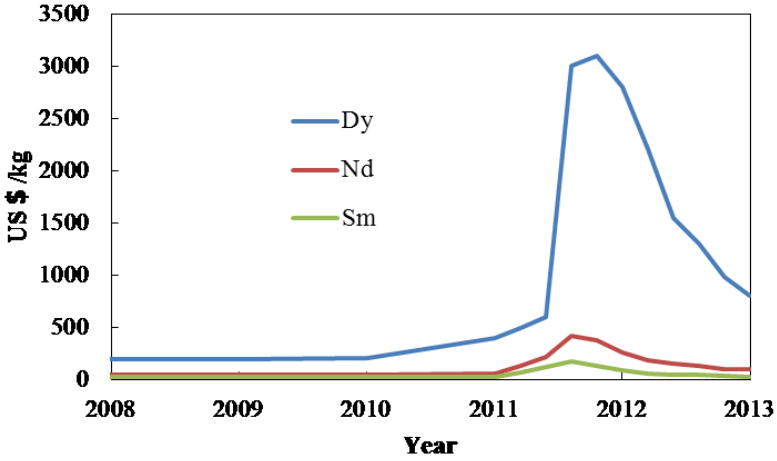

Figure 1.3 Price trends of Dy, Nd and Sm [8].

1.3.2 Sm-Co type magnet

There are $SmCo_5$ and Sm_2Co_{17} among Sm-Co type magnets. For $SmCo_5$, J_s=1.07[T], T_C=1020[K] and H_a=40[T] [9,10]. H_a of $SmCo_5$ is the largest among the existing rare-earth magnetic materials. In addition, since T_C of $SmCo_5$ is relatively high, it shows higher heat resistance than $Nd_2Fe_{14}B$. However, $(BH)_{max}$ of $SmCo_5$ is relatively small because of its low saturation magnetization.

Sm_2Co_{17} was developed to increase the magnetization by increasing the amount of Co and replacing a part of Co by Fe. For Sm_2Co_{17}, J_s=1.22[T], T_C=1190[K] and H_a=7[T]. The single-phase Sm_2Co_{17} magnet does not have high coercivity because of its low H_a. However, it was found that the doping of Cu and Zr increases the coercivity of the Sm_2Co_{17} sintered magnet, and $Sm(Co,Fe,Cu,Zr)_z$ magnet has been developed, where Fe is doped to enhance the magnetization, whereas Cu and Zr are doped to enhance the coercivity. As a result, the $Sm(Co,Fe,Cu,Zr)_z$ magnet shows high heat resistance and good magnetic properties of B_r=1.12[T], H_{cj}=13[kOe] and $(BH)_{max}$=33[MGOe][11,12]. The $Sm(Co,Fe,Cu,Zr)_z$ magnet is produced through multistage annealing processes with severe controlled temperature. This

complicated annealing process induces a characteristic microstructure, where 100nm of Sm_2Co_{17} grains are surrounded with the 4-5nm thickness of $SmCo_5$ layers [13,14]. The magnetic wall energies of the Sm_2Fe_{17} phase and the $SmCo_5$ phase are greatly different. This difference of the magnetic wall energy traps the magnetic domain wall moving at the grain boundary. This trapping of the magnetic domain wall improves the coercivity of $Sm(Co,Fe,Cu,Zr)_z$ magnet. This coercivity mechanism is called as a pinning model. As shown above, the coercivity of the sintered magnet is dominated by its microstructure. Further development of Sm_2Co_{17} type magnet is in progress to improve its magnetic properties.

1.3.3 $Sm_2Fe_{17}N_3$ magnet

$Sm_2Fe_{17}N_3$ was firstly reported in 1987 by Iriyama *et al*. [15,16]. For $Sm_2Fe_{17}N_3$, J_s=1.54[T], T_C=749[K] and H_a=26[T]. The saturation magnetization of $Sm_2Fe_{17}N_3$ is comparable to that of Nd-Fe-B (1.61T), and the anisotropy field and the Curie temperature are higher than the values of Nd-Fe-B (H_a; 8T and T_C; 585K) [3]. As shown in Fig. 1.4, even if achieved $(BH)_{max}$ of the $Sm_2Fe_{17}N_3$ magnet is only 64% of the theoretical maximum value, it is higher than that of Dy-doped $Nd_2Fe_{14}B$ sintered magnet at 200 ˚C. Therefore, it is expected that $Sm_2Fe_{17}N_3$ magnet can be a substitute for the Dy-doped $Nd_2Fe_{14}B$ sintered magnet.

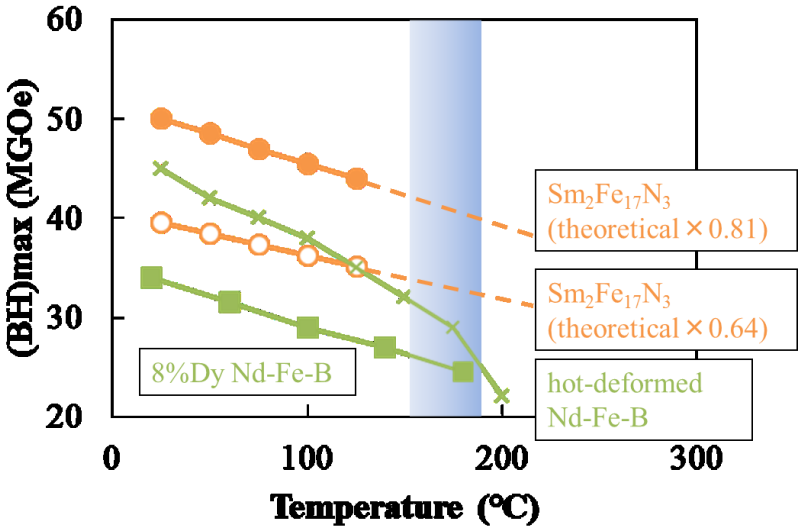

Figure 1.4 Dependence of $(BH)_{max}$ on the temperature.

However, at present, only resin-bonded $Sm_2Fe_{17}N_3$ magnet is put into practical use [17]. Although the resin-bonded magnet has flexibility in shape and high mechanical strength, the resin cannot tolerate high temperatures and the relative density of the magnetic phase is inevitably lower than that of the sintered magnet. Therefore, the resin-bonded $Sm_2Fe_{17}N_3$ magnet is not suitable for the magnet in the driving motor for EV.

Hence, the realization of the sintered $Sm_2Fe_{17}N_3$ magnet is desired. However, the $Sm_2Fe_{17}N_3$ sintered magnet with the sufficient exploitation of its potential has not been developed because of difficulties in the sintering process [18–21]. There are two major obstacles in sintering the $Sm_2Fe_{17}N_3$ powders. The first obstacle is the irreversible thermal decomposition of the $Sm_2Fe_{17}N_3$ phase. $Sm_2Fe_{17}N_3$ is easily decomposed into α-Fe and Sm-N around 620 ˚C and the magnetic properties disappears accordingly [22–24]. Therefore, a low-temperature sintering process is indispensable for producing the sintered magnets of this material. Many researchers have tried various low-thermal-load consolidation methods, such as the shock compaction method [25–27], compression shearing method [28], spark plasma sintering method [29–31] and others [32,33]. However, all of them caused a decrease

in coercivity even below the decomposition temperature of $Sm_2Fe_{17}N_3$, which is the second obstacle. A previous report [34] proposed the following mechanism for the suppression in coercivity. Commonly available $Sm_2Fe_{17}N_3$ powders naturally have surface oxide layers because of the exposure to air. When these $Sm_2Fe_{17}N_3$ powders are sintered, a redox reaction occurs between the primary $Sm_2Fe_{17}N_3$ phase and the iron oxide in the surface oxide layer, resulting in the precipitation of the α-Fe phase on the grain surface even below 620 ˚C. The α-Fe precipitation causes a severe decrease in coercivity because the α-Fe precipitate acts as the nucleation site of the reverse magnetic domain. Based on this mechanism, Soda *et al*. [35] demonstrated that a low oxygen sintering process with surface-oxide-free $Sm_2Fe_{17}N_3$ powder can produce the sintered magnet with maintaining the coercivity of the raw powder. However this process still needs to be improved because it is difficult to densify the magnetic phase by the solid phase sintering at such a low temperature below 620 ˚C. Therefore, to produce the ideal $Sm_2Fe_{17}N_3$ magnet, both densification of the magnetic phase by low-thermal-load consolidation process and overcoming of the serious decrease in coercivity caused by the surface oxide layers have to be simultaneously achieved.

1.4 Liquid phase sintering

In this section, it is proposed that liquid phase sintering is promising process to simultaneously achieve densification of $Sm_2Fe_{17}N_3$ grains by low-thermal-load consolidation process and overcoming the serious decrease in coercivity caused by the surface oxide layers. At first, to show a reason of this proposal, a progress of classic liquid phase sintering and an effect of liquid phase sintering of the $Nd_2Fe_{14}B$ sintered magnets are mentioned below.

1.4.1 Classic liquid phase sintering

A classic liquid phase sintering densifies a raw material through three overlapping stages [36]. Fig. 1.5 shows schematic sequence of steps. Initially, the additive-mixed powders are heated to a temperature where an additive-liquid forms. Immediately, rapid initial densification is progressed owing to rearrangement by the capillary force exerted from the wetting liquid on the solid particles (Stage 1). In case of low wettability of liquid additive on the solid grain, the compact is swelled adversely.

As densification by rearrangement slows, effects of solubility and diffusivity become dominant. This second stage is termed solution-reprecipitation (Stage 2). A general property of solution-reprecipitation processes is microstructural coarsening. The solubility of a grain in additive-liquid varies inversely with the grain size; small grains have a higher solubility than coarse grains. The difference of solubility establishes a concentration gradient in the liquid. Main phase material is transported from the small grains to the large grains by diffusion. This process is termed Ostwald ripening. Ostwald ripening relaxes the shape of grains and densification is progressed accordingly. Note that, if the liquid solubility in the solid is higher than the solid solubility in the liquid, pores are generated in liquid phase and compact is swelled accordingly. These pores are termed Kirkendall voids.

The last stage of classic liquid phase sintering is termed solid state controlled sintering (Stage 3). At this stage, the grain size is grown and the grain contact causes solid state

sintering. In addition, when insoluble gasses are trapped in the compact, the compact is swelled due to growth of the pores. This swelling is restrained by vacuum condition sintering process or pressure sintering process.

As shown above, to promote the densification by the classic liquid phase sintering, high wettability of the liquid additive on the solid grain, appropriate solubility and appropriate sintering process is important.

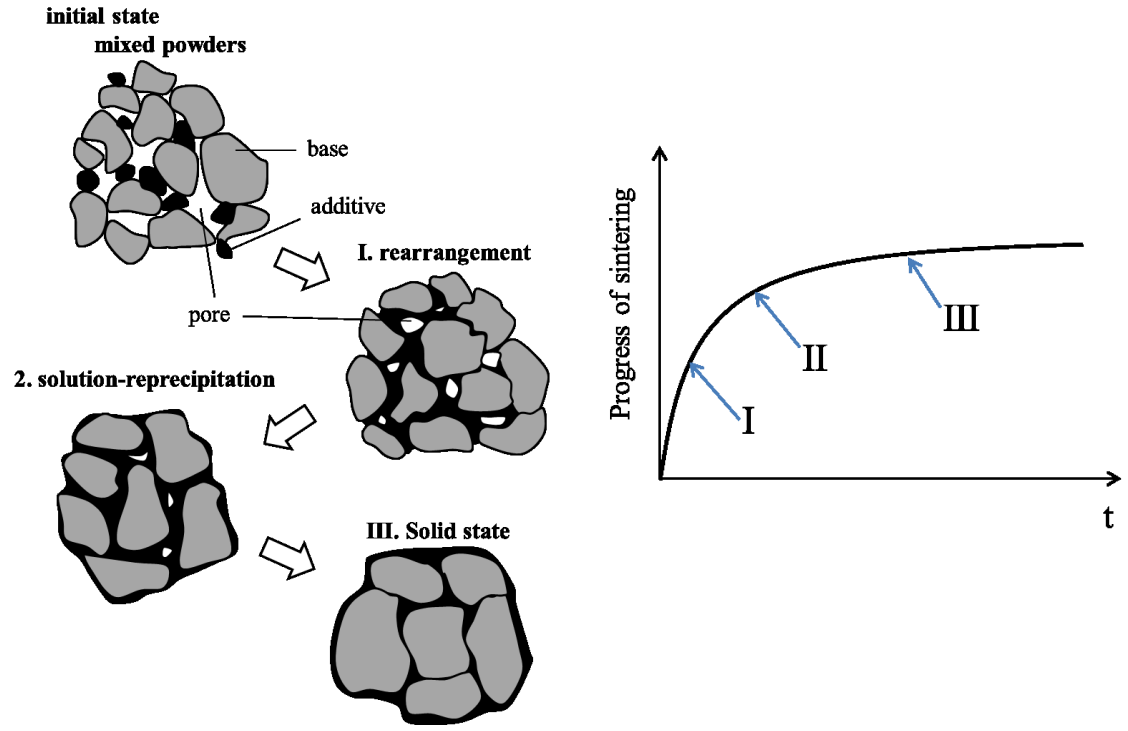

Figure 1.5 The progress of classic liquid phase sintering [36].

1.4.2 Liquid phase sintering of $Nd_2Fe_{14}B$

Liquid phase sintering phenomenon is occurred while sintering of $Nd_2Fe_{14}B$ [3]. It is different from classic liquid phase sintering but is supersolidus sintering which is a kind of special technique of liquid phase sintering. The major difference between the supersolidus sintering and the classic liquid phase sintering is the use of liquid phase from inside of the particle instead of liquid phase of the additive. The raw $Nd_2Fe_{14}B$ powders include Nd-rich

phase. The melting point of $Nd_2Fe_{14}B$ and Nd-rich phase are 1155 and 665 ˚C, respectively [37]. Therefore, liquid Nd-rich phase is exuded from inside of $Nd_2Fe_{14}B$ when the raw powder is heated. This permeated liquid phase promotes densification of powders as classical liquid phase sintering. In addition, the liquid Nd-rich phase removes oxide layers of grain surface and concentrate oxides at grain boundary triple junctions [38]. Furthermore, Nd-rich grain boundary layer is composed after sintering and it act as pinning site. As a result, coercivity of $Nd_2Fe_{14}B$ sintered magnet is improved by Nd-rich phase [39,40].

1.4.3 Previous metal bonded $Sm_2Fe_{17}N_3$ magnet

The above facts strongly support the proposal that liquid phase sintering of $Sm_2Fe_{17}N_3$ is expected to simultaneously achieve densification of $Sm_2Fe_{17}N_3$ grains by low-thermal-load consolidation process and overcoming the serious decrease in coercivity caused by the surface oxide layers. Naturally, supersolidous sintering is hard to be realized for $Sm_2Fe_{17}N_3$, because its solidus temperature is higher than the thermal decomposition temperature. Therefore, the classic liquid phase sintering using low-melting point alloy as additive is expected to be suitable. So far some researchers have tried sintering $Sm_2Fe_{17}N_3$ with various metal binders, but only sintering using a Zn binder has been successful in producing worthful high-coercive sintered magnets [2,41–53]. Zn was able to be melted below the decomposition temperature of $Sm_2Fe_{17}N_3$, and wet spread on the surface of the $Sm_2Fe_{17}N_3$ particles. A part of the Fe atoms in the $Sm_2Fe_{17}N_3$ main phase are replaced by Zn, and nonmagnetic Sm-Fe-Zn-N phases are then formed at the grain boundary. The literature [49] presumed that this Zn replacement might recover the anisotropic field of the grain surfaces because of removal of surface defects which cause nucleation sites. In addition, the grain boundary Sm-Fe-Zn-N phases might reduce exchange coupling between the $Sm_2Fe_{17}N_3$ grains. These mechanisms were considered to be the reason for improvement of coercivity. However, Zn addition also posed excess reduction of saturation magnetization: the reduction

ratio of saturation magnetization was approximately twice as much as the Zn addition ratio [48]. This reduction of saturation magnetization causes reduction of remanence. As a result, $(BH)_{max}$ of the Zn-bonded $Sm_2Fe_{17}N_3$ magnet is inevitably lower than that of ideal $Sm_2Fe_{17}N_3$ metal-bonded magnet which surpasses that of $Nd_2Fe_{14}B$ sintered magnet.

1.4.4 Requirement for additive alloy to take place ideal liquid phase sintering of $Sm_2Fe_{17}N_3$

This study proposes using Sm-based eutectic alloy as a sintering additive for $Sm_2Fe_{17}N_3$ magnet. Requirements for additive alloy to take place ideal liquid phase sintering of $Sm_2Fe_{17}N_3$ are considered as following (Table 1.2). First requirement is that liquid phase is formed below 620 ˚C which is decomposition temperature of $Sm_2Fe_{17}N_3$. As shown in Table 1.3, some Sm-based binary eutectic alloys satisfy this requirement [54]. Second requirement is that liquid phase can dissolve $Sm_2Fe_{17}N_3$. This requirement is needed to improve relation density of magnetic phase by solution-reprecipitation processes. Sm atoms of $Sm_2Fe_{17}N_3$ are naturally dissolved into Sm-based alloy liquid. Fe atoms of $Sm_2Fe_{17}N_3$ are also dissolved into Sm-based alloy liquid because Fe and Sm are took place eutectic reaction. Therefore, Sm-based eutectic alloys satisfy this requirement. Third requirement is that liquid phase can remove the oxide layers of $Sm_2Fe_{17}N_3$ grain surface. This requirement is necessary to restrain coercivity decrease during sintering. As shown in Fig. 1.6, reducing power of Sm is higher than that of Fe. Hence, Sm-based alloys are expected to satisfy this requirement. Fourth requirement is that Sm-based alloy liquid has good wettability with the $Sm_2Fe_{17}N_3$ grain surface. This requirement is necessary to permeate the liquid into grain boundary. Sm-based alloys are intuitively expected to have good wettability with the $Sm_2Fe_{17}N_3$ grain surface because Sm is a constituent element of $Sm_2Fe_{17}N_3$. The final requirement is that the liquid solubility in the solid is lower than the solid solubility in the liquid. This requirement is preferable to avoid generation of Kirkendall voids. It is difficult to predict whether

Sm-based alloys satisfy this requirement but it might be possible to satisfy this requirement by adjusting its composition. From the above reasons, Sm-based eutectic alloys are expected to be an ideal sintering additive for $Sm_2Fe_{17}N_3$ magnet.

Table 1.2 Requirements for additive alloy to take place liquid phase sintering of $Sm_2Fe_{17}N_3$.

Requirement for liquid phase sintering	Previous report	Sm-based eutectic alloy
Liquid phase is formed below decomposition temperature(<620℃)	○ Zn,Sn etc.	○ SmCu, SmNi etc.
Liquid phase can dissolve $Sm_2Fe_{17}N_3$	△ Zn react with main phase	○
Liquid phase can remove oxide layer	×	○?
Good wettability	○	○?
Appropriate solubility	△	○?

Table 1.3 Eutectic point of Sm-based binary alloys [54].

	Eutectic point
Sm-Fe	720 ˚C
Sm-Cu	555 ˚C
Sm-Ni	572 ˚C
Sm-Co	590 ˚C
Sm-Zn	670 ˚C
Sm-Ag	675 ˚C
Sm-Al	700 ˚C

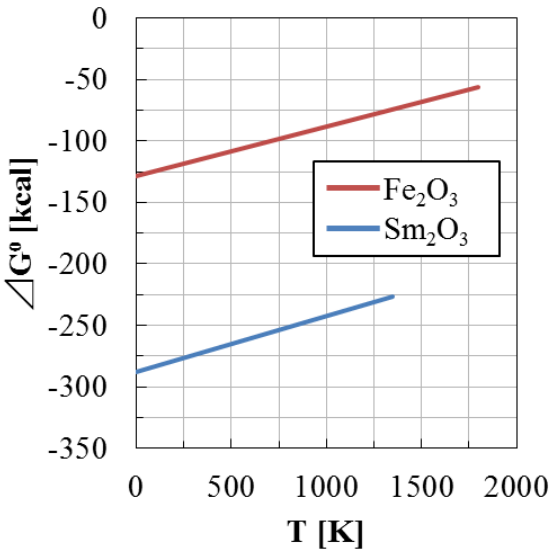

Figure 1.6 Ellingham diagrams of Fe_2O_3 and Sm_2O_3.

1.5 Scope of the thesis

The purpose of this thesis is explore the new sintering process using Sm-based eutectic alloy as additive which is capable of preventing the coercivity decrease during sintering as well as facilitating sintering densification due to the same effect as liquid phase sintering. This research is expected to promote the development of Dy-free high-performance permanent magnet which surpasses Dy-doped $Nd_2Fe_{14}B$ sintered magnet.

In the second chapter, low-melting point Sm-based eutectic alloy for sintering binder was explored. In the third chapter, $Sm_2Fe_{17}N_3$ bulk magnet using developed Sm-based alloy as binder was produced and its magnetic properties were measured. In the fourth chapter, an approach to maximize the potential of the developed Sm-based binder for the magnetic properties of $Sm_2Fe_{17}N_3$ magnet is discussed. In the fifth chapter, summary and future prospect were mentioned.

1.6 References

[1] M. Sagawa, M. Hamano, M. Hirabayasi, 永久磁石-材料科学と応用-, Agune Gijutsu Center, tokyo, 2007.

[2] T. Iriyama, Ph. D. Thesis, Tohoku University, 1994.

[3] M. Sagawa, S. Fujimura, N. Togawa, H. Yamamoto, Y. Matsuura, New material for permanent magnets on a base of Nd and Fe (invited), Journal of Applied Physics. 55 (1984) 2083–2087. doi:10.1063/1.333572.

[4] D. Harimoto, H. Matsuura, Hitachi Giho, 23 (2007) 69.

[5] T. Akiya, J. Liu, H. Sepehri-Amin, T. Ohkubo, K. Hioki, A. Hattori, K. Hono, High-coercivity hot-deformed Nd-Fe-B permanent magnets processed by Nd-Cu eutectic diffusion under expansion constraint, Scripta Materialia. 81 (2014) 48–51. doi:10.1016/j.scriptamat.2014.03.002.

[6] E.B. Boltich, E. Oswald, M.Q. Huang, S. Hirosawa, W.E. Wallace, E. Burzo, Magnetic characteristics of R2Fe14B systems prepared with high purity rare earths (R=Ce, Pr, Dy, and Er), Journal of Applied Physics. 57 (1985) 4106–4108. doi:10.1063/1.334633.

[7] http://www.hitachi-metals.co.jp/products/auto/el/pdf/nmx.pdf, (n.d.).

[8] http://www.neomag.jp/mag_navi/statistics/rare_earth_newprice2.html, (n.d.).

[9] J.J. Strnat, K., Hoffer, G., Olson, J., Ostertag, W. & Becker, A family of new cobalt base permanent magnet materials, J. Appl. Phys. 38 (1967) 1001–1002.

[10] E. Lectard, C.H. Allibert, Saturation phases magnetization and anisotropy fields in the Sm (Col -xCux) 5, 75 (1994) 6277–6279.

[11] Y. Tawara, K. Strnat, Rare earth-cobalt permanent magnets near the 2–17 composition, IEEE Transactions on Magnetics. 12 (1976) 954–958. doi:10.1109/TMAG.1976.1059138.

[12] A.E. Ray, Metallurgical behavior of Sm(Co,Fe,Cu,Zr)z alloys, Journal of Applied

Physics. 55 (1984) 2094–2096. doi:10.1063/1.333575.

[13] W. Tang, A.M. Gabay, Y. Zhang, G.C. Hadjipanayis, H. Kronmuller, Temperature dependence of coercivity and magnetization reversal mechanism in Sm(Co bal Fe 0.1 Cu y Zr 0.04)7.0 magnets, IEEE Transactions on Magnetics. 37 (2001) 2515–2517. doi:10.1109/20.951220.

[14] X.. Xiong, T. Ohkubo, T. Koyama, K. Ohashi, Y. Tawara, K. Hono, The microstructure of sintered Sm(Co0.72Fe0.20Cu0.055Zr0.025)7.5 permanent magnet studied by atom probe, Acta Materialia. 52 (2004) 737–748. doi:10.1016/j.actamat.2003.10.015.

[15] T. Iriyama, K. Kobayashi, N. Imaoka, T. Fukuda, H. Kato, Y. Nakagawa, Effect of nitrogen content on magnetic properties of Sm2Fe17Nx and SmFe5Ny alloys, IEEE Transactions on Magnetics. 28 (1992) 2587–2589. doi:10.1109/20.179565.

[16] J.M.D. Coey, H. Sun, Improved magnetic properties by treatment of iron-based rare earth intermetallic compounds in anmonia, Journal of Magnetism and Magnetic Materials. 87 (1990) 251–254. doi:10.1016/0304-8853(90)90756-G.

[17] K. Omori, T. Ishikawa, the 19th International Workshop on Rare Earth Permanent Magnets and Their Applications, in: Beijing, 2006: p. 221.

[18] M. Katter, J. Wecker, C. Kuhrt, L. Schultz, R. Grössinger, Magnetic properties and thermal stability of Sm2Fe17Nx with intermediate nitrogen concentrations, Journal of Magnetism and Magnetic Materials. 117 (1992) 419–427. doi:10.1016/0304-8853(92)90099-A.

[19] K. Kobayashi, Q. Qi, J.M.D. Coey, Magnetic properties of partially oxidized Sm 2Fe17 Nx, J Magn Magn Mater. 144 (1995) 1077–1078.

[20] C.N. Christodoulou, N. Komada, High coercivity anisotropic Sm2Fe17N3 powders, Journal of Alloys and Compounds. 222 (1995) 92–95. doi:10.1016/0925-8388(94)04924-6.

[21] K. Kobayashi, T. Iriyama, T. Yamaguchi, H. Kato, Y. Nakagawa, Magnetic properties of the single magnetic domain particles of Sm2Fe17Nx compounds, Journal of Alloys and Compounds. 193 (1993) 235–238. doi:10.1016/0925-8388(93)90357-S.

[22] D.T. Zhang, M. Yue, J.X. Zhang, Study on bulk Sm2 Fe17 Nx sintered magnets prepared by spark plasma sintering, Powder Metallurgy. 50 (2007) 215–218. doi:10.1179/174329007X169128.

[23] J.M.D. Coey, J.F. Lawler, H. Sun, J.E.M. Allan, Nitrogenation of R2Fe17 compounds: R=rare earth, Journal of Applied Physics. 69 (1991) 3007–3010. doi:10.1063/1.348614.

[24] K. Schnitzke, L. Schultz, J. Wecker, M. Katter, High coercivity in Sm2Fe17Nx magnets, Applied Physics Letters. 57 (1990) 2853–2855. doi:10.1063/1.104202.

[25] M. Leonowicz, W. Kaszuwara, E. Jezierska, D. Januszewski, Application of the shock compaction technique for consolidation of hard magnetic powders, Journal of Applied Physics. 83 (1998) 6634–6636. doi:10.1063/1.367580.

[26] T. Mashimo, X. Huang, S. Hirosawa, K. Makita, Y. Kato, S. Mitsudo, M. Motokawa, Magnetic properties of fully dense Sm2Fe17Nx magnets prepared by shock compression, Journal of Magnetism and Magnetic Materials. 210 (2000) 109–120. doi:10.1016/S0304-8853(99)00762-3.

[27] H. Oda, K. Kondo, H. Uchida, Y. Matsumura, S. Tachibana, T. Kawanabe, A samarium-iron nitride magnet fabricated by shock-compaction technique, Japanese Journal of Applied Physics. 34 (1995) L35–L37. doi:10.1143/JJAP.34.L35.

[28] T. Saito, M. Fukui, H. Takeishi, Sm-Fe-N bulk magnets produced by compression shearing method, Scripta Materialia. 53 (2005) 1117–1121. doi:10.1016/j.scriptamat.2005.07.025.

[29] K. Takagi, H. Nakayama, K. Ozaki, K. Kobayashi, Fabrication of High-performance SmFeN isotropic bulk magnets by a combination of High-pressure compaction and

current sintering, Journal of Magnetism and Magnetic Materials. 324 (2012) 1337–1341. doi:10.1016/j.jmmm.2011.11.035.

[30] T. Saito, Production of Sm-Fe-N bulk magnets by spark plasma sintering method, Journal of Magnetism and Magnetic Materials. 369 (2014) 184–188. doi:10.1016/j.jmmm.2014.06.034.

[31] D. V. Dudina, A.K. Mukherjee, Reactive spark plasma sintering: Successes and challenges of nanomaterial synthesis, Journal of Nanomaterials. 2013 (2013). doi:10.1155/2013/625218.

[32] B.P. Hu, X.L. Rao, J.M. Xu, G.C. Liu, Y.Z. Wang, X.L. Dong, D.X. Zhang, M. Cai, Magnetic properties of sintered Sm2Fe17Ny magnets, Journal of Applied Physics. 74 (1993) 489–494. doi:10.1063/1.355258.

[33] K. Machida, Y. Nakatani, G. Adachi, A. Onodera, High-pressure sintering characteristics of Sm2 Fe17 Nx powder, Applied Physics Letters. 62 (1993) 2874–2876. doi:10.1063/1.109186.

[34] K. Takagi, H. Nakayama, K. Ozaki, Microstructural behavior on particle surfaces and interfaces in Sm2Fe17N3 powder compacts during low-temperature sintering, Journal of Magnetism and Magnetic Materials. 324 (2012) 2336–2341. doi:10.1016/j.jmmm.2012.02.021.

[35] R. Soda, K. Takagi, M. Jinno, W. Yamaguchi, K. Ozaki, Anisotropic Sm2Fe17N3 sintered magnets without coercivity deterioration, AIP Advances. 6 (2016). doi:10.1063/1.4967364.

[36] Randall m. Germann, Liquid Phase Sintering, Springer Science+business media, New York, 1985.

[37] Y. Matsuura, S. Hirosawa, H. Yamamoto, S. Fujimura, M. Sagawa, K. Osamura, Phase diagram of the nd-fe-b ternary system, Japanese Journal of Applied Physics. 24 (1985) 635–637. doi:10.1143/JJAP.24.L635.

[38] T.T. Sasaki, T. Ohkubo, K. Hono, Structure and chemical compositions of the grain boundary phase in Nd-Fe-B sintered magnets, Acta Materialia. 115 (2016) 269–277. doi:10.1016/j.actamat.2016.05.035.

[39] T. Kohashi, K. Motai, T. Nishiuchi, S. Hirosawa, Magnetism in grain-boundary phase of a NdFeB sintered magnet studied by spin-polarized scanning electron microscopy, Applied Physics Letters. 104 (2014) 1–6. doi:10.1063/1.4883487.

[40] A. Sugawara, K. Ueda, T. Nakayama, N. Lee, H. Yamamoto, Measuring magnetisation reversal in micron-sized Nd2Fe14B single crystals by microbeam x-ray magnetic circular dichroism, Journal of Physics D: Applied Physics. 49 (2016) 1–7. doi:10.1088/0022-3727/49/42/425001.

[41] M. Endoh, M. Iwata, M. Tokunaga, Sm2(Fe,M)17Nx compounds and magnets, Journal of Applied Physics. 70 (1991) 6030–6032. doi:10.1063/1.350083.

[42] Y. Otani, A. Moukarika, H. Sun, J.M.D. Coey, E. Devlin, I.R. Harris, Metal bonded Sm2Fe17N3-δ magnets, Journal of Applied Physics. 69 (1991) 6735–6737. doi:10.1063/1.348900.

[43] K. Hiraga, K. Okamoto, T. Iriyama, Microstructure of Zinc-Bonded Sm2Fe17N3 Permanent Magnet Studied by Transimission and Analytical Electron Microscopy, Materials Transactions. 34 (1993) 569–571.

[44] M.Q. Huang, L.Y. Zhang, B.M. Ma, Y. Zheng, J.M. Elbicki, W.E. Wallace, S.G. Sankar, Metal-bonded Sm2Fe17-N-type magnets, Journal of Applied Physics. 70 (1991) 6027–6029. doi:10.1063/1.350082.

[45] P.A.P. Wendhausen, D. Eckert, A. Handstein, K.H. Müller, G. Leitner, R. Skomski, On the role of Zn in Sm2Fe17Nx permanent magnets, Journal of Applied Physics. 73 (1993) 6044–6046. doi:10.1063/1.353464.

[46] T.K. N. Imaoka, T. Iriyama, S. Itoh, A. Okamoto, Effect of Mn addition to Sm-Fe-N magnets on the thermal stability of coercivity, Journal of Alloys and Compounds. 222

(1995) 73–77.

[47] B. Wall, M. Katter, W. Rodewald, M. Velicescu, Dependence of the magnetic properties of Zn bonded Sm2Fe17Nx magnets on the particle size distribution, IEEE TRANSACTIONS ON MAGNETICS. 30 (1994) 675–677.

[48] K. Makita, S. Hirosawa, Coercivity of Zn evaporation-coated Sm2Fe17Nx fine powder and its bonded magnets, Journal of Alloys and Compounds. 260 (1997) 236–241. doi:10.1016/S0925-8388(97)00155-2.

[49] D. Prabhu, H. Sepehri-Amin, C.L. Mendis, T. Ohkubo, K. Hono, S. Sugimoto, Enhanced coercivity of spark plasma sintered Zn-bonded Sm-Fe-N magnets, Scripta Materialia. 67 (2012) 153–156. doi:10.1016/j.scriptamat.2012.04.001.

[50] K. Machida, K. Noguchi, M. Nishimura, G. Adachi, High-performance alloyed In metal-bonded magnets produced from ZnSm2Fe17Nx powders, Journal of Applied Physics. 87 (2000) 5317. doi:10.1063/1.373333.

[51] C. Kuhrt, K. O'Donnell, M. Katter, J. Wecker, K. Schnitzke, L. Schultz, Pressure-assisted zinc bonding of microcrystalline Sm2Fe 17Nx powders, Applied Physics Letters. 60 (1992) 3316–3318. doi:10.1063/1.106678.

[52] T. Saito, T. Deguchi, H. Yamamoto, Magnetic properties of Sm-Fe-N bulk magnets produced from Cu-plated Sm-Fe-N powder, AIP Advances. 7 (2017) 1–6. doi:10.1063/1.4973396.

[53] T. Saito, Magnetic properties of Sm-Fe-N anisotropic magnets produced by magnetic-field-assisted spark plasma sintering, Materials Science and Engineering B: Solid-State Materials for Advanced Technology. 167 (2010) 75–79. doi:10.1016/j.mseb.2010.01.032.

[54] H. Baker, H. Okamoto, ASM Alloy Phase Diagrams Database, ASM International. (2017). http://www.asminternational.org.

Chapter 2

Exploration of Sm-based Alloy for Sintering Binders

2.1 Introduction

As mentioned in Chapter 1, at first, low-melting point Sm-based eutectic alloy for sintering binder of $Sm_2Fe_{17}N_3$ have to be developed. Melting point of binder alloy was absolutely required below 620 ˚C which is the thermal decomposition temperature of $Sm_2Fe_{17}N_3$ [1–3]. Taking into account the tolerability of sintering temperature control, the desirable melting point should be below 500 ˚C, which is much lower than the thermal decomposition temperature. However, as far as I know, the lowest melting point among previously reported binary Sm alloys is 555 ˚C, which is the eutectic point of the Sm-Cu alloy [4]. Ternary or quaternary Sm eutectic alloys are expected to have lower melting points than binary eutectic alloys. Therefore, to achieve melting point below 500 ˚C, ternary or quaternary Sm-based eutectic alloys have been set to the candidate for the binder alloy. Fe, Cu and Al were selected as the candidate of additive element. The binary phase diagram of Sm-Fe, Sm-Cu and Sm-Al are shown in Fig. 2.1-3 [5]. The Sm-Fe eutectic point was 720 ˚C, which is not so low, but this composition was expected to improve wettability with the $Sm_2Fe_{17}N_3$ grain surface because Fe is the main component of $Sm_2Fe_{17}N_3$. The solution-reprecipitation effect was also expected to Sm-Fe alloy because of same reason. The Sm-Cu eutectic point is the lowest among the binary Sm-based alloys. Cu as well as Al was have been reported to have a significant effect in improving magnetic properties of $Nd_2Fe_{14}B$ sintered magnets [6]. In addition, all the candidate elements are abundant and readily available, which is important in respect of practical application.

In this chapter, at first, some compositions of alloys were prepared from above element. The composition of eutectic alloy was optimized on the basis of the result of thermal analysis and

microstructure analysis of the prepared alloys. As a result, target low-melting point Sm-based alloy, which has melting point below 500 ˚C, was developed. The reason of low-melting point was discussed from microstructure analysis. From measurement of demagnetization curve, the developed alloy was estimated whether it is suitable for binder alloy. This chapter is partly reproduced from "Consolidation of $Sm_2Fe_{17}N_3$ magnets with Sm-based eutectic alloy binder" by Otogawa, K; Takagi, K; Asahi, T. *Journal oh Alloys and Compounds* **2018**, 746C, 19-26, Elsevier, copyright 2018.

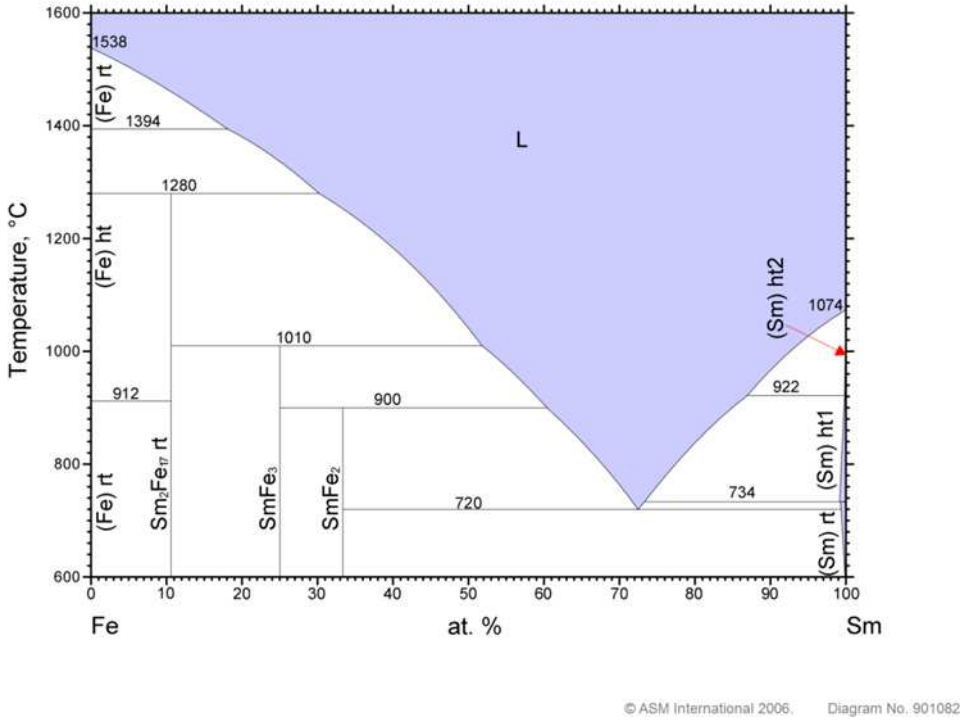

Figure 2.1 Binary phase diagram of Sm-Fe [5].

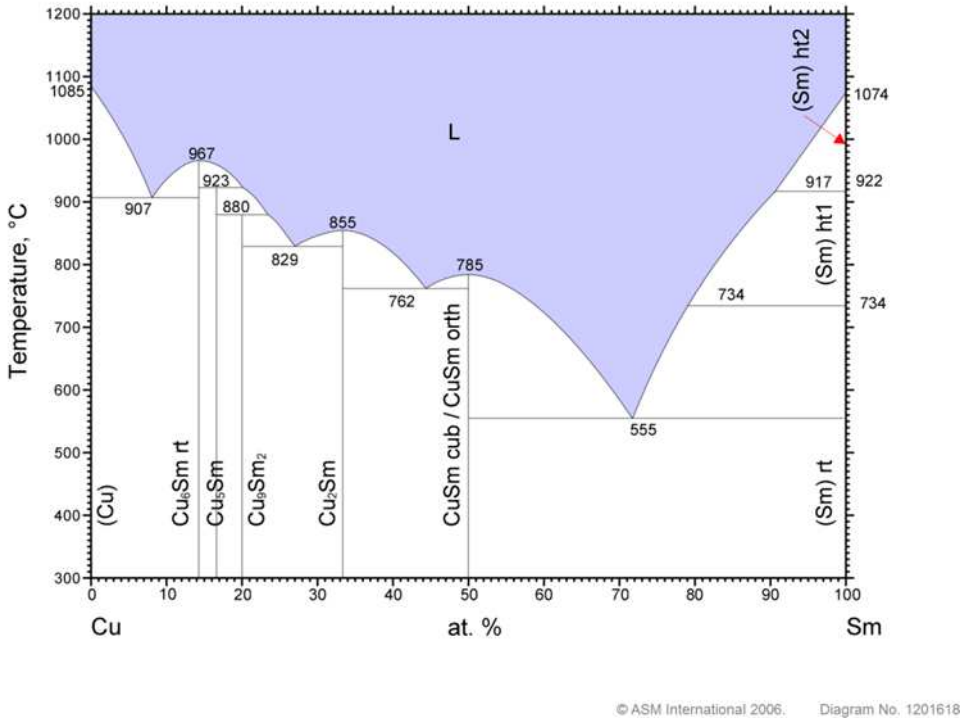

Figure 2.2 Binary phase diagram of Sm-Cu [5].

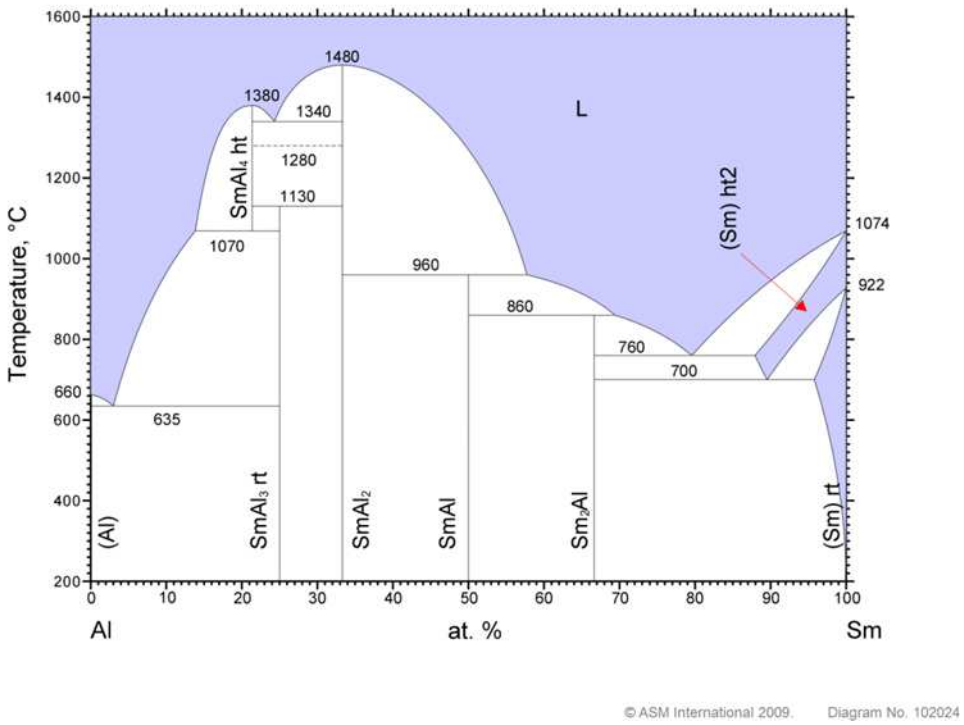

Figure 2.3 Binary phase diagram of Sm-Al [5].

2.2 Materials and methods

2.2.1 Materials

Sm ingot (>99.9%), Fe foil (>99.99%), Cu grain (>99.0%) and Al plate (>99.99%) were used as raw materials of alloys.

2.2.2 Alloying method

The raw materials were alloyed by arc melting apparatus (ACM-DS-01, Diavac, Japan) as shown in Fig 2.4. To avoid oxidation of alloys, arc melting chamber was evacuated to 2×10^{-2} Pa by diffusion pump and purged at least three times with purity argon gas. Titanium button was melted as oxygen getters prior to ingot melting. Because melting point of Fe is higher than that of other materials, other materials were wrapped with Fe foil and arc discharge was directly applied to Fe foil firstly. To make homogeneous alloy ingot, the ingots were inverted and melted at least 5 times. Example image of the prepared button ingots by arc melting method is shown in Fig 2.5. The optimized composition alloy was prepared again by a cold crucible melting method by Sinfonia Technology Co., Ltd. The cold crucible method melts the materials in water-cooled copper crucible by high frequency heating. Therefore, high-purity ingot is prepared by this method, even if the materials have high reactivity. The prepared button ingot by cold crucible melting method is shown in Fig. 2.6.

Figure 2.4 Arc melting apparatus.

Figure 2.5 Button ingots prepared by arc melting method.

Figure 2.6 Button ingot prepared by cold crucible method.

2.2.3 Thermal analysis

The thermodynamic properties of the prepared alloys were measured by differential scanning calorimetry (DSC: STA 449 F1 Jupiter, Netzsch, Germany) as shown in Fig. 2.7. The samples were put in an alumina (Al_2O_3) pan. To avoid oxidation as much as possible, measurement chamber was evacuated by rotary pump and purged with purity argon gas. Residual oxygen was reduced by using Zr oxygen getter. The analyses were carried out at a heating rate of 20℃/min. The Pure argon gas was flowed during measurement and its flow rate was 150 ml/min.

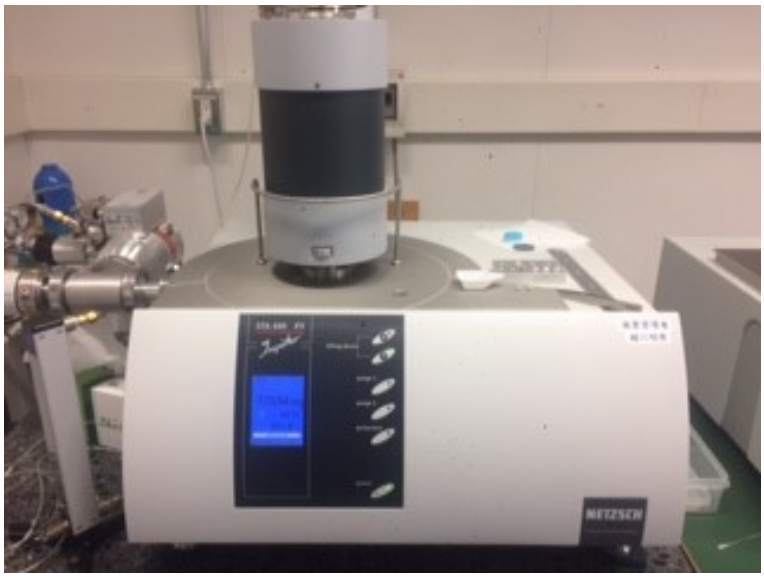

Figure 2.7 DSC apparatus.

2.2.4 Microstructural observation

Semi-quantitative elemental analyses and cross-sectional observation of the prepared alloys were conducted with a field emission scanning electron microscopy (FE-SEM; JSM-7800F, JEOL, Japan) equipped with an energy dispersive X-ray analyzer (EDX: XFlash 6130, Bruker, USA) as shown in Fig. 2.8. The prepared button ingots were cut and mirror-polished

using diamond paste. Accelerating voltage of electron beam was 10 kV.

Figure 2.8 EDX equipped FE-SEM.

2.2.5 X-ray diffraction measurement

Phase identifications of the prepared alloys were performed by X-ray diffractometry using Co Kα radiation (XRD; Empyrean, Panalytical, Netherlands) as shown in Fig. 2.9. Surface of the prepared button ingots were grinded with polishing paper. Measuring method was θ-2θ method. 45kV and 40mA of electric current was applied to Co target. Width of radiation beam was 10mm and it was radiated 500s per 0.013°.

Figure 2.9 XRD apparatus.

2.3 Results and Discussions

2.3.1 Ternary Sm-based alloys

The eutectic composition ratio (at%) of binary Sm-Cu and Sm-Fe are approximately Sm: Cu or Fe = 78 : 22. As the first attempt, $Sm_{60}Fe_{20}Cu_{20}$ alloy was prepared because composition ratios of Fe and Cu against Sm are nearly to that of binary eutectic compositions. DTA curve of the $Sm_{60}Fe_{20}Cu_{20}$ alloy was shown in Fig. 2.10. Melting point of the $Sm_{60}Fe_{20}Cu_{20}$ alloy was 552.3 ˚C which is slightly lower than that of Sm-Cu eutectic alloy. The cross-sectional SEM image of the $Sm_{60}Fe_{20}Cu_{20}$ alloy was shown in Fig. 2.11. Three kinds of structure were observed in this alloy. Semi-quantitative elemental analyses were performed to these three structures with EDX apparatus. The elemental composition (at%) of the black structure indicated as (a) was Sm : Fe : Cu = 35 : 60 : 5. This structure was supposed to $SmFe_2$ phase which contains little amount of solid solution of Cu. The elemental composition (at%) of the white structure indicated as (b) was Sm : Fe : Cu = 85 : 5 : 10. This structure was supposed to Sm phase which contains solid solution of Fe and Cu. The elemental composition (at%) of the gray structure indicated as (c) which fills gap of structure (a) and (b) was Sm : Fe : Cu = 70 : 5 : 25. This structure was supposed to Sm-Cu eutectic phase which contains little amount of solid solution of Fe. This metal structure is reasonable considering with the binary phase diagrams of Sm-Fe and Sm-Cu (Fig. 2.1 and 2). When melted sample are cooled, $SmFe_2$ and Sm phases are firstly precipitated around 720 ˚C, which is the eutectic point of Sm-Fe. However, at this point, Sm phase does not solidify because Sm and Cu forms liquid phase. Therefore, only $SmFe_2$ phase is precipitated as primary phase. After that, around 555 ˚C, which is the eutectic point of Sm-Cu, a little excessive Sm phase is precipitated previously and the rest of elements are precipitated as Sm-Cu eutectic phase. Therefore, the measured melting point of 552.3 ˚C might be melting point of the Sm-Cu eutectic phase which contains little amount of solid solution of Fe. The reduction of the melting point might be due to dissolution of solid solution Fe into the

Sm-Cu eutectic structure.

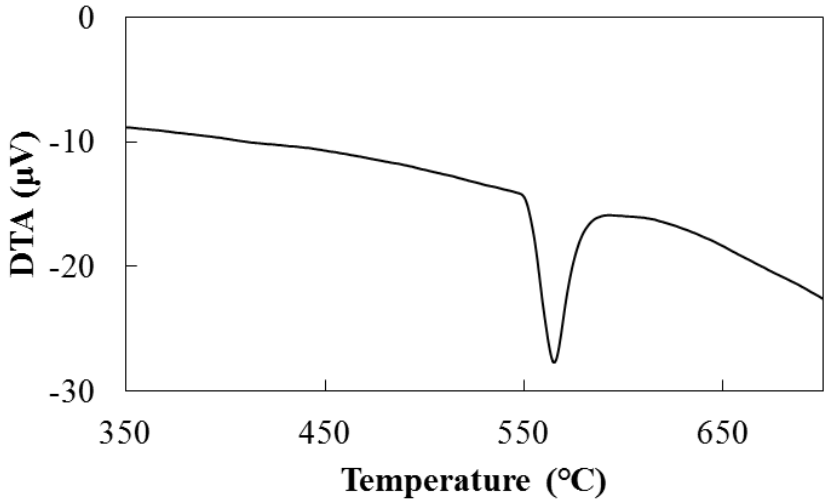

Figure 2.10 DTA curve of $Sm_{60}Fe_{20}Cu_{20}$ alloy.

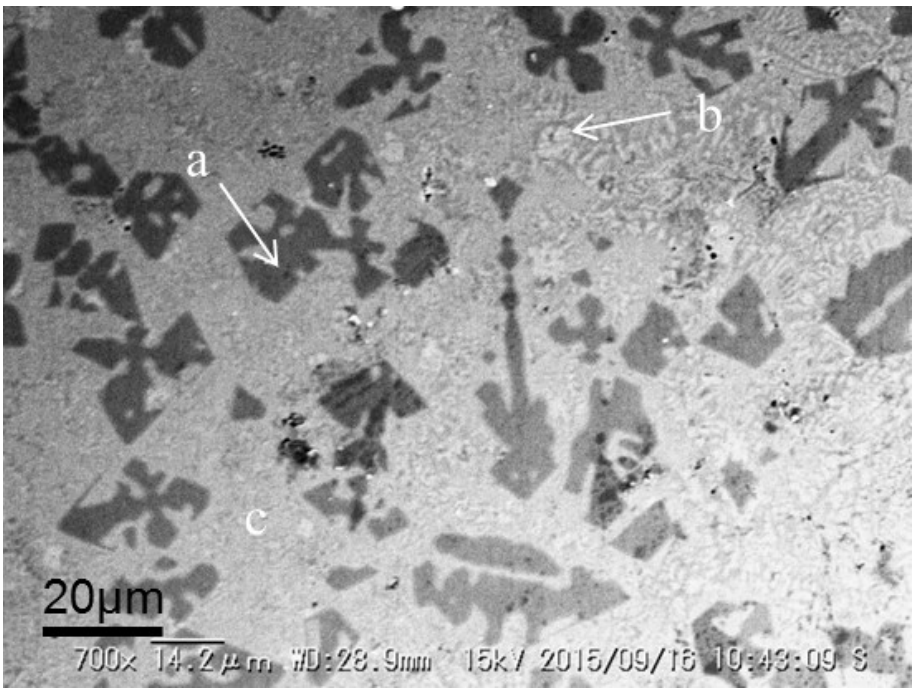

Figure 2.11 Cross sectional SEM-BSE image of $Sm_{60}Fe_{20}Cu_{20}$**.**

The microstructural observation of $Sm_{60}Fe_{20}Cu_{20}$ alloy suggested that dissolution of solid solution Fe into the Sm-Cu eutectic structure decrease melting point of the alloy. Hence,

variety compositions of Sm-Fe-Cu alloys, whose Sm-Cu compositions were near Sm-Cu eutectic composition, were prepared. Those compositions and melting points were shown in Fig. 2.12. A vertical axis of this figure shows melting points of alloys. A horizontal axis of this figure shows composition ratio of Sm / (Sm+Cu). A depth of green plot shows ratio of Fe atom. The $Sm_{82}Fe_8Cu_8$ alloy showed lowest melting point of 533 ˚C among the prepared Sm-Fe-Cu alloys. The DSC curve of the $Sm_{82}Fe_8Cu_8$ alloy was shown in Fig. 2.13.

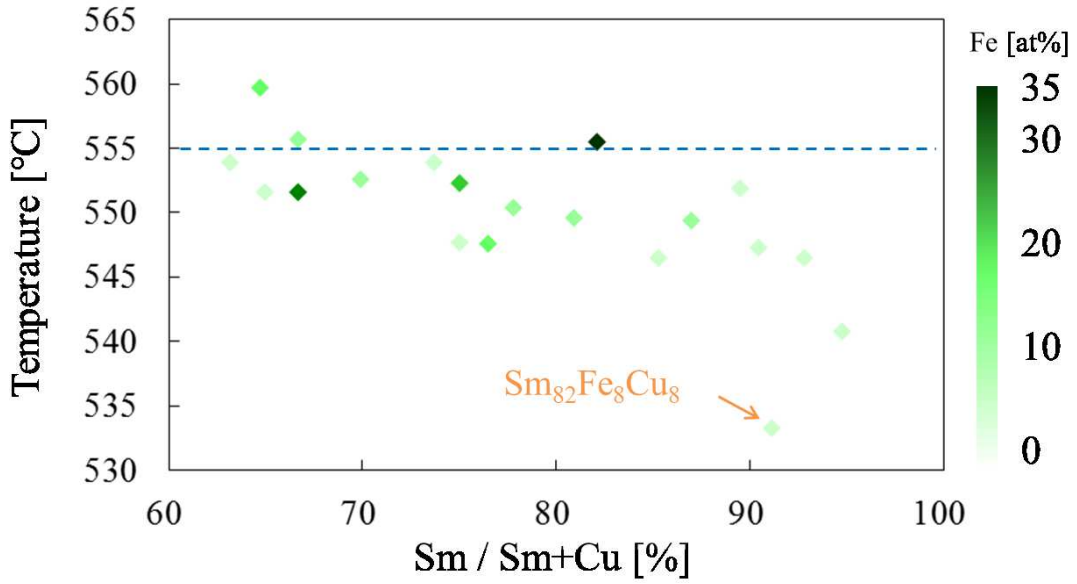

Figure 2.12 Eutectic point of Sm-Fe-Cu alloys.

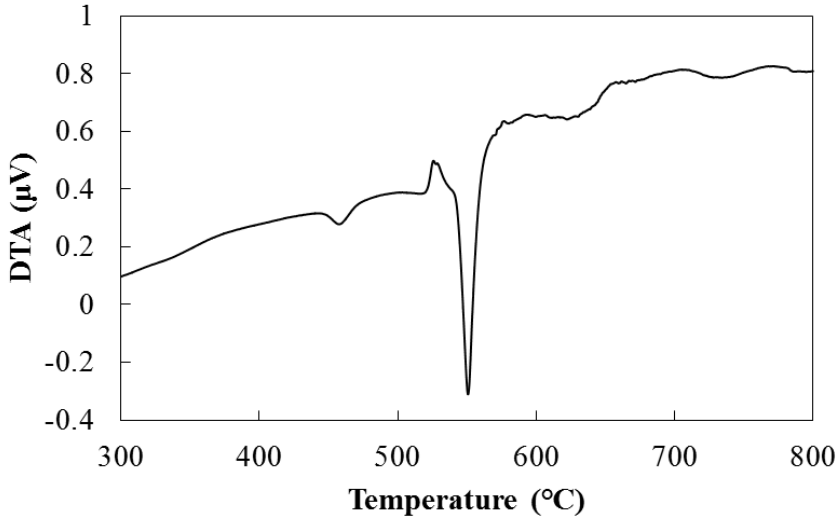

Figure 2.13 DSC curve of $Sm_{82}Fe_8Cu_8$ alloy.

The cross-sectional SEM image of the $Sm_{82}Fe_8Cu_8$ alloy was shown in Fig. 2.14. Three kinds of structure were observed in this alloy. It looks like a hypo-eutectic structure. The elemental composition (at%) of the large white structure indicated as (a) was Sm : Fe : Cu = 99 : 0 : 1. This structure was supposed to Sm single phase. The elemental composition (at%) of the gray structure indicated as (b) was Sm : Fe : Cu = 48 : 11 : 41. This structure was supposed to SmCu phase which contains solid solution of Fe. The elemental composition (at%) of the lamellar structure indicated as (c) was Sm : Fe : Cu = 71 : 5 : 24. This structure was supposed to Sm-Cu eutectic phase which contains little amount of solid solution of Fe. Simply considering, the melting point of 533 ˚C was supposed to indicate the melting point of the lamellar structure (structure (c)) but structure (a) and (b) might not be melted. As shown in Fig. 2.2, the melting point of pure SmCu phase is 785 ˚C. The melting point of the structure (b) might be lower than that of pure SmCu phase because structure (b) dissolves solid solution of Fe in SmCu phase. However, there was no obvious endothermic peak around 785 ˚C. From these results, it was presumed that this $Sm_{82}Fe_8Cu_8$ alloy was composed of the combination of fine eutectic structure which was formed at the stage of initial rapid solidification and coarse eutectic structure which was formed at the stage of latter slow solidification.

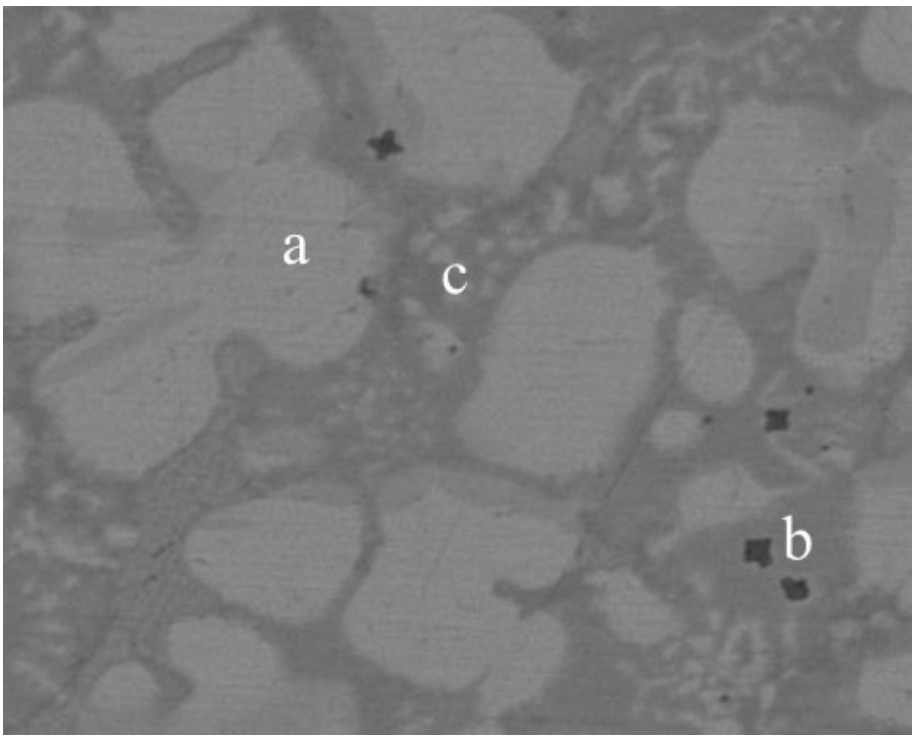

Figure 2.14 Cross sectional SEM-BSE image of $Sm_{82}Fe_8Cu_8$ alloy.

In addition, the DSC curve of $Sm_{82}Fe_8Cu_8$ alloy (Fig. 2.13) showed small endothermic peak near 450 ˚C. This peak was supposed to enthalpy relaxation peak of the lamellar structure (structure (c)) because this structure was supposed to be amorphous like structure due to rapid solidification. The exothermic peak near 520 ˚C was accordingly supposed to be the crystallization peak of that. To confirm these inferences, further examination is demanded. However, the purpose of this study was developing low-melting point Sm-based alloy to be used as binder alloy. Therefore, further examination to confirm these inferences had not been performed.

Ternary Sm-Fe-Al and Sm-Cu-Al alloys were also prepared. Representative eutectic points of the prepared ternary Sm-based alloys were shown in Table 2.1. Either ternary Sm-based alloy showed decrease of melting point compared with binary Sm-based eutectic alloys.

Therefore, it was suggested that solid solution of Al also decrease the melting temperature of Sm-based alloy. However, the ternary eutectic points did not reach the target point of 500 ˚C.

Table 2.1 Eutectic point of ternary Sm based alloys.

	Eutectic point (˚C)
$Sm_{82}Fe_8Cu_8$	533
$Sm_{70}Fe_{14}Al_{16}$	627
$Sm_{73}Cu_{16}Al_{11}$	546

2.3.2 Quaternary Sm-based alloys

The ternary alloys suggested that solid solution of Fe and Al decrease the melting point of Sm-based alloy. To achieve below 500 ˚C eutectic points, therefore, quaternary Sm-based alloys with Fe, Cu and Al were tried to prepare. The DSC curve of $Sm_{63}Fe_5Cu_{22}Al_{10}$ alloy, whose composition was optimized, showed an endothermic peak at 495 ˚C as shown in Fig. 2.15. This result, therefore, verifies that a eutectic point below 500 ˚C can be achieved with a Sm-based quaternary alloy. This thermodynamic property was a promising sign for a sintering binder alloy of $Sm_2Fe_{17}N_3$. Therefore, in this research, I focused on this $Sm_{63}Fe_5Cu_{22}Al_{10}$ alloy as the sintering binder. This $Sm_{63}Fe_5Cu_{22}Al_{10}$ alloy is simply called "Sm-Fe-Cu-Al alloy" in the following.

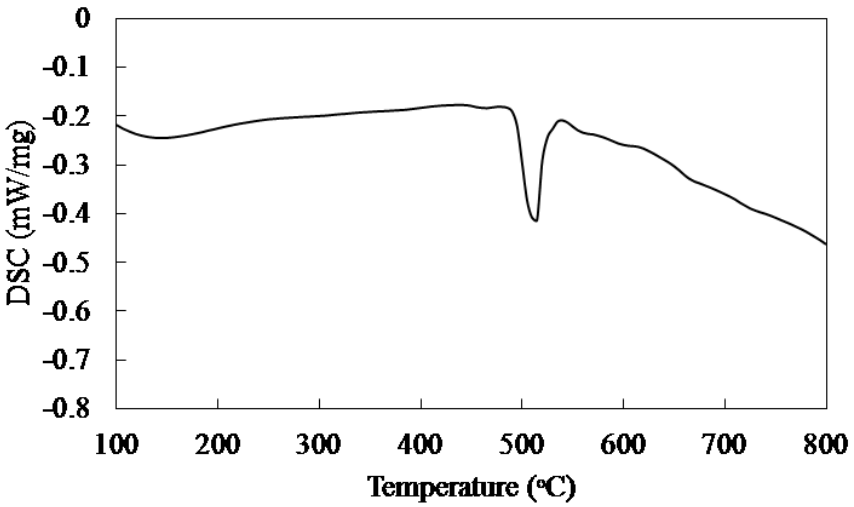

Fig. 2.15 DSC curve of $Sm_{63}Fe_5Cu_{22}Al_{10}$ alloy. This figure is reproduced from "Consolidation of $Sm_2Fe_{17}N_3$ magnets with Sm-based eutectic alloy binder" by Otogawa, K; Takagi, K; Asahi, T. *Journal oh Alloys and Compounds* **2018**, 746C, 19-26, Elsevier, copyright 2018.

A binder alloy is supposed to have a great influence on the magnetic properties of a sintered magnet. The previous analytical studies of $Nd_2Fe_{14}B$ sintered magnets have revealed the significant roles for the grain boundary in magnetic properties [7], therefore a binder alloy which forms a grain boundary should exert an influence on the resultant sintered magnets. To clarify this point, the magnetic properties and microstructure of the Sm-Fe-Cu-Al alloy were evaluated. As shown in Fig. 2.16, the XRD profile of the Sm-Fe-Cu-Al alloy ingot showed the diffraction peaks of the cubic SmCu (ICDD card No.04-004-5311), rhombohedral α-Sm (ICDD card No.04-007-1895), cubic Sm_2O (ICDD card No.01-072-5853) and cubic SmO (ICDD card No.00-033-1146) phase but no diffraction peaks derived from Fe and Al. The Sm_2O and SmO might be ineluctable oxides in air atmosphere analysis. Actually, as shown in Fig. 2.17, EDX line analysis of surface to cross-section of the Sm-Fe-Cu-Al bulk alloy which was processed by FIB showed that oxygen concentration of surface was higher than that of cross-section. Thus, the prepared Sm-Fe-Cu-Al alloy substantially consisted of the two phases of SmCu and α-Sm. Carefully looking at the diffraction peak of SmCu, the peak of the (211) plane at around 76° was remarkably shifted to a lower angle. This peak shift indicates lattice expansion. Considering the missing of diffraction peaks which were derived from Al or Fe, the SmCu phase was expected to form a solid solution with Al and Fe. The α-Sm phase also had a possibility of a solid solution with Al and Fe. However, the peak shift of Sm was hard to recognize due to overlap with other diffraction peaks.

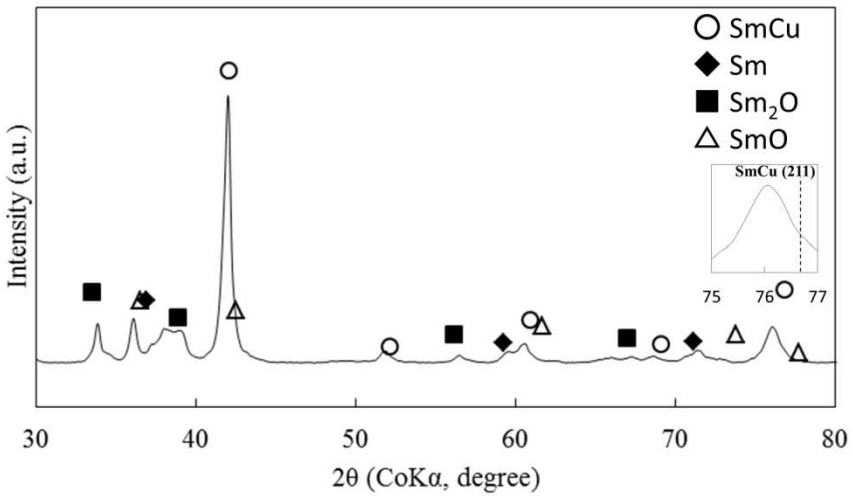

Fig. 2.16 XRD profile of the $Sm_{63}Fe_5Cu_{22}Al_{10}$ alloy ingot. The inset figure shows an enlarged view of the profile from 75° to 77°, and the broken line represents the diffraction angle of SmCu (211). This figure is reproduced from "Consolidation of $Sm_2Fe_{17}N_3$ magnets with Sm-based eutectic alloy binder" by Otogawa, K; Takagi, K; Asahi, T. *Journal oh Alloys and Compounds* **2018**, 746C, 19-26, Elsevier, copyright 2018.

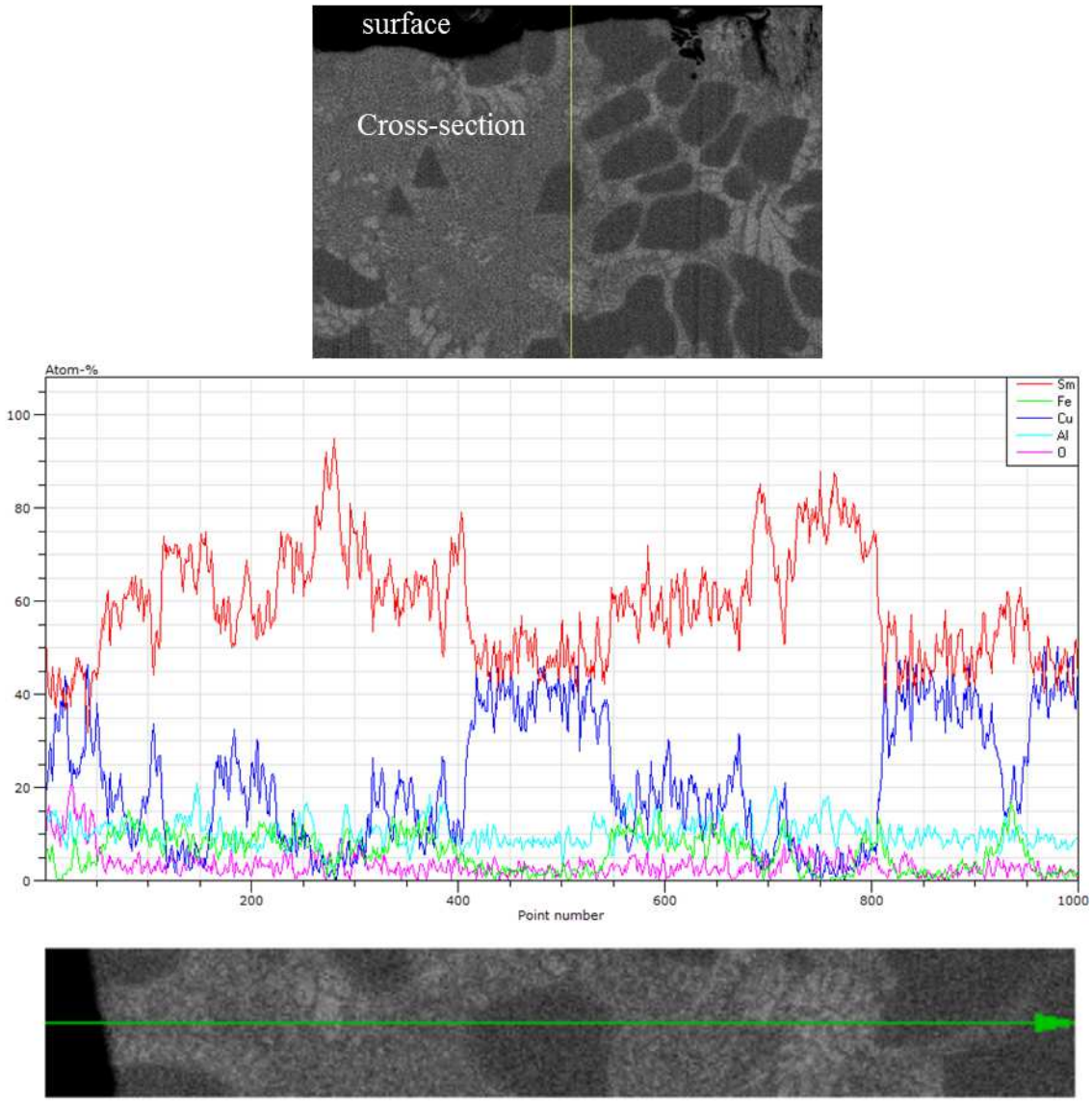

Figure 2.17 EDX line analysis of surface to cross-section of the Sm-Fe-Cu-Al bulk alloy. Analyzed line was shown as yellow line of the upper SEM image.

To assist in the discussion about the constituent phases of Sm-Fe-Cu-Al alloy, a SEM-EDX analysis was performed for a cross-section of the Sm-Fe-Cu-Al ingot. As shown in Fig. 2.18, SEM-BSE cross-sectional image of the Sm-Fe-Cu-Al alloy revealed that this alloy consisted of four different regions. Table 2.2 shows the compositions of these regions, which were determined by EDX semi-quantitative elemental analysis. The most occupied dark gray regions, which were shown as Fig. 2.18, Region 1, were a SmCu phase containing 1 at% Fe

and 8 at% Al, that is to say, $(SmCu)_{91}Fe_1Al_8$. These solid solutions of Fe and Al were consistent with the estimation from the peak shift of SmCu in the XRD results. The light gray regions, which were shown as Fig. 2.18, Region 2, were determined to be a Sm phase, but also contained a little amount of Fe, Cu and Al like the SmCu phase. The whitest regions, which were shown as Fig. 2.18, Region 3, were a Sm phase containing Fe and Al but no Cu. The lamellar regions, which were shown as Fig. 2.18, Region 4, seems to be lamellar structures formed from SmCu and Sm phases and contain 11at% Fe and 10 at% Al. Therefore, Fe and Al were enriched in the lamellar regions. Simply considering, the microstructure of Sm-Fe-Cu-Al alloy looks like a hypoeutectic structure which was composed of the primary phase of SmCu and the fine eutectic lamellar structure. The eutectic lamellar phase is supposed to have the melting point lower than 555 ˚C from a Sm-Cu phase diagram. Moreover, the melting point of the SmCu phase is expected to be lower than that of pure SmCu, 785 ˚C, because it contains Fe and Al atoms as solid-solution. However, the DSC curve of the Sm-Fe-Cu-Al ingot shows only single peak of 495 ˚C as shown in Fig. 2.15. From these facts, it was presumed that this Sm-Fe-Cu-Al alloy was composed of the combination of fine eutectic structure which was formed at the stage of initial rapid solidification and coarse eutectic structure which was formed at the stage of latter slow solidification. This structure was similar to $Sm_{82}Fe_8Cu_8$ alloy. From the above, the reduction in the melting point by quaternary alloying might be owing to a decrease in free energy by dissolution of solid-solution Fe, Cu and Al into the SmCu/Cu eutectic structure, even though there were differences in the concentrations.

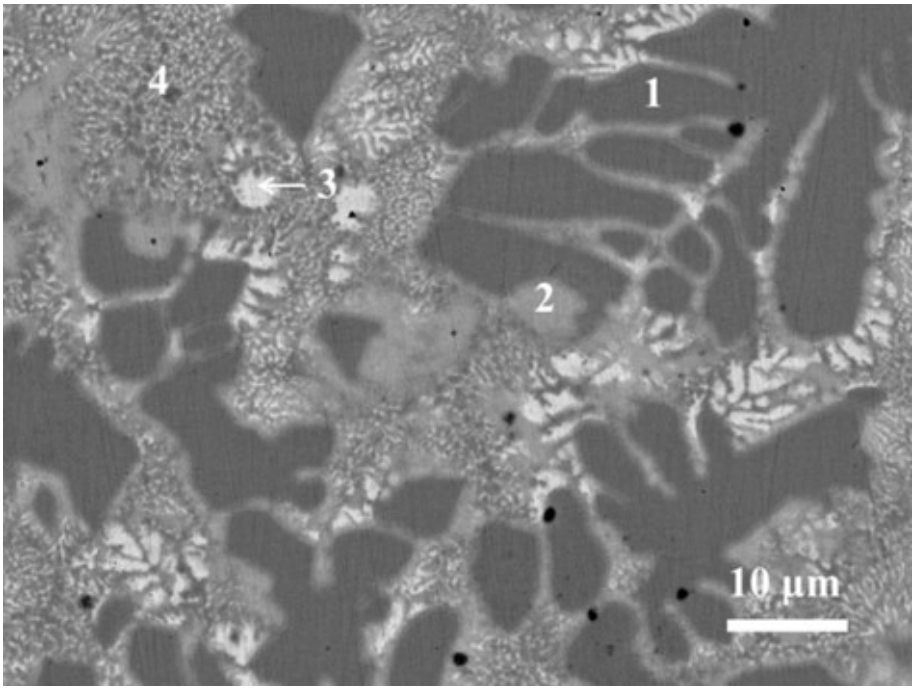

Fig. 2.18 SEM-BSE cross-sectional image of the $Sm_{63}Fe_5Cu_{22}Al_{10}$ ingot. This figure is reproduced from "Consolidation of $Sm_2Fe_{17}N_3$ magnets with Sm-based eutectic alloy binder" by Otogawa, K; Takagi, K; Asahi, T. *Journal oh Alloys and Compounds* **2018**, 746C, 19-26, Elsevier, copyright 2018.

Table 2.2 EDX analytical values of elemental compositions (at.%) for the different regions indicated in Fig. 2.18.

	Sm	Fe	Cu	Al
Region 1	48.6	1.2	41.7	8.5
Region 2	90.3	1.8	5.6	2.4
Region 3	89.9	6.2	0.0	4.0
Region 4	62.0	11.4	16.5	10.1

The magnetic property of the grain boundary layer greatly affects the coercivity of a

sintered magnet. The previous studies [7] have proposed that a nonmagnetic-like grain boundary layer is better to improve the coercivity of sintered magnets because it intercepts exchange coupling between the main phase grains. Hence, the magnetic property of the developed Sm-Fe-Cu-Al alloy was measured. The demagnetization curve of the Sm-Fe-Cu-Al alloy ingot was shown in Fig. 2.19. This alloy had slight remanent magnetization of 0.4 emu/g. This weak ferromagnetic characteristic might be derived from the magnetic moment of the Fe atoms. However, entire magnetization was proportional to the magnetic field: this alloy acted as a paramagnetic-like property, which might be derived from the paramagnetic SmCu and α-Sm phases. Therefore, this weak ferromagnetic and paramagnetic-like property of the Sm-Fe-Cu-Al alloy was expected to intercept or weaken the exchange coupling between the main phase grains in $Sm_2Fe_{17}N_3$ sintered magnets.

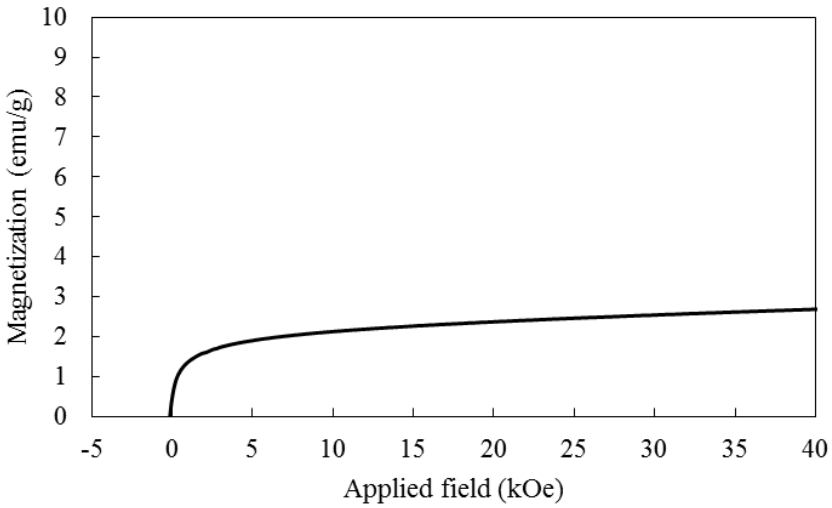

Figure 2.19 Demagnetization curve of the $Sm_{63}Fe_5Cu_{22}Al_{10}$ alloy ingot.

2.4 Conclusions

This study revealed that some ternary or quaternary Sm-based eutectic alloys had lower eutectic points than 620 ˚C, which is thermal decomposition temperature of $Sm_2Fe_{17}N_3$. Among them, especially quaternary $Sm_{63}Fe_5Cu_{22}Al_{10}$ alloy was found to have very low melting temperature of 495 ˚C. This thermodynamic property was a promising sign for a sintering binder alloy of $Sm_2Fe_{17}N_3$. This Sm-Fe-Cu-Al alloy was composed from Sm phase and SmCu phase and each phase has solid solutions of Fe, Cu and Al. Therefore, the reduction in the melting point by quaternary alloying might be owing to a decrease in free energy by dissolution of solid-solution Fe, Cu and Al into the SmCu/Cu eutectic structure. In addition, the Sm-Fe-Cu-Al alloy had nonmagnetic-like and paramagnetic-like property. Therefore, the Sm-Fe-Cu-Al binder alloy was expected to intercept or weaken the exchange coupling between the main phase grains in $Sm_2Fe_{17}N_3$ sintered magnets.

2.5 References

[1] D.T. Zhang, M. Yue, J.X. Zhang, Study on bulk Sm2 Fe17 Nx sintered magnets prepared by spark plasma sintering, Powder Metallurgy. 50 (2007) 215–218. doi:10.1179/174329007X169128.

[2] J.M.D. Coey, J.F. Lawler, H. Sun, J.E.M. Allan, Nitrogenation of R2Fe17 compounds: R=rare earth, Journal of Applied Physics. 69 (1991) 3007–3010. doi:10.1063/1.348614.

[3] K. Schnitzke, L. Schultz, J. Wecker, M. Katter, High coercivity in Sm2Fe17Nx magnets, Applied Physics Letters. 57 (1990) 2853–2855. doi:10.1063/1.104202.

[4] H. Okamoto, Cu-Sm(Copper-Samarium), Journal of Phase Equilibria and Diffusion. 19 (1998) 183.

[5] H. Baker, H. Okamoto, ASM Alloy Phase Diagrams Database, ASM International. (2017). http://www.asminternational.org.

[6] J. Fidler, T. Schrefl, Overview of Nd-Fe-B magnets and coercivity, Journal of Applied Physics. 79 (1996) 5029–5034. doi:10.1063/1.361565.

[7] K. Hono, H. Sepehri-Amin, Strategy for high-coercivity Nd-Fe-B magnets, Scripta Materialia. 67 (2012) 530–535. doi:10.1016/j.scriptamat.2012.06.038.

Chapter 3

Magnetic Properties of Sm-based Alloy Binder Added $Sm_2Fe_{17}N_3$ Sintered Magnets

3.1 Introduction

In chapter 2, the quaternary Sm-Fe-Cu-Al eutectic alloy was found to have a melting point of 495°C, which was more than 100°C lower than the decomposition temperature of $Sm_2Fe_{17}N_3$. The nonmagnetic-like characteristic of the Sm-Fe-Cu-Al alloy was preferred as binder alloy because it could contribute to enhance the coercivity of the sintered magnets. The $Nd_2Fe_{14}B$ sintered magnet is known to be consolidated by liquid phase sintering phenomenon [1]. Nd-rich phase is melted during sintering process. The Nd-rich phase liquid not only removes surface oxide layer but also improves the coercivity and density of sintered compact [2–4]. The Sm-Fe-Cu-Al alloy was expected to have same effects against the $Sm_2Fe_{17}N_3$ magnet. Therefore, the magnetic properties of Sm-Fe-Cu-Al bonded $Sm_2Fe_{17}N_3$ magnets were expected to be higher than that of additive-free $Sm_2Fe_{17}N_3$ magnets. It is noted that, generally, consolidated compact of the $Sm_2Fe_{17}N_3$ using metal binder was described as "hot-pressed magnet" but not "sintered magnet" because previously reported metal binders did not cause diffusion of $Sm_2Fe_{17}N_3$ phase. However, this study expects the Sm-Fe-Cu-Al binder "to remove surface oxides" as well as "to dissolve the main phase". In other words, the Sm-Fe-Cu-Al binder is expected to play a role of sintering aid capable of facilitating densification by diffusion of $Sm_2Fe_{17}N_3$ phase, whereas the previously reported metal binders played nothing other than the role of binder and did not facilitate densification of $Sm_2Fe_{17}N_3$ phase. Therefore, this study mentioned the consolidated compacts of the Sm-Fe-Cu-Al added $Sm_2Fe_{17}N_3$ as "sintered compacts".

In this chapter, at first, the Sm-Fe-Cu-Al alloy ingot was pulverized with wet ball milling

method which is a general powder metallurgy technique. The pulverized Sm-Fe-Cu-Al powder as a sintering binder was mixed with raw $Sm_2Fe_{17}N_3$ powder. The Sm-Fe-Cu-Al added $Sm_2Fe_{17}N_3$ powder was sintered. The magnetic properties of the binder-added $Sm_2Fe_{17}N_3$ sintered compact was compared with additive-free $Sm_2Fe_{17}N_3$ sintered compact. In addition, the Sm-Fe-Cu-Al added $Sm_2Fe_{17}N_3$ powders were sintered at various sintering temperature. The dependence of coercivity on the sintering temperature of binder-added sintered compacts and additive-free sintered compacts were discussed in aspect of precipitated amount of α-Fe. Finally, the absolute densities of the binder-added sintered compacts and additive-free sintered compacts were measured and the promotion effect of the Sm-Fe-Cu-Al sintering binder was discussed. This chapter is partly reproduced from "Consolidation of $Sm_2Fe_{17}N_3$ magnets with Sm-based eutectic alloy binder" by Otogawa, K; Takagi, K; Asahi, T. *Journal oh Alloys and Compounds* **2018**, 746C, 19-26, Elsevier, copyright 2018.

3.2 Materials and methods

3.2.1 Materials

The $Sm_{63}Fe_5Cu_{22}Al_{10}$ alloy was used as sintering binder. As mentioned at section 2.2.2, the button ingot of the mother alloy with a diameter of 60mm was prepared by a cold crucible melting method from Sm ingot (>99.9%), Fe foil (>99.99%), Cu grain (>99.0%) and Al plate (>99.99%). In the cold crucible method, the materials are melted in a water-cooled copper crucible by high frequency heating. Therefore, high-purity ingots can be prepared by this method, even when using high reactivity materials. A commercial $Sm_2Fe_{17}N_3$ powder (Sumitomo Metal Mining Co., Ltd.) was used as raw $Sm_2Fe_{17}N_3$ powder. The grain size distribution of the $Sm_2Fe_{17}N_3$ powder is shown in Fig. 3.1. The mean diameter of the raw $Sm_2Fe_{17}N_3$ powder was about 3μm. Note that surface of the commercial $Sm_2Fe_{17}N_3$ powder was already oxidized because it was exposed to the air.

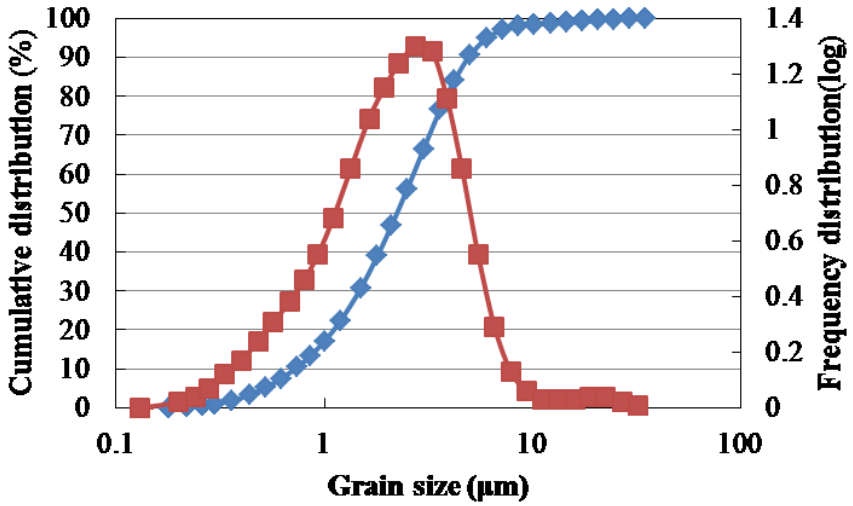

Figure 3.1 Grain size distribution of commercial $Sm_2Fe_{17}N_3$ powder. Blue plot indicates cumulative distribution and red plot indicates frequency distribution.

3.2.2 Pulverizing method

The Sm-Fe-Cu-Al button ingot was pulverized into fine powder to be mixed with raw

$Sm_2Fe_{17}N_3$ powder. This binder alloy is readily oxidized due to its Sm-rich composition. Therefore, pulverization of the binder alloy was performed in a low-oxygen atmosphere glove box. Prior to the pulverization process, the atmosphere inside the glove box was replaced with highly pure Ar gas, after that the residual oxygen was sufficiently removed down to an oxygen concentration of below 1ppm by an inert gas refiner. In the pulverization process, the binder alloy ingot was first ground by a hand grinder to a submillimeter-sized coarse powder. This coarse binder powder was further pulverized into a fine powder by planetary ball milling (Pulverisette 7, Fritsch, Germany) as shown in Fig. 3.2. The coarse powder was put into an 80mL stainless vessel with 5 mm diameter stainless balls and filled with adequate amount of acetonitrile (CH_3CN). The weight ratio of the balls and the coarse powder was 100 : 5. The milling rotation speed was 200rpm and the total milling time was 10 hours. The fine alloy powder was prepared by evaporating the slurry.

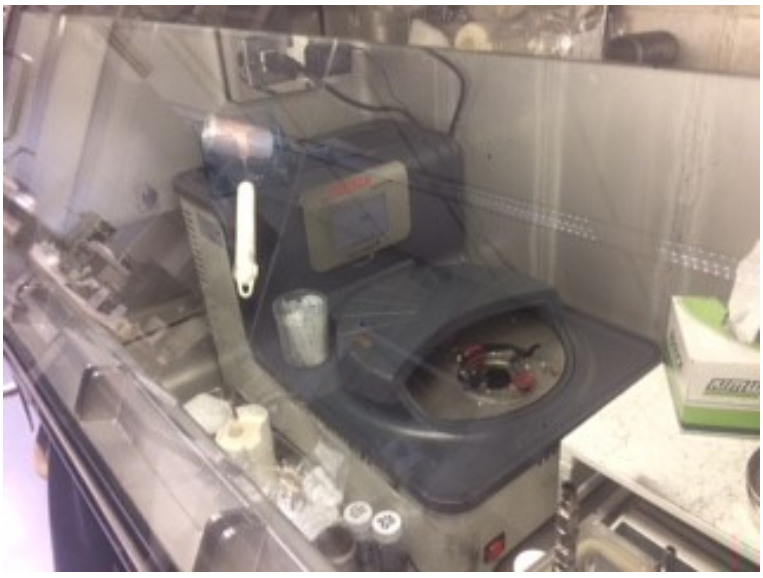

Figure 3.2 Planetary ball milling apparatus in glove box.

3.2.3 Mixing method

The fine binder alloy powder and commercial $Sm_2Fe_{17}N_3$ powder were mixed by wet or dry

ball milling. To prevent oxidation of powders, the mixing process was also performed with the same apparatus as in the pulverization step. The mixing ratio of the binder and raw $Sm_2Fe_{17}N_3$ powder was 20: 80 in weight, and the ratio of the mixed powder and balls was 200 : 5 in weight. The wet ball milling method added adequate amount of acetonitrile. The mixings were performed at a milling speed of 200 rpm for a total milling time of 2 hours. During this process, the mixings were paused for 15 minutes after every 15 minutes of milling to avoid excessive heating of the powders. Meanwhile, additive-free $Sm_2Fe_{17}N_3$ powder was also milled under the same conditions for comparison.

3.2.4 Sintering method

The milled powders were sintered by electric current sintering apparatus (Plasman, SS Alloy Co. Ltd., Japan) (Fig. 3.3), which is a kind of hot-pressing method. The 0.5 g of the milled powders were filled in a 6 mm diameter cylindrical die set made of cemented carbide (WC-FeAl) (Fig. 3.4). To prevent oxidation of the powders, the whole mold containing the powder was immersed in a liquid medium of acetonitrile for shielding against air exposure as shown in Fig. 3.5, and was transferred from the glove box to the sintering system. The sintering chamber was evacuated and the powder was pressed under the uniaxial pressure of 1.2 GPa. After the vacuum dropped below 2Pa by volatilization of the liquid medium of acetonitrile, heating of the powder was started. The sintering temperature was varied from 300 ˚C to 650 ˚C, and the holding time and the heating rate were set to be 5 minutes and 40 ˚C minutes, respectively. Incidentally, Soda *et al*. [5] reported that the sintering procedure described above was assured to prevent in-process oxidation of powders.

Figure 3.3 Electric current sintering apparatus.

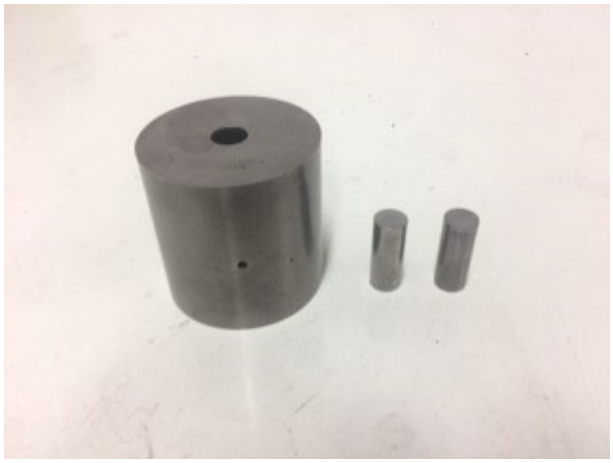

Figure 3.4 Cylindrical die set.

Figure 3.5 Immersed die set in a liquid medium.

3.2.5 Magnetic property measurement

The demagnetization curves of the prepared powder and the sintered compacts were measured by a physical property measurement system equipped with a vibrating sample magnetometer (PPMS-VSM; Dynacool, Quantum Design, USA) (shown in Fig. 3.6) under a He atmosphere at 300 K. An external magnetic field was applied up to 90 kOe. The saturation magnetizations of prepared samples were calculated by the law of approach to saturation magnetization, which is shown below equation, using magnetization values of measured demagnetization curve.

$M = Ms^* (1-a/H^2-b/H^3-c/H^4-d/H^5)$

The coercivities of the prepared samples were measured with a pulse B-H tracer (PBH-1000, Nihon Denjisokki Co., Japan) as shown in Fig. 3.7. An external magnetic field was applied up to 55 kOe.

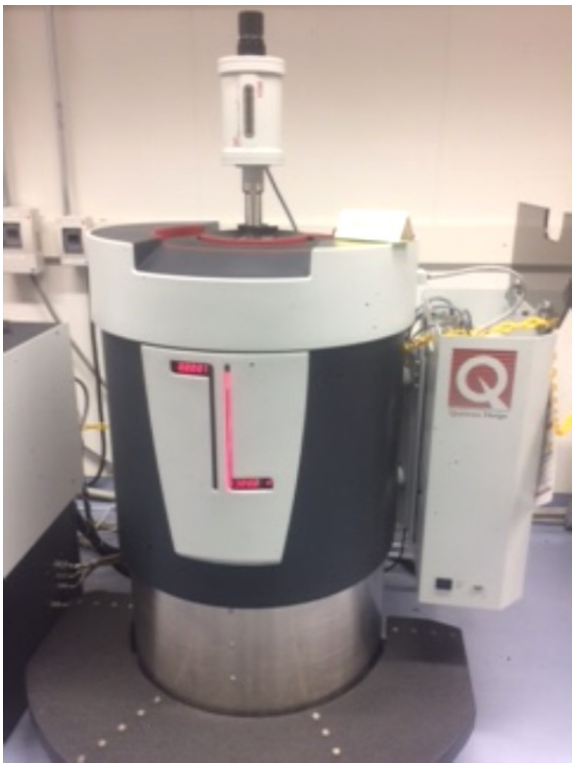

Figure 3.6 PPMS-VSM apparatus.

Figure 3.7 pulse BH-tracer apparatus.

3.2.6 X-ray diffraction measurement

Phase identifications of the prepared powders and sintered compacts were performed by X-ray diffractometry using Co Kα radiation (XRD; Empyrean, Panalytical, Netherlands) as shown in Fig. 2.9. Surface of the powders and cross-section of the sintered compacts were measured. Measuring method was θ-2θ method. 45kV and 40mA of electric current was applied to Co target. Width of radiation beam was 10mm and it was radiated 500s per 0.013°.

3.2.7 Density measurement

The absolute densities of the sintered compacts were measured by the Archimedes method. To avoid persistence of bubble at the surface voids, the surface voids of sintered magnets were filled with paraffin.

3.2.8 Microstructural observation

The prepared powders and sintered compacts were observed with EDX equipped FE-SEM apparatus as shown in Fig. 2.8. To observe cross-section, the prepared sample were embedded in epoxy resin and polished with diamond paste.

3.3 Results and discussions

3.3.1 Pulverizing of Sm-Fe-Cu-Al alloy

To obtain homogeneously mixed Sm-Fe-Cu-Al alloy added $Sm_2Fe_{17}N_3$ powder, the Sm-Fe-Cu-Al alloy was needed to be pulverized into fine powder whose grain size was as same as that of raw $Sm_2Fe_{17}N_3$ powder (mean diameter: 3 μm). The Sm-Fe-Cu-Al ingot was pulverized by wet ball milling method for 10 hours. As shown in Fig. 3.8, plate shaped fine Sm-Fe-Cu-Al powders with a mean diameter of 4 μm was prepared.

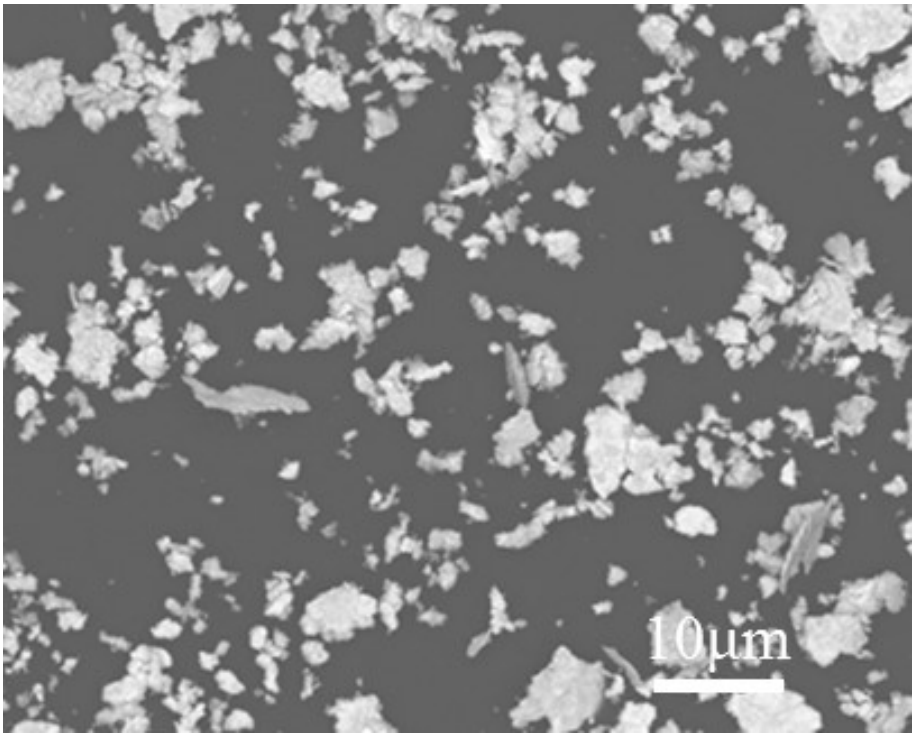

Figure 3.8 SEM image of Sm-Fe-Cu-Al pulverized powder.

3.3.2 Mixing method

Mixing method is important to produce sintered compact which has binder alloy layer at whole grain boundary. The additive ratio of the binder powder was 20 wt%. This additive ratio is relatively excessive compared to that of general practice, but assured that the binder would permeates into the whole grain boundary. At first, the cross-sectional images of the

additive-free $Sm_2Fe_{17}N_3$ compact sintered at 550 ˚C were shown in Fig. 3.9. Some white phase grains were observed. This white phase grains were Sm-rich grains which were natively contaminated in raw powder as impurities.

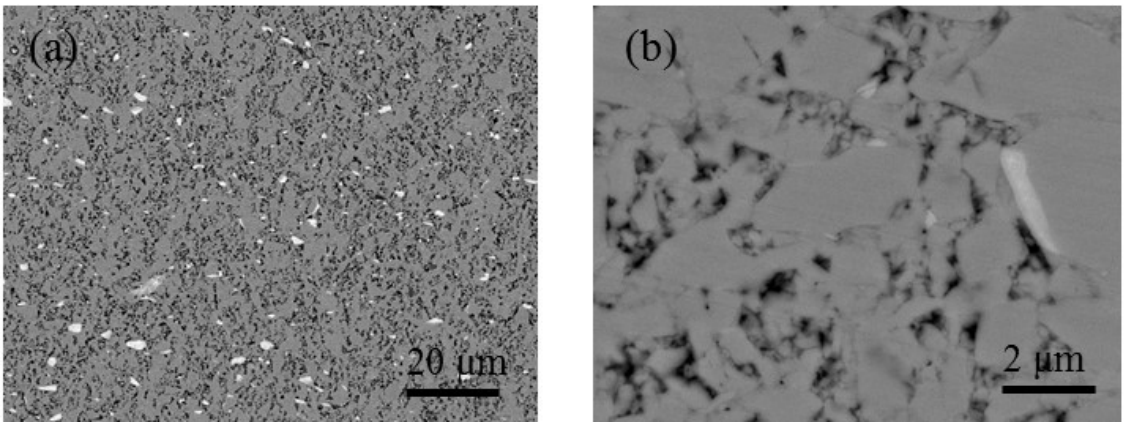

Figure 3.9 Cross-sectional SEM-BSE images of additive-free $Sm_2Fe_{17}N_3$ compact sintered at 550℃.

The cross-sectional images of the 550 ˚C sintered binder-added $Sm_2Fe_{17}N_3$ compact mixed by wet ball milling were shown in Fig. 3.10. There were not only Sm-rich grains but also bright white flat regions. These flat regions were Sm-Fe-Cu-Al alloy phases. As shown in Fig. 3.10 (a), the Sm-Fe-Cu-Al alloy phases were unevenly distributed. Furthermore, enlarged image of Fig. 3.10 (b) showed that the binder alloy was not permeated into grain boundary. Therefore mixing with wet ball milling method was revealed not to successfully disperse the binder alloy into grain boundary. The reason was presumed as below. The liquid medium might weaken adsorption power between particles, accordingly the binder particles and $Sm_2Fe_{17}N_3$ particles were easily separated during collection due to difference of their specific gravities.

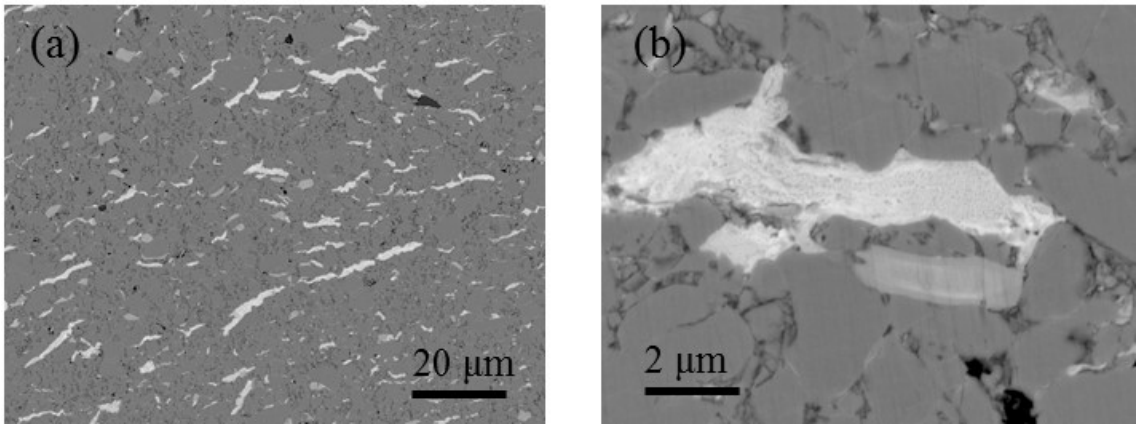

Figure 3.10 Cross-sectional SEM-BSE images of 550 ˚C sintered binder-added $Sm_2Fe_{17}N_3$ compact mixed by wet ball milling.

The mixing with wet ball milling method failed to produce sintered compact which has binder alloy layer at whole grain boundary. Hence, the milled binder alloy powder and raw $Sm_2Fe_{17}N_3$ powder were mixed with dry ball milling method which was expected to produce homogeneously mixed powder. Because dry ball milling method requires no liquid medium, separation of the binder particles and $Sm_2Fe_{17}N_3$ particles might be hard to occur compared with wet ball milling method. In addition, in certain instances, dry ball milling method can produce a core/shell structured powder. Fig. 3.11 showed cross-sectional SEM-BSE images of the 550 ˚C sintered binder-added $Sm_2Fe_{17}N_3$ compact mixed by dry ball milling. As shown in Fig 3.11 (a), the Sm-Fe-Cu-Al binder phase was evenly dispersed. Furthermore, enlarged image of Fig. 3.11 (b) showed that the binder alloy was permeated into grain boundary. Therefore, mixing with dry ball milling method was revealed to successfully disperse the binder alloy into grain boundary. This study calls this dry ball milling mixed powder as “binder-added powder” hereafter.

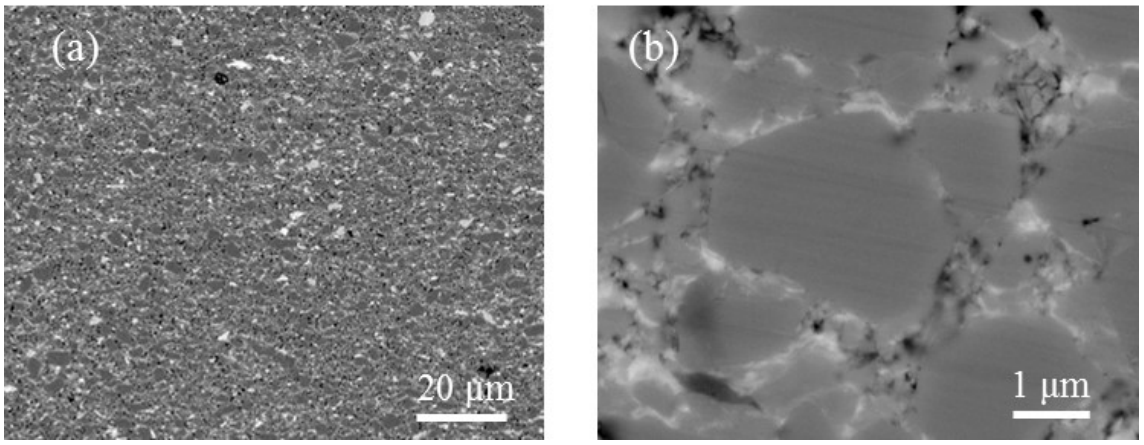

Figure 3.11 Cross-sectional SEM-BSE images of 550 ˚C sintered binder-added $Sm_2Fe_{17}N_3$ compact mixed by dry ball milling. This figure is reproduced from "Consolidation of $Sm_2Fe_{17}N_3$ magnets with Sm-based eutectic alloy binder" by Otogawa, K; Takagi, K; Asahi, T. *Journal oh Alloys and Compounds* **2018**, 746C, 19-26, Elsevier, copyright 2018.

3.3.3 Evaluation of mixed powder

Prior to specific evaluation of the sintered compacts, the binder-added powder was evaluated at this section. Fig. 3.12 showed the cross-sectional images of typical particles in the binder-added powder. Note that in the EDX mapping images, the Fe distribution should be regarded as the distribution of $Sm_2Fe_{17}N_3$ particles, while the Cu distribution should be regarded as the distribution of the Sm-Fe-Cu-Al alloys. Each mapping image showed that the Sm-Fe-Cu-Al and $Sm_2Fe_{17}N_3$ particles maintained a granular form and did not construct core/shell structure $Sm_2Fe_{17}N_3$ particles wrapped with the binder layer as expected. However, the Sm-Fe-Cu-Al powder was confirmed to be dispersed homogeneously by a wide area observation.

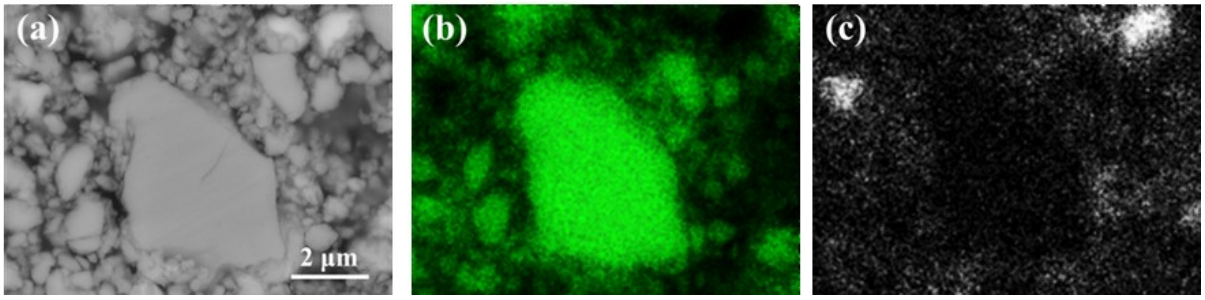

Figure 3.12 Cross-sectional images of the Sm-Fe-Cu-Al binder added $Sm_2Fe_{17}N_3$ powder. (a) SEM BSE image. (b) EDX Fe-mapping image. (C) EDX Cu-mapping image. This figure is reproduced from "Consolidation of $Sm_2Fe_{17}N_3$ magnets with Sm-based eutectic alloy binder" by Otogawa, K; Takagi, K; Asahi, T. *Journal oh Alloys and Compounds* **2018**, 746C, 19-26, Elsevier, copyright 2018.

Fig. 3.13 showed a comparison of the demagnetization curves of the binder-added $Sm_2Fe_{17}N_3$ powder, the raw $Sm_2Fe_{17}N_3$ powder and the milled additive-free $Sm_2Fe_{17}N_3$ powder. The coercivities of the raw powder, the additive-free powder and the binder-added powder were 11.9, 12.2 and 12.6 kOe, respectively. The coercivities of the two kinds of dry ball-milled powders were slightly higher than that of the raw powder. These slight increases in coercivity might be caused by refinement of the $Sm_2Fe_{17}N_3$ powder during dry ball milling, but this effect was negligible. Meanwhile, the saturation magnetizations were estimated using the law of approach to saturation magnetization from these demagnetization curves. The calculated saturation magnetizations of the raw powder, the milled additive-free powder and the binder-added powder were 150.3, 150.2 and 117.8 emu/g, respectively. The mixing of the binder resulted in a decrease of about 20% in saturation magnetization, which virtually agreed with the mixing ratio of the paramagnetic binder powder. This result demonstrates that, the mixing of the Sm-Fe-Cu-Al fine powders and raw $Sm_2Fe_{17}N_3$ powders by the dry ball milling produces a homogeneously dispersed mixed powder and induces no deterioration of the magnetic properties of the raw $Sm_2Fe_{17}N_3$.

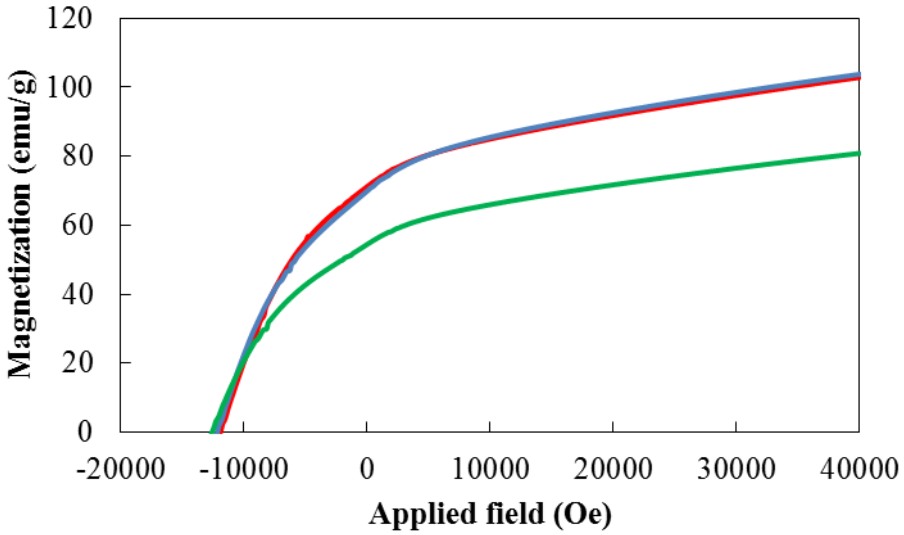

Figure 3.13 Demagnetization curves of the raw $Sm_2Fe_{17}N_3$ powder (red line), the milled additive-free $Sm_2Fe_{17}N_3$ powder (blue line) and the milled binder-added powder (green line). This figure is reproduced from "Consolidation of $Sm_2Fe_{17}N_3$ magnets with Sm-based eutectic alloy binder" by Otogawa, K; Takagi, K; Asahi, T. *Journal oh Alloys and Compounds* **2018**, 746C, 19-26, Elsevier, copyright 2018.

3.3.4 Evaluation of sintered compacts

Subsequently, the availability of the addition of the Sm-Fe-Cu-Al binder alloy on the $Sm_2Fe_{17}N_3$ sintered compacts was examined. This study limited the production of sintered compact to isotropic compacts and did not include anisotropic ones, because the initial study focused on the most important determining criteria such as the formation of a liquid phase and restraint of the coercivity decrease. At first, the binder-added and additive-free $Sm_2Fe_{17}N_3$ powders, which were both prepared via the dry ball-milling process, were sintered at 550°C. At this sintering temperature, which was higher than the melting point of the Sm-Fe-Cu-Al alloy as shown in Chapter 2, the Sm-Fe-Cu-Al binder was expected to be transformed into liquid phase. The Cross-sectional SEM-BSE and EDX Cu-mapping images

of the binder-added sintered compact were shown in Fig 3.14 (a) and (b). The SEM-BSE image showed that submicron thick white phases surrounded the grains. The Cu-distribution, moreover, corresponds to the distribution of the white phases. Therefore, the white phases in the SEM-BSE image were identified to be the Sm-Fe-Cu-Al binder phase or its derived phase. The EDX semi-quantitative elemental analyses of the grain center and grain boundary of the binder-added compact also showed that the elemental compositions (at%) of these were Sm : Fe : Cu: Al = 10.9 : 88.3 : 0.4 : 0.4 and 24.3 : 68.1 : 5.0 : 2.6, respectively. Note that as EDX point analyses inevitably detect the characteristic X-ray emitted from about 1μm region, the mentioned elemental composition of the grain boundary might include that of the $Sm_2Fe_{17}N_3$ grain. Therefore, the composition of the grain boundary presented above might not indicate an exact composition of the grain boundary, but at least suggested that the constituent elements of the Sm-Fe-Cu-Al alloy were concentrated at the grain boundary. Moreover, the Sm-Fe-Cu-Al phase formed continuous layers at the grain boundary. This result supports the expectation that the Sm-Fe-Cu-Al alloy functions as a binder for $Sm_2Fe_{17}N_3$ sintering.

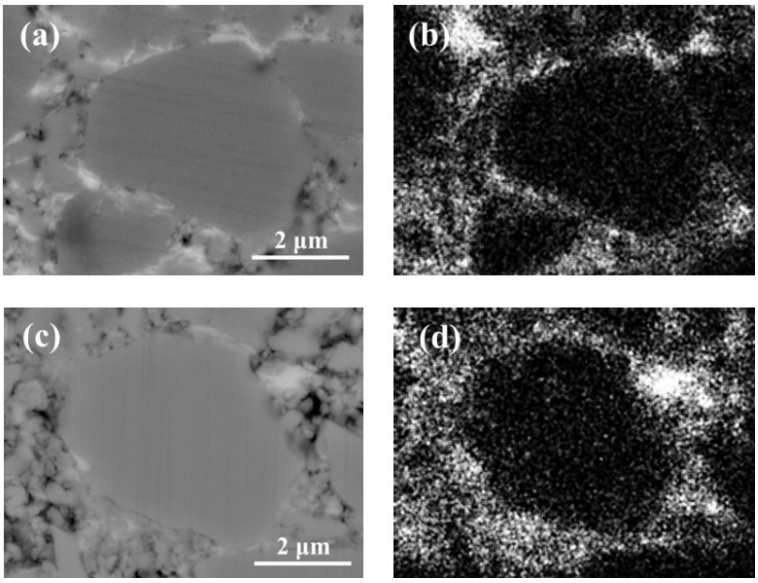

Figure 3.14 Cross-sectional SEM-BSE images of Sm-based alloy-added $Sm_2Fe_{17}N_3$ compacts hot-pressed at (a) 550°C and (c) 300°C. Cross-sectional EDX Cu-mappings of alloy-added $Sm_2Fe_{17}N_3$ compacts hot-pressed at (b) 550°C and (d) 300°C. This figure is reproduced from "Consolidation of $Sm_2Fe_{17}N_3$ magnets with Sm-based eutectic alloy binder" by Otogawa, K; Takagi, K; Asahi, T. *Journal oh Alloys and Compounds* **2018**, 746C, 19-26, Elsevier, copyright 2018.

The formation of the Sm-Fe-Cu-Al layers at grain boundary was expected to improve the magnetic properties of the sintered compacts. To confirm this possibility, the demagnetization curves of the binder-added and additive-free $Sm_2Fe_{17}N_3$ compacts sintered at 550℃ were measured as shown in Fig. 3.15. As mentioned in Chapter 1, Zn-bonded $Sm_2Fe_{17}N_3$ sintered compacts, which are the most successful metal-bonded $Sm_2Fe_{17}N_3$ sintered compact to date, show an excess reduction ratio of magnetization, in that the reduction ratio is approximately twice as large as the binder additive ratio [6,7]. As clarified above, mixing of the Sm-Fe-Cu-Al binder did not cause an excessive decrease in saturation magnetization. The saturation magnetizations of the additive-free and binder-added sintered compacts were calculated from Fig. 3.15 to be 149.2 and 116.5 emu/g. Thus, even after

sintering, the reduction ratio due to binder addition was about 20%. This reduction ratio was the same as the binder additive ratio, which means that the Sm-Fe-Cu-Al alloy binder, unlike Zn binders, did not affect the magnetization of the magnetic phase adversely. This innocuous property of the Sm-Fe-Cu-Al binder is a significant advantage compared to the previous metal binder.

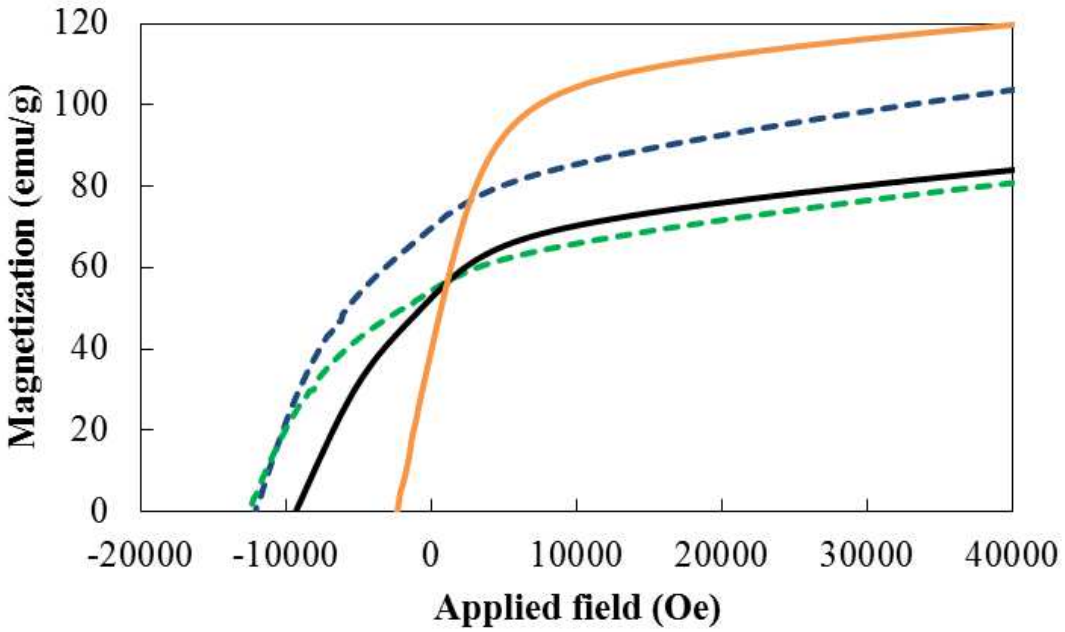

Figure 3.15 Demagnetization curves of the sintered compacts and powders. Yellow line: additive-free $Sm_2Fe_{17}N_3$ compact sintered at 550°C, black line: binder-added $Sm_2Fe_{17}N_3$ compact sintered at 550°C, blue broken line: milled additive-free $Sm_2Fe_{17}N_3$ powder and green broken line: milled binder-added $Sm_2Fe_{17}N_3$ powder. This figure is reproduced from "Consolidation of $Sm_2Fe_{17}N_3$ magnets with Sm-based eutectic alloy binder" by Otogawa, K; Takagi, K; Asahi, T. *Journal oh Alloys and Compounds* **2018**, 746C, 19-26, Elsevier, copyright 2018.

More importantly, in Fig. 3.15, the Sm-Fe-Cu-Al binder-added $Sm_2Fe_{17}N_3$ sintered compact showed a slight decrease in coercivity from the powder, whereas the additive-free $Sm_2Fe_{17}N_3$

sintered compact showed one-fifth decrease in coercivity from the powder. Previous report [8] proposed that the main cause of the decrease in coercivity of the $Sm_2Fe_{17}N_3$ during sintering was the formation of α-Fe phases near the sintered interfaces, i.e., the grain boundaries. Therefore, the state or amount of α-Fe phases was expected to be different between the additive-free and binder-added $Sm_2Fe_{17}N_3$ sintered compacts. In order to identify the phase constitution of each compact, XRD analyses of the additive-free and binder-added $Sm_2Fe_{17}N_3$ compacts sintered at 550 ˚C were performed, as shown in Fig. 3.16 (a) and (b). Rhombohedral $Sm_2Fe_{17}N_3$ (ICDD card No.00-048-1790) and cubic α-Fe (ICDD card No.00-006-0696) peaks were identified in both XRD profiles. However, the peak intensity of α-Fe in the binder-added sintered compact was less than one-third of that in the additive-free sintered compact. Consequently, this indicates that the Sm-Fe-Cu-Al binder alloy restrained the formation of the α-Fe phase during sintering, resulting in conservation of coercivity. There are two inferences of the mechanisms to restrain the formation of α-Fe. A previous study proposed that, the α-Fe phases are formed by the redox reaction between the surface oxide layer and the $Sm_2Fe_{17}N_3$ main phase. Therefore, one of the possibilities is that the surface oxide layers, which are the origin of the α-Fe phases, were removed by the Sm-Fe-Cu-Al binder. Otherwise, the precipitated α-Fe phases were reacted with the Sm-Fe-Cu-Al binder into a certain nonmagnetic alloy. In this connection, the EDX result of the sintered compact indicated that the Sm-Fe-Cu-Al alloy were concentrated at the grain boundary. However, any other peaks were not identified from the XRD profile except for $Sm_2Fe_{17}N_3$ and α-Fe peaks. The XRD profile of the Sm-Fe-Cu-Al alloy ingot, which is same as XRD profile of Fig. 2.16, was shown as a green broken line in Fig. 3.16 (b). Each of the Sm-Fe-Cu-Al peaks were near the peaks of $Sm_2Fe_{17}N_3$ or α-Fe. For this reason, identification of the diffraction peak that was derived from the Sm-Fe-Cu-Al alloy possibly got into difficulties. In addition, comparing the XRD profile of the binder-added and additive-free $Sm_2Fe_{17}N_3$ powders, which were shown in Fig. 3.16 (e) and (f), the

binder-added $Sm_2Fe_{17}N_3$ powder also did not show any other peaks which were derived from the Sm-Fe-Cu-Al alloy except for the slight cubic Sm_2O_3 diffraction peak. The specific observation of the grain boundary by TEM characterization is performed in Chapter4.

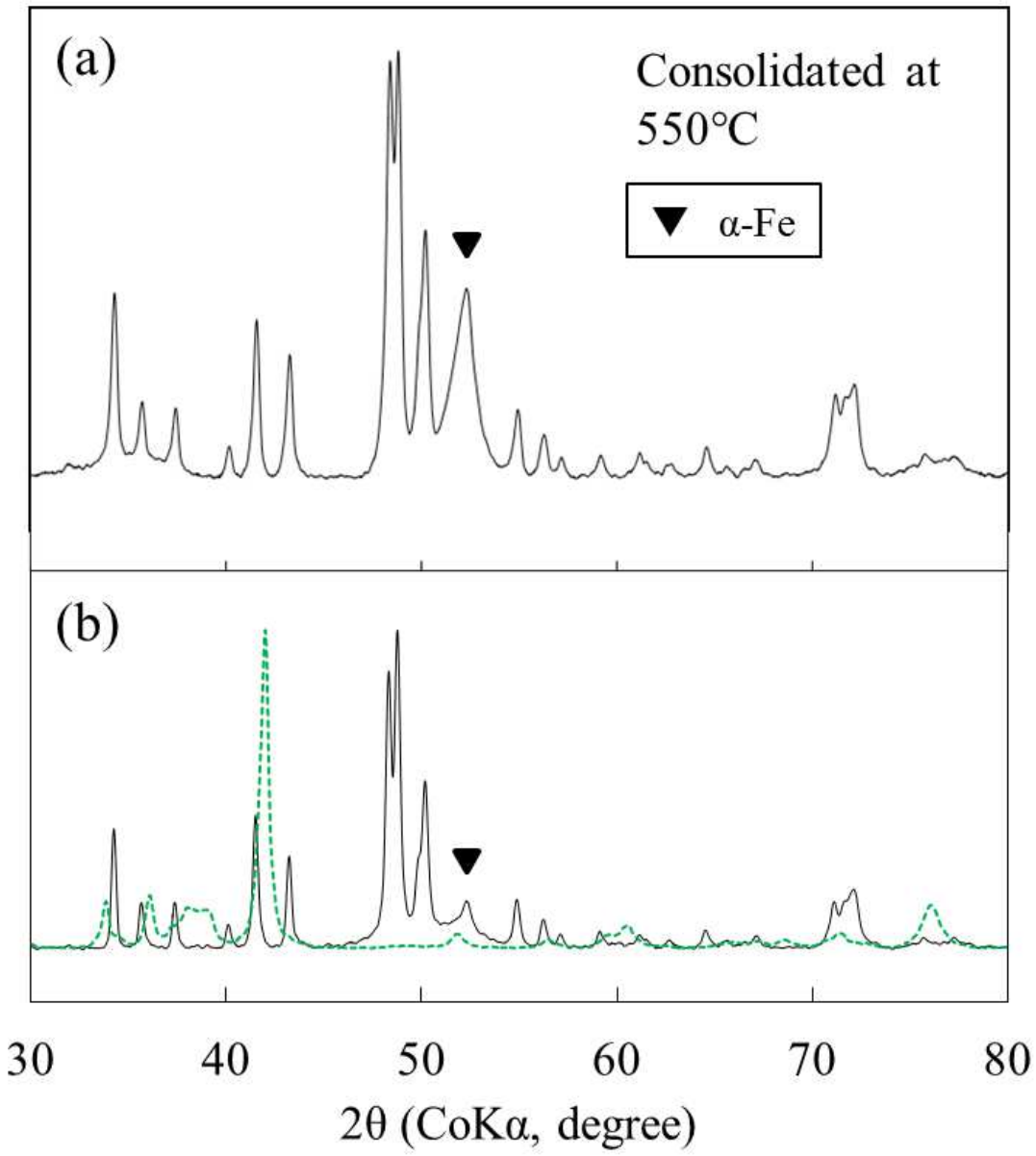

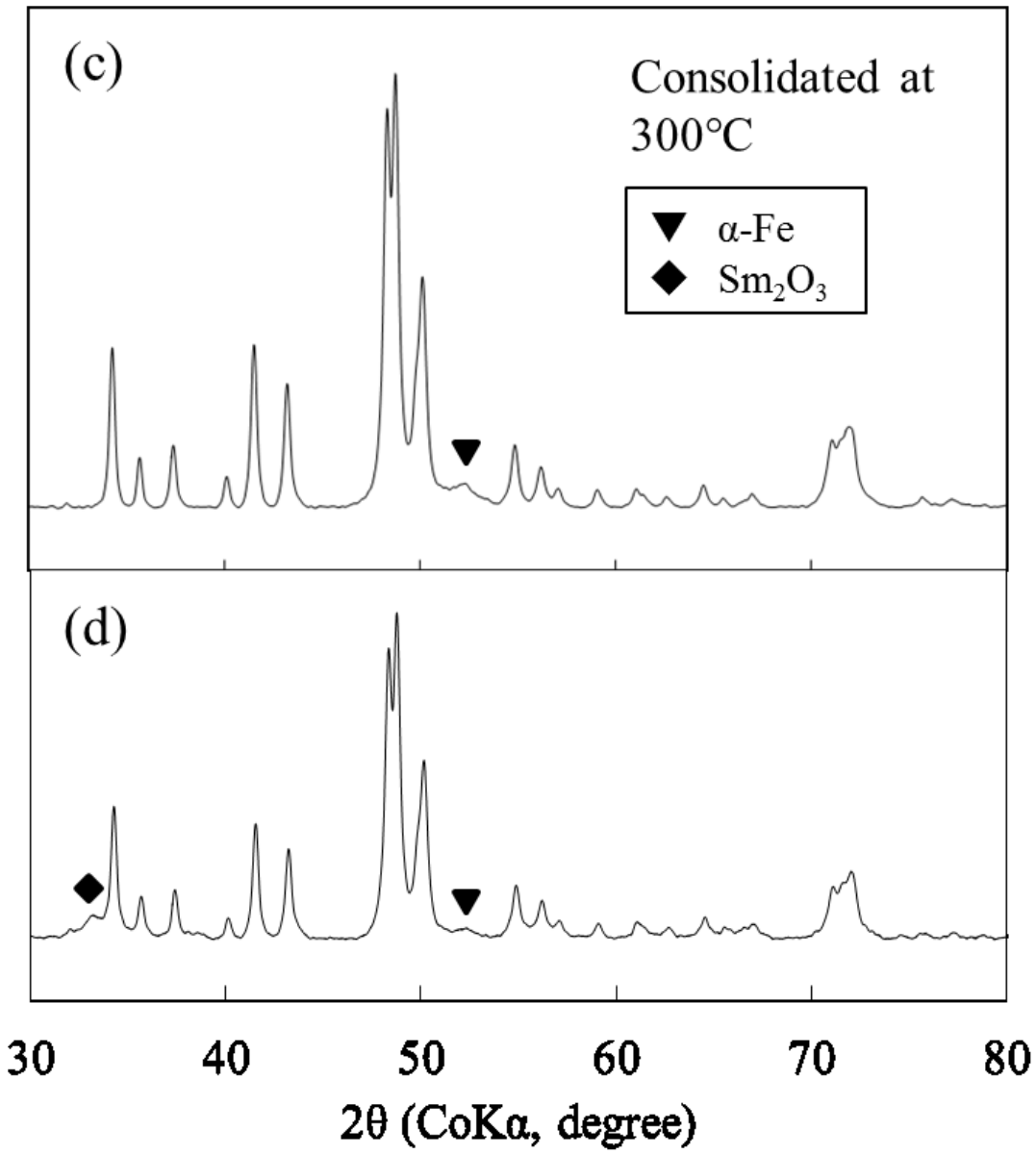
(c)
Consolidated at 300°C
α-Fe
Sm2O3
(d)
30
40
50
60
70
80
2θ (CoKα, degree)

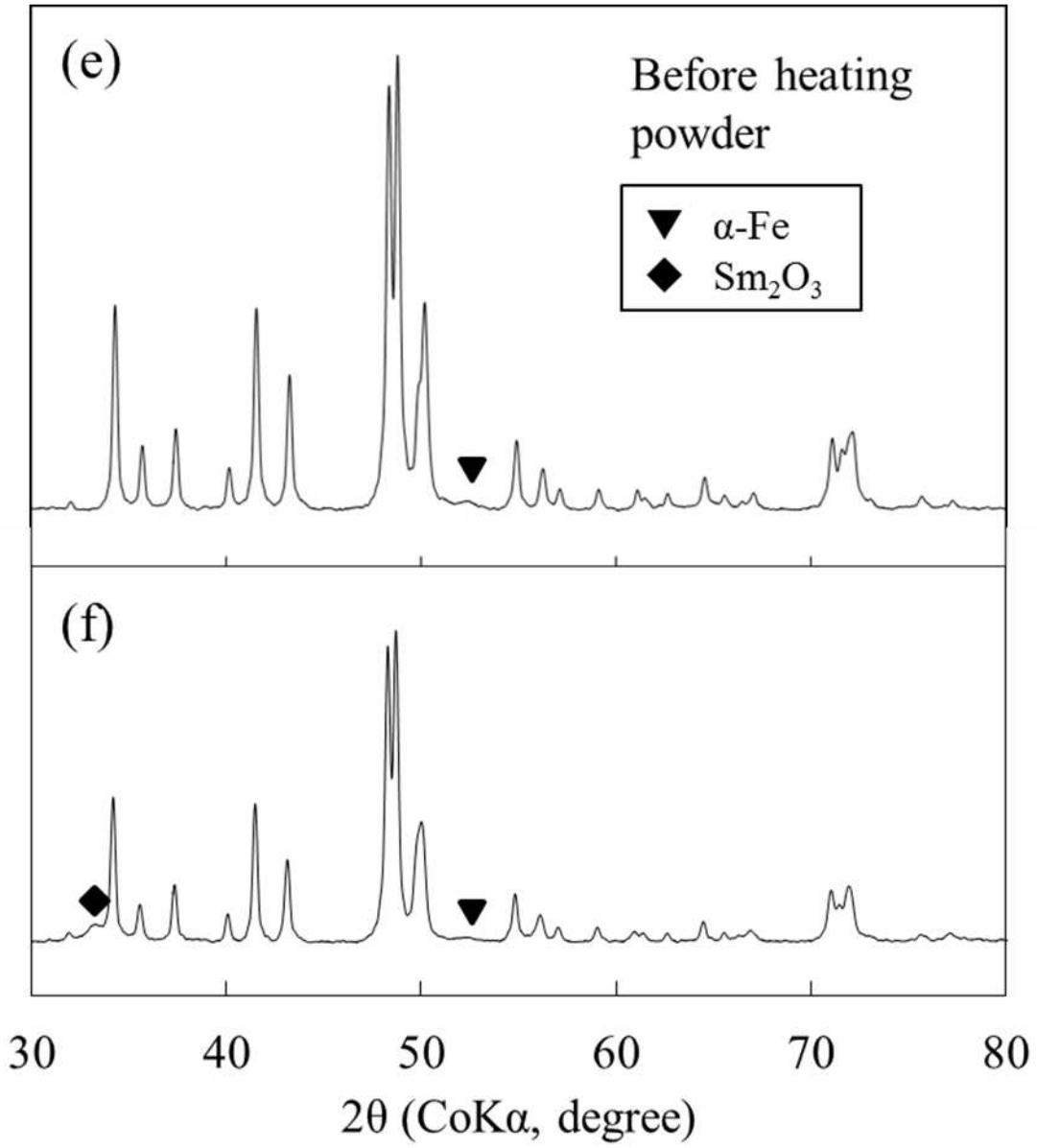

Figure 3.16 X-ray diffraction profiles of (a) additive-free and (b) Sm-based alloy-added $Sm_2Fe_{17}N_3$ compacts hot-pressed at 550°C, (c) additive-free and (d) alloy-added $Sm_2Fe_{17}N_3$ compacts hot-pressed at 300°C and (e) additive-free and (f) alloy-added $Sm_2Fe_{17}N_3$ powders. The green broken line in (b) is the prolife of the $Sm_{63}Fe_5Cu_{22}Al_{10}$ alloy ingot. This figure is reproduced from "Consolidation of $Sm_2Fe_{17}N_3$ magnets with Sm-based eutectic alloy binder" by Otogawa, K; Takagi, K; Asahi, T. *Journal oh Alloys and Compounds* **2018**, 746C, 19-26, Elsevier, copyright 2018.

Remanences of the milled additive-free $Sm_2Fe_{17}N_3$ powder, additive-free $Sm_2Fe_{17}N_3$ compact sintered at 550°C, milled binder-added $Sm_2Fe_{17}N_3$ powder and binder-added $Sm_2Fe_{17}N_3$ compact sintered at 550°C were 69.70, 40.91, 54.42 and 52.49 emu/g, respectively. The remanence of the additive-free $Sm_2Fe_{17}N_3$ was greatly decreased by sintering. This decrease in remanence might be caused by α-Fe phase because magnetic moment of the soft magnetic α-Fe phase may be easily inversed by diamagnetic field. On the other hand, the Sm-Fe-Cu-Al binder-added $Sm_2Fe_{17}N_3$ showed slight decrease in remanence by sintering. These differences in the remanence between additive-free and binder-added $Sm_2Fe_{17}N_3$ were consistent with the amount of formed α-Fe phase.

The binder-added and additive-free $Sm_2Fe_{17}N_3$ powders were sintered at various temperatures. The dependences of coercivity on the sintering temperature of the additive-free and binder-added $Sm_2Fe_{17}N_3$ sintered compacts were shown Fig. 3.17 in comparison with that in the literature [8]. The coercivity of the additive-free $Sm_2Fe_{17}N_3$ sintered compacts showed a considarable decrease against rising of sintering temperature. This decreasing behavior in coercivity totally coincided with the reported result. Both sintered compacts were common to be produced from air-exposed powders, i.e., powders having the surface oxide layer. As mentioned above, the surface oxide causes decrease in coercivity due to the formation of α-Fe phases near the grain surfaces. In contrast, even though the binder-added $Sm_2Fe_{17}N_3$ sintered compacts were also produced from the air-exposed $Sm_2Fe_{17}N_3$ powder, they maintained the coercivity of the raw powder sufficiently up to the sintering temperature of 550 ˚C.

Figure 3.17 Dependence of coercivity on the sintering temperature of the additive-free (red) and binder-added (blue) $Sm_2Fe_{17}N_3$ sintered compacts. The green triangles represent the

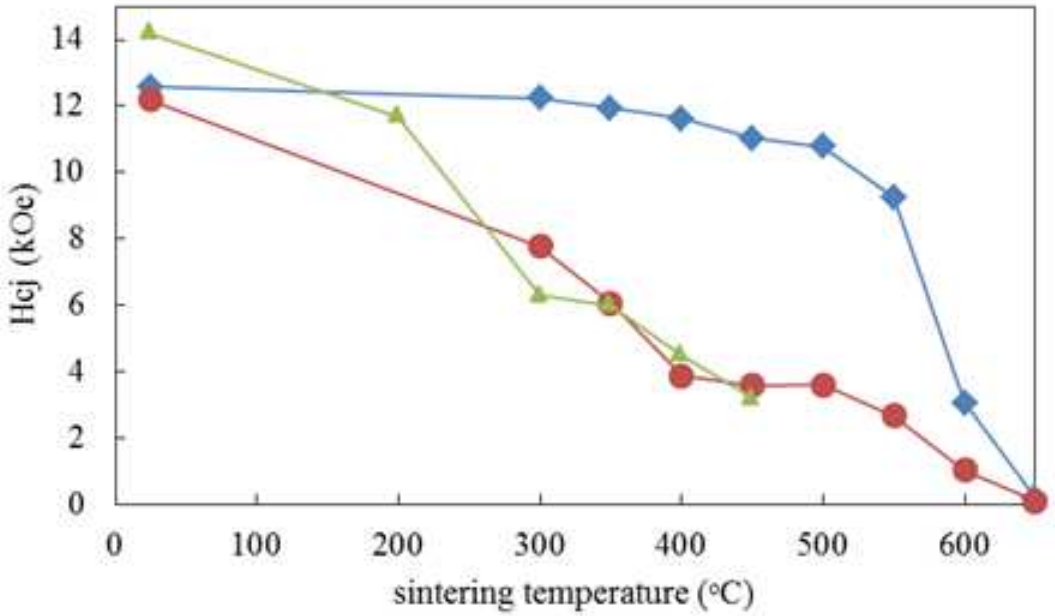

results in the literature that reported results for $Sm_2Fe_{17}N_3$ sintered compacts [8]. This figure is reproduced from "Consolidation of $Sm_2Fe_{17}N_3$ magnets with Sm-based eutectic alloy binder" by Otogawa, K; Takagi, K; Asahi, T. *Journal oh Alloys and Compounds* **2018**, 746C, 19-26, Elsevier, copyright 2018.

Interestingly, the restraining effect of the binder alloy on the formation of α-Fe phase and hence, the coercivity decrease was also exerted at low sintering temperatures even below the melting point of the binder alloy, as can be seen in Fig. 3.17. For example, the additive-free compact sintered at 300 ˚C showed the coercivity decrease, but the binder-added sintered compact showed no decrease. A cross-sectional SEM-BSE image of the binder-added $Sm_2Fe_{17}N_3$ compact sintered at 300 ˚C was shown in Fig. 3.14 (c). The binder particles maintained their spherical shape even after sintering at 300 ˚C, unlike the compact sintered at 550 ˚C as shown in Fig. 3.14(a). Therefore, the Sm-Fe-Cu-Al alloy seemed not to wrap the $Sm_2Fe_{17}N_3$ grains as a binder. However, as shown in Fig. 3.14 (d), the Cu-mapping indicated that Cu lightly surrounded the $Sm_2Fe_{17}N_3$ grains. As shown in Fig. 3.12, the binder-added $Sm_2Fe_{17}N_3$ powder has no obvious Cu-concentrated layer on its surface before sintering.

These results suggest that the binder alloy thinly surrounds the $Sm_2Fe_{17}N_3$ grains by a grain boundary or surface diffusion effect, even though they are sintered below the melting point of the binder alloy. Comparing the XRD profiles of the additive-free and the binder-added $Sm_2Fe_{17}N_3$ compacts sintered at 300 ˚C (Fig. 3.16 (c) and (d)), the peak intensity of α-Fe in the binder-added sintered compact was less than two-thirds of that in the binder-free sintered compact. Therefore, in spite of the low sintering temperature, the formation of α-Fe phase was reasonably restrained by the Sm-Fe-Cu-Al binder, and as a result, the coercivity of the powder might be maintained. Deepening the consideration, from the XRD results in Fig. 3.16,the amount of α-Fe phase in the binder-added $Sm_2Fe_{17}N_3$ compact sintered at 550 ˚C was estimated to be more than twice as much as that in the additive-free compact sintered at 300℃. Nevertheless, the coercivity of the binder-added compact sintered at 550 ˚C was remarkably higher, by 2.5 kOe, than that of the additive-free compact sintered at 300 ˚C. This contradiction implies that there would be a second reason for the suppression of the coercivity decrease by the Sm-Fe-Cu-Al binder in addition to restraint of α-Fe precipitation. Fig. 3.18 shows a schematic image of the hypothesis of the second reason of the coercivity maintenance effect. Previous report indicated that $Sm_2Fe_{17}N_3$ sintered magnets produced from air-exposed $Sm_2Fe_{17}N_3$ powders showed thin oxide layer with a thickness of about 30nm at the grain boundaries [8]. Therefore, most of the precipitated α-Fe phases consequently exist near the $Sm_2Fe_{17}N_3$ grain. These α-Fe phases might act as a nucleation site of reverse magnetic domain. On the other hand, as shown in Fig. 3.14, the binder-added $Sm_2Fe_{17}N_3$ sintered compacts showed thick grain boundary layer with a thickness of about few 100 nm. Therefore, most of the precipitated α-Fe phases exist far from the $Sm_2Fe_{17}N_3$ grain and consequently amount of nucleation sites of reverse magnetic domain might be few. However, to verify this hypothesis, further evidence is demanded.

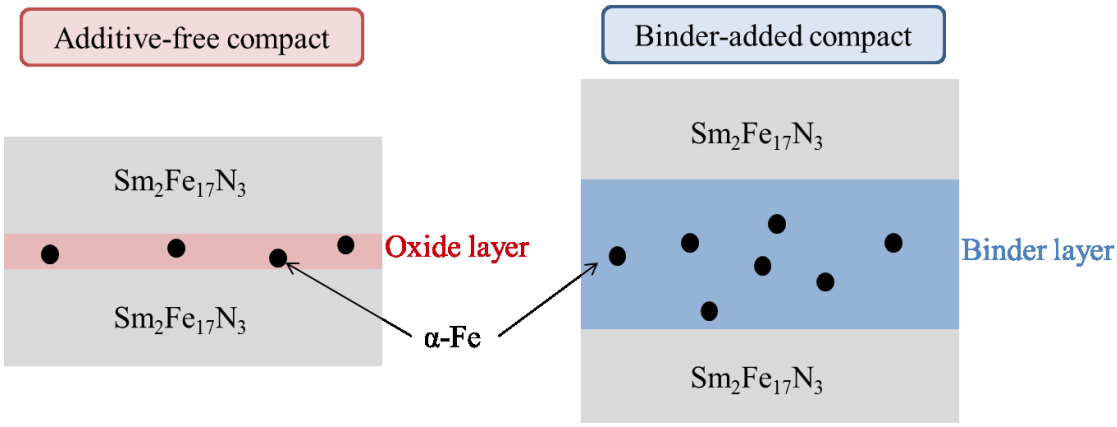

Figure 3.18 Hypothesis of second reason for coercivity maintenance effect.

Meanwhile, the relative densities of the additive-free compacts prepared at 300°C and 550°C were determined to be 79.7 and 84.1%, respectively. These densities were reasonable values compared to conventional hot-pressed $Sm_2Fe_{17}N_3$ magnets [21]. On the other hand, the alloy-added compacts hot-pressed at 300°C and 550°C showed relative densities of 82.8% and 94.1%, respectively. It may be noted that the relative densities of the alloy-added compacts were simply calculated from the theoretical density of $Sm_2Fe_{17}N_3$ (7.67 g/cm^3), the measured density of the Sm-Fe-Cu-Al bulk (7.37 g/cm^3) and their mixing ratio (20%), assuming that no reaction and no phase transition occurred during hot-pressing. With the hot-pressing temperature of 550°C, the alloy-added compacts exhibited much higher relative densities than the additive-free compacts. This implied that the binder alloy melted and infiltrated into the interparticle spaces. Therefore, the developed Sm-Fe-Cu-Al alloy can certainly be expected to fulfill the role of a metal binder. However, based on the present results, it is difficult to discuss whether this alloy had an effect of promoting densification of the main phase like that observed in liquid phase sintering. This is due to the large amount of alloy (20%) used in the powder mix; that is, even assuming a full dense compact was prepared from the powder mixture, the volume fraction of the main $Sm_2Fe_{17}N_3$ phase would not surpass 80%, and this low volume fraction is not suitable for a quantitative evaluation of the densification promotion effect. However, as this is considered an important issue, a

detailed study of the densification effect of the developed alloy should be studied in future.

3.4 Conclusion

In this chapter, to reveal the effect of the Sm-Fe-Cu-Al binder alloy on the magnetic properties of the $Sm_2Fe_{17}N_3$ sintered compacts, Sm-Fe-Cu-Al bonded $Sm_2Fe_{17}N_3$ sintered compacts were produced and those properties were evaluated. At first, the Sm-Fe-Cu-Al alloy ingot was pulverized with wet ball milling method which is a general powder metallurgy technique. The pulverized Sm-Fe-Cu-Al powders as a sintering binder were mixed with raw $Sm_2Fe_{17}N_3$ powders by wet or dry ball milling method. The sintered compact from binder-added powder, which was mixed with wet ball milling method, showed that, the Sm-Fe-Cu-Al binder alloy were unevenly distributed and the binder alloy was not permeated into grain boundary. On the other hand, the sintered compact from binder-added powder, which was mixed with dry ball milling method, showed that the Sm-Fe-Cu-Al alloy were homogeneously distributed and permeated into grain boundary. Observation of the mixed powder revealed that the mixing with dry ball milling method already dispersed the binder powder homogeneously at the step of mixing. While the conventional Zn binder decreases the saturation magnetization of sintered compacts due to an excess reaction with $Sm_2Fe_{17}N_3$ phase, the developed Sm-Fe-Cu-Al binder did not affect the magnetization of the $Sm_2Fe_{17}N_3$ sintered compacts adversely. Most importantly, conventional sintering of $Sm_2Fe_{17}N_3$ powder has always resulted in a serious decrease in coercivity against rising sintering temperature, but the binder-added sintered compacts maintained the coercivity of the raw powder over a wide range of sintering temperatures. The main cause of this coercivity maintenance effect was considered to restraint of α-Fe precipitation by the Sm-Fe-Cu-Al binder.

3.5 References

[1] M. Sagawa, S. Fujimura, N. Togawa, H. Yamamoto, Y. Matsuura, New material for permanent magnets on a base of Nd and Fe (invited), Journal of Applied Physics. 55 (1984) 2083–2087. doi:10.1063/1.333572.

[2] T.T. Sasaki, T. Ohkubo, K. Hono, Structure and chemical compositions of the grain boundary phase in Nd-Fe-B sintered magnets, Acta Materialia. 115 (2016) 269–277. doi:10.1016/j.actamat.2016.05.035.

[3] T. Kohashi, K. Motai, T. Nishiuchi, S. Hirosawa, Magnetism in grain-boundary phase of a NdFeB sintered magnet studied by spin-polarized scanning electron microscopy, Applied Physics Letters. 104 (2014) 1–6. doi:10.1063/1.4883487.

[4] A. Sugawara, K. Ueda, T. Nakayama, N. Lee, H. Yamamoto, Measuring magnetisation reversal in micron-sized Nd2Fe14B single crystals by microbeam x-ray magnetic circular dichroism, Journal of Physics D: Applied Physics. 49 (2016) 1–7. doi:10.1088/0022-3727/49/42/425001.

[5] R. Soda, K. Takagi, M. Jinno, W. Yamaguchi, K. Ozaki, Anisotropic Sm2Fe17N3 sintered magnets without coercivity deterioration, AIP Advances. 6 (2016). doi:10.1063/1.4967364.

[6] P.A.P. Wendhausen, D. Eckert, A. Handstein, K.H. Müller, G. Leitner, R. Skomski, On the role of Zn in Sm2Fe17Nx permanent magnets, Journal of Applied Physics. 73 (1993) 6044–6046. doi:10.1063/1.353464.

[7] K. Makita, S. Hirosawa, Coercivity of Zn evaporation-coated Sm2Fe17Nx fine powder and its bonded magnets, Journal of Alloys and Compounds. 260 (1997) 236–241. doi:10.1016/S0925-8388(97)00155-2.

[8] K. Takagi, H. Nakayama, K. Ozaki, Microstructural behavior on particle surfaces and interfaces in Sm2Fe17N3 powder compacts during low-temperature sintering, Journal of Magnetism and Magnetic Materials. 324 (2012) 2336–2341.

doi:10.1016/j.jmmm.2012.02.021.

Chapter 4

Development of Sintering Process to Maximize the Potential of the Sm-based Alloy Binder for Improvement of the Magnetic Properties of $Sm_2Fe_{17}N_3$ Compacts

4.1 Introduction

In chapter 3, the Sm-Fe-Cu-Al bonded $Sm_2Fe_{17}N_3$ sintered compacts were produced and the magnetic properties of those compacts were evaluated. The Sm-Fe-Cu-Al alloy has a very low melting temperature of 495 ˚C. Therefore, if this Sm-based alloy binder melts and surrounds the $Sm_2Fe_{17}N_3$ grains below the decomposition temperature of $Sm_2Fe_{17}N_3$, it is expected to remove the surface oxide layer due to the strong reducing ability of the element Sm, and removal of the surface oxide layer is expected to result in prevent coercivity decrease against rising sintering temperature[1–3]. Actually, the Sm-Fe-Cu-Al alloy bonded $Sm_2Fe_{17}N_3$ sintered compacts were proved to maintain the coercivity of the raw powder. Therefore, this is considered to be an attractive material for producing high-performance magnets by further development to enhance both coercivity and densification. However, at the moment, even the mechanism of the coercivity maintenance effect has not been clarified. Therefore, to maximize the potential of the Sm-Fe-Cu-Al binder for improvement of the magnetic properties of $Sm_2Fe_{17}N_3$, further knowledge of the effect of the binder is needed.

Hence, this chapter examined the potential of the Sm-Fe-Cu-Al binder for improvement of the magnetic properties of $Sm_2Fe_{17}N_3$, in particular the coercivity recovery effect of this binder. At first, specific microstructural observation was conducted for the Sm-Fe-Cu-Al bonded $Sm_2Fe_{17}N_3$ compacts prepared in Chapter 3 in order to discuss the interfacial reaction between the binder and the grain surface. Following this, to explore the possibility of further improvement of coercivity, the Sm-Fe-Cu-Al alloy was added to raw $Sm_2Fe_{17}N_3$

powder by jet milling method and sputter coating method, and these binder-added powders were sintered. Based on the evaluation on the magnetic properties of these sintered compacts, the prospects for developing a new high-performance magnet were discussed. This chapter is partly reproduced from “Coercivity Recovery Effect of Sm-Fe-Cu-Al alloy on $Sm_2Fe_{17}N_3$ Magnet” by Otogawa, K; Asahi, T; Jinno, M; Yamaguchi, W; Takagi, K; Kwon, H. *Journal of the Korean Physical Society* **2018**, in press, Korean Physical Society, copyright 2018.

4.2 Materials and methods

4.2.1 Materials

As mentioned at section 2.2.2, the button ingot of the mother $Sm_{63}Fe_5Cu_{22}Al_{10}$ alloy with a diameter of 60mm was prepared by a cold crucible melting method from Sm ingot (>99.9%), Fe foil (>99.99%), Cu grain (>99.0%) and Al plate (>99.99%). A commercial $Sm_2Fe_{17}N_3$ powder (Sumitomo Metal Mining Co., Ltd.) was used as raw $Sm_2Fe_{17}N_3$ powder. Note that surface of the commercial $Sm_2Fe_{17}N_3$ powder was already oxidized because it was exposed to the air.

4.2.2 Pulverizing of Sm-Fe-Cu-Al alloy by mortar

The Sm-Fe-Cu-Al alloy button ingot was first crushed by stamp mill (Fig. 4.1) into coarse chip. The coarse chip was ground by agate mortar (Fig. 4.2) to 1 mm diameter large grains and parts of grains were extracted. The grains were further ground and filtered with a 100μm of grid mesh. To avoid burning of the powders, above pulverization methods were performed in a glove box with a pure Ar gas atmosphere with a low oxygen concentration below 1 ppm. This powder was pulverized with below jet milling method.

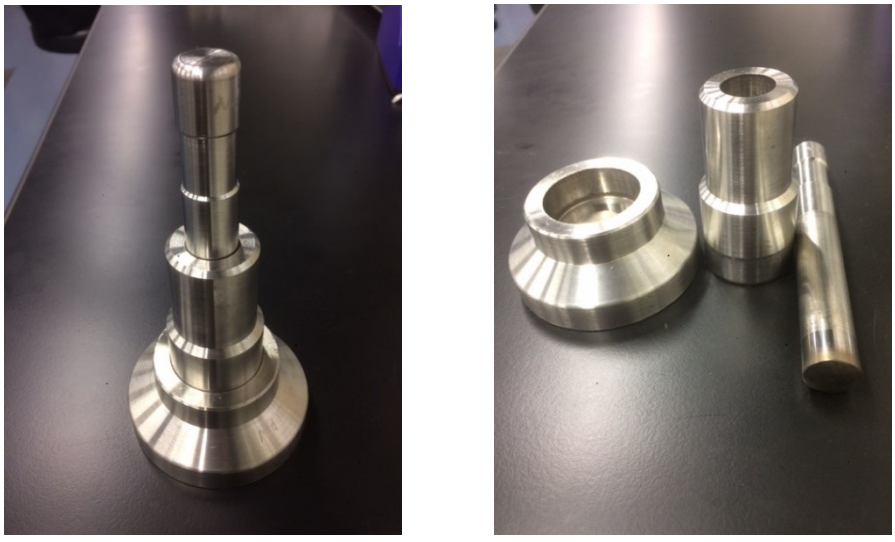

Figure 4.1 Stamp mill.

Figure 4.2 Agate mortar.

4.2.3 Jet milling method

The above Sm-Fe-Cu-Al powder was pulverized into fine powder with a jet milling method as shown in Fig. 4.3. Jet milling method conflicts grains by fast gas stream and these are pulverized. Because fracture surfaces of the grains have high-reactivity and these are easily aggregated, little amount of organic solvent is dropped as pulverization additive to prevent aggregation of the grains. However, required amount of solvent is much less than that of wet ball milling pulverization method. To prevent oxidation of the pulverized powder, following operations were performed in a glove box with a pure Ar gas atmosphere with a low oxygen concentration below 1 ppm. Nitrogen was used as pulverizing gas. Pressure of each pulverization and transportation was 1.5 MPa. Supply rate of material powders was 1 g/min. Acetonitrile (CH_3CN) was used as pulverization additive and was dropped at 0.1 mL/min. To prevent prepared fine powders, it was immersed in heptane. This fine powder was mixed with raw $Sm_2Fe_{17}N_3$ powder with dry ball milling method as mentioned at section 3.2.3 and 20wt% binder-added $Sm_2Fe_{17}N_3$ powder was prepared.

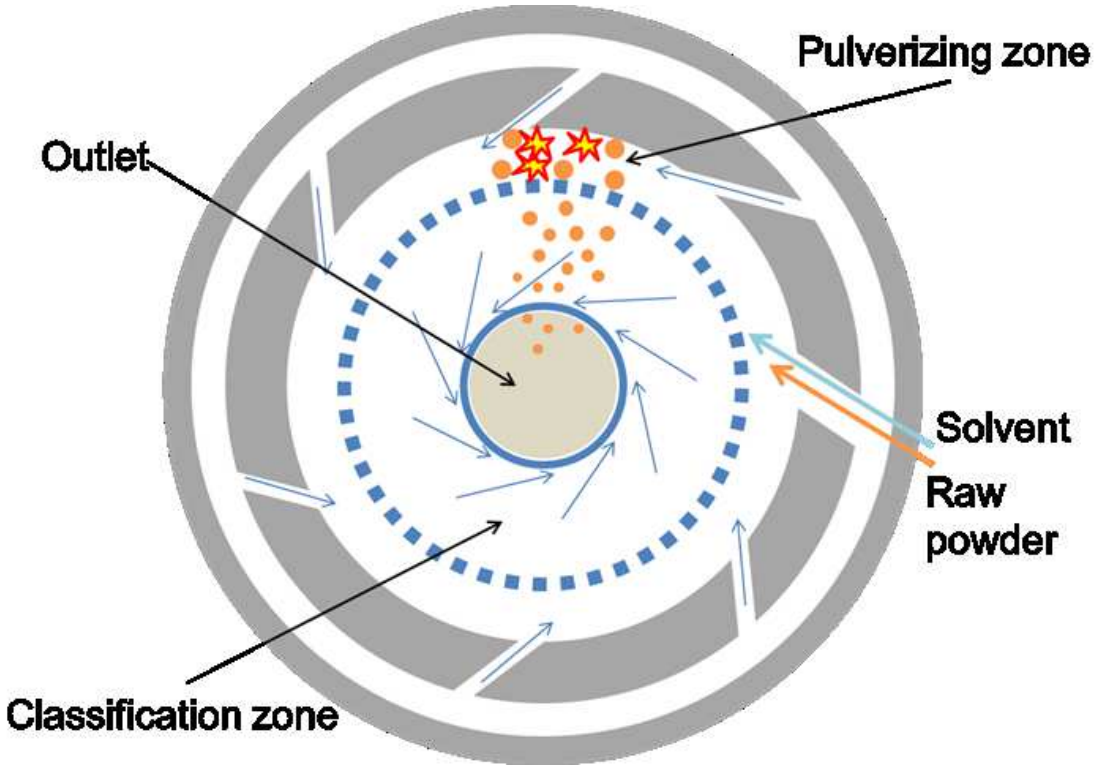

Figure 4.3 Schematic drawings of jet milling method

4.2.4 Sputter coating method

To add the Sm-Fe-Cu-Al alloy to $Sm_2Fe_{17}N_3$ without organic medium, the binder alloy was directly coated on the surface of $Sm_2Fe_{17}N_3$ particles by sputtering. A direct current (DC) magnetron sputtering apparatus coupled with a glove box was uniquely developed to prevent oxidation of the sputter-coated powder. An outline figure of the DC magnetron sputtering method is shown in Fig. 4.4. A sputtering target of 50 mm in diameter and 5 mm in thickness was cut from the Sm-Fe-Cu-Al button ingot. 15 g of the commercial $Sm_2Fe_{17}N_3$ powder was put into a vessel equipped with automatic stirring apparatus. The distance of vessel-to-target was 150 mm. Prior to deposition, the sputtering chamber was evacuated to a pressure of 1×10^{-4} Pa. Pure Ar gas was introduced to the operating pressure of 0.45 Pa. The supplied electricity was 70 W. Total deposition time was 50 hours. The sputter-coated powder was immersed in a heptane to prevent oxidation.

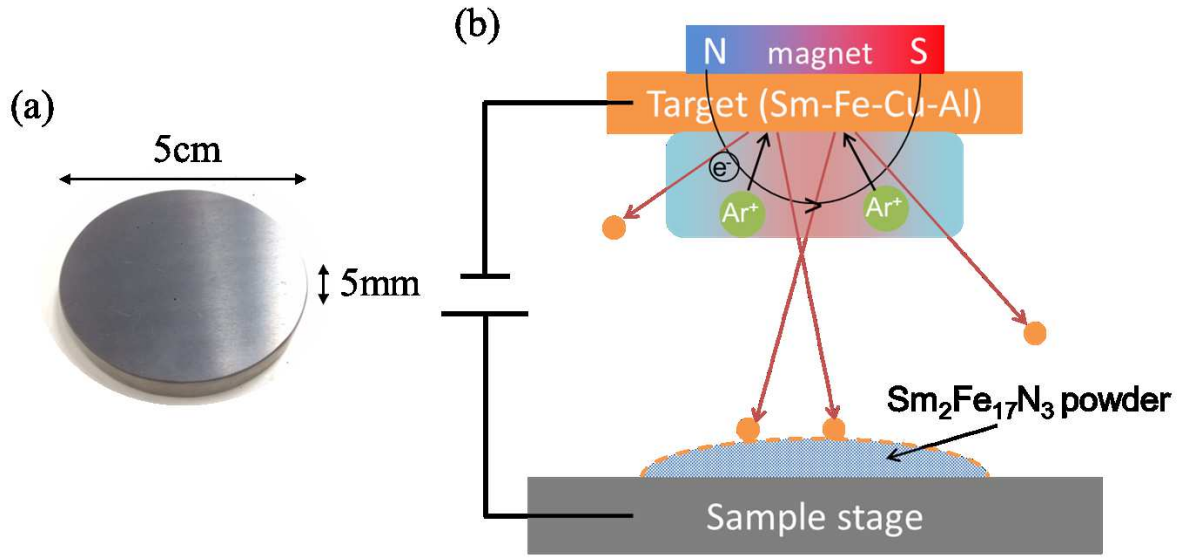

Figure 4.4 (a) sputter target and (b) schematic drawing of DC magnetron sputtering.

4.2.5 Sintering method

The prepared powders were sintered. Sintering process was same as section 3.2.4.

4.2.6 Carbon and nitride analyses

The concentrations of carbon and nitrogen in the alloy ingot, the prepared powders and the sintered compacts were measured with a carbon analyzer (EMIA-110, Horiba, Japan) (Fig. 4.5) and nitrogen analyzer (EF-620, Horiba, Japan) (Fig. 4.6). Each sample was inevitably exposed to air prior to the measurement.

Figure 4.5 Carbon analyzer.

Figure 4.6 Nitrogen analyzer.

4.2.7 XRF analysis

Quantitative elemental analyses of the prepared powders were performed with an X-ray fluorescence spectrometer (XRF; EDX-8000, Shimadzu, Japan) (Fig. 4.7). Each sample was inevitably exposed to air prior to the measurement.

Figure 4.7 XRF apparatus.

4.2.8 XPS analysis

The elemental composition of the surface of the prepared powders and the chemical bonding state of those elements were measured by X-ray photoelectron spectroscopy (XPS; PHI VersaProbeII, Ulvac-Phi, Japan) (Fig. 4.8). The samples were transported from glove box to XPS chamber with transfer vessel to restrain oxidation of the samples as few as possible.

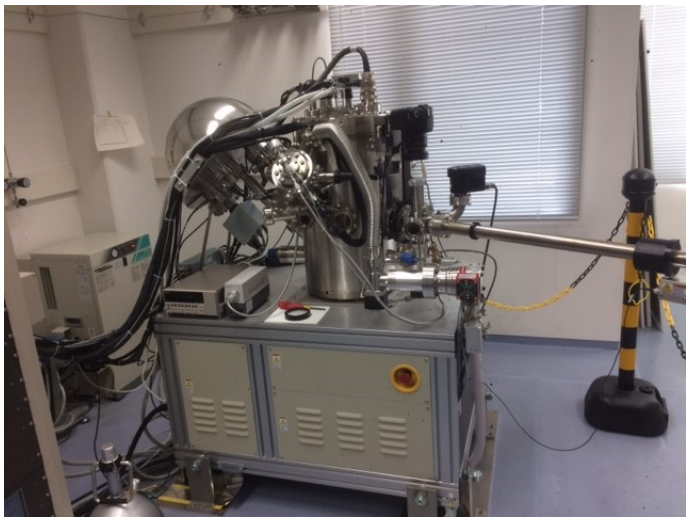

Figure 4.8 XPS apparatus.

4.2.9 X-ray diffraction measurement

Phase identifications of the prepared powders and the sintered compacts were performed by X-ray diffractometry using Co Kα radiation (XRD; Empyrean, Panalytical, Netherlands) (Fig. 2.9). Surface of the powders and cross-section of the sintered compacts were measured. Measuring method was θ-2θ method. 45kV and 40mA of electric current was applied to Co target. Width of radiation beam was 10mm and it was radiated 500s per 0.013°.

4.2.10 Magnetic property measurement

The coercivities of the prepared samples were measured with a pulse B-H tracer (PBH-1000, Nihon Denjisokki Co., Japan) (Fig. 3.7). An external magnetic field was applied up to 55 kOe.

4.2.11 Density measurement

The absolute densities of the sintered compacts were measured by the Archimedes method. To avoid persistence of bubble at the surface voids, the surface voids of sintered magnets were filled with paraffin.

4.2.12 Microstructural observation

The microstructures of the prepared powders and the sintered compacts were observed as following methods. Microstructure observation and elemental distribution analyses of the prepared powders and sintered compacts were performed with EDX equipped FE-SEM apparatus (Fig. 2.8). Cross-sections of the prepared powders and sintered compacts were processed by polishing with diamond paste. Especially, the sintered compact, which was produced in Chapter 3, was processed into thin sample by FIB to observe with transmission electron microscope (TEM). Semi-quantitative elemental analysis of selected areas and precise microstructural observation of this this sample were performed with TEM apparatus

(EM-2100F, JEOL, Japan) equipped with an EDX analyzer (JED-2300, JEOL, Japan).

4.3 Results and discussions

4.3.1 TEM observation of Sm-Fe-Cu-Al bonded $Sm_2Fe_{17}N_3$ sintered magnet.

Many researchers have reported that the coercivities of $Sm_2Fe_{17}N_3$ are drastically decreased against rising sintering temperature[1–3]. Actually, as indicated in Chapter 3, the coercivity of additive-free $Sm_2Fe_{17}N_3$ powder was decreased against rising sintering temperature. The mechanism of this coercivity decrease was proposed as follows [4]. Commonly-available $Sm_2Fe_{17}N_3$ powders are exposed to air and naturally have an oxide layer on the particle surface. The following redux reaction takes place between the primary $Sm_2Fe_{17}N_3$ phase and the surface oxide layer upon heating:

$Fe_2O_3(FeO) + Sm_2Fe_{17}N_3 \rightarrow \alpha\text{-Fe} + Sm_2O_3 + N_2\uparrow$

The α-Fe phase which are precipitated by this reaction act as nucleation sites for the reverse magnetic domain. This precipitation of α-Fe results in the reported decrease of coercivity. Because amount of precipitated α-Fe phases increases with increasing sintering temperature, the coercivity of $Sm_2Fe_{17}N_3$ sintered magnets decreases depending on the sintering temperature.

However, the milled Sm-Fe-Cu-Al alloy-added $Sm_2Fe_{17}N_3$ sintered compacts, which were produced in Chapter 3, maintained the coercivity of the raw powder well, as shown in Fig. 3.17. It was also confirmed that the addition of the milled Sm-Fe-Cu-Al alloy restrained the precipitation of α-Fe compared with the additive-free compacts. Therefore, the coercivity maintenance effect of the Sm-Fe-Cu-Al binder was estimated to be exerted by the restraint of the α-Fe precipitation derived from the surface oxide layer.

To confirm the estimated mechanism of the coercivity maintenance effect of the Sm-Fe-Cu-Al alloy, TEM observation was conducted for the cross-section of a milled Sm-Fe-Cu-Al binder-added $Sm_2Fe_{17}N_3$ compact that was produced by wet ball milling and sintered at 550 ˚C. In particular, the whereabouts of the surface oxide layer of the $Sm_2Fe_{17}N_3$ grains were focused on. Fig. 4.9 (a) showed a TEM cross-sectional image of a thin sample

which was processed by FIB from the central part of the milled binder-added $Sm_2Fe_{17}N_3$ sintered compact. The gray region, which occupies the upper left, was the Sm-Fe-Cu-Al binder phase, and the black region, which occupies the lower right, is the $Sm_2Fe_{17}N_3$ phase. Previous report indicated that $Sm_2Fe_{17}N_3$ sintered magnet produced from air-exposed $Sm_2Fe_{17}N_3$ powders showed 30 nm thickness of the oxide layer at the grain boundaries [4]. This oxide layers at the grain boundaries were derived from the surface oxide layer of the $Sm_2Fe_{17}N_3$ particles. In general, $Sm_2Fe_{17}N_3$ powders are known to have a 10 to 20 nm oxide layer on the particle surface [5]. On the other hand, TEM observation of the milled binder-added $Sm_2Fe_{17}N_3$ sintered compact found no oxide layer around the surface of the $Sm_2Fe_{17}N_3$ grain. This is confirmed by the fact that, as shown in Fig. 4.9 (b) and (c), the lattice fringe of the central $Sm_2Fe_{17}N_3$ crystal continued to the grain surface without misorientation. This suggested that no oxide phase existed near the interface between the $Sm_2Fe_{17}N_3$ prime phase and the Sm-Fe-Cu-Al phase. It is noted that EDX was difficult to analyze accurate oxide distribution of the thin sample because both the Sm-Fe-Cu-Al and $Sm_2Fe_{17}N_3$ phases were easily oxidized so as to become indistinct. These results suggested that the Sm-Fe-Cu-Al alloy removed the surface oxide layer of the $Sm_2Fe_{17}N_3$ grains. Therefore, these observation results support the inference that the coercivity maintenance effect is attributed to the removal of the surface oxide layer by the Sm-Fe-Cu-Al binder.

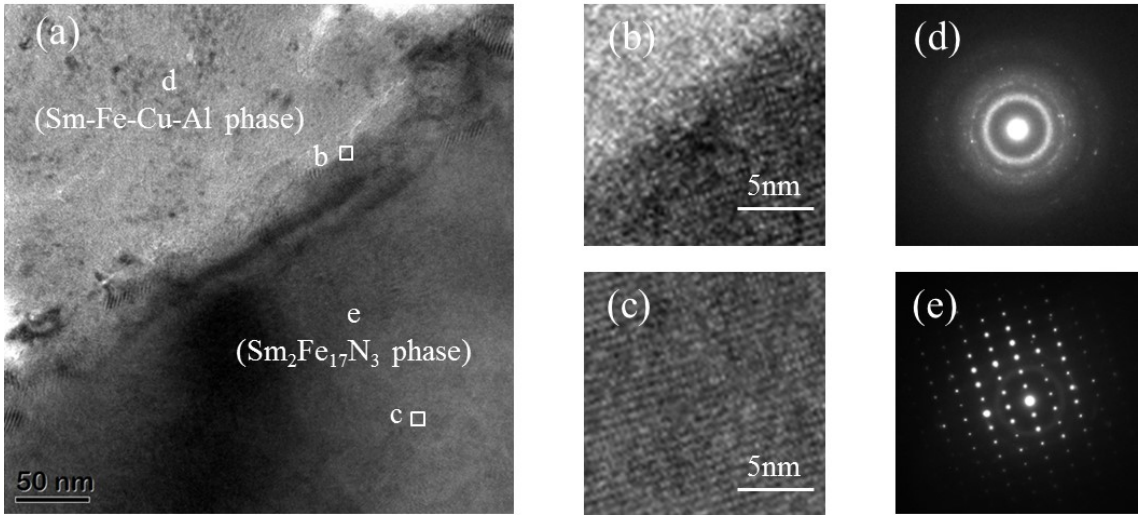

Figure 4.9 TEM cross-sectional images of (a) the interface between $Sm_2Fe_{17}N_3$ phase (region (d)) and Sm-Fe-Cu-Al phase (region (e)), (b) and (c) magnified regions squared in (a) for the milled binder added $Sm_2Fe_{17}N_3$ compact sintered at 550 ˚C. The electron diffraction patters of (d) Sm-Fe-Cu-Al phase and (e) $Sm_2Fe_{17}N_3$ phase. This figure is reproduced from "Coercivity Recovery Effect of Sm-Fe-Cu-Al alloy on $Sm_2Fe_{17}N_3$ Magnet" by Otogawa, K; Asahi, T; Jinno, M; Yamaguchi, W; Takagi, K; Kwon, H. *Journal of the Korean Physical Society* **2018**, in press, Korean Physical Society, copyright 2018.

In addition, EDX analysis of the Sm-Fe-Cu-Al binder phase detected the characteristic X-rays of carbon and nitride. The measured weight ratio was Sm : C : N = 1 : 0.25 : 0.12. The quantitativity of light elements by EDX is not precise. However, this result certainly showed that part of the Sm-Fe-Cu-Al alloy was carbonized and nitrided. Fig. 4.9 (d) showed the selected area electron diffraction image of the Sm-Fe-Cu-Al phase. This electron diffraction image indicated that the Sm-Fe-Cu-Al phase was composed of very fine crystallite because the Drbye-Scherrer ring was formed. Actually, as shown in Fig. 4.9 (b), a clear lattice fringe was not observed in the binder layer, and the crystal size seemed to be several nanometers. This nanocrystallization of the Sm-Fe-Cu-Al phase was speculated to

occur due to the strain introduce by ball milling or the existence of interstitial carbon and nitride atoms. However, as shown in Fig. 4.9 (e), the $Sm_2Fe_{17}N_3$ grain showed a very clear diffraction pattern of the $Sm_2Fe_{17}N_3$ crystal, i.e., high crystallinity without strain. This implied that ball milling did not give sufficient energy to introduce the large strain necessary for nanocrystallization. Therefore it was suggested that the Sm-Fe-Cu-Al phase might have been nanocrystallized by carbonization and nitridization.

4.3.2 Elemental analyses of binder alloy

Because carbonization and nitridization might influence the functions of the binder, we focused on when these reactions took place. Two possibilities were proposed. The first possibility was the pulverization process by wet ball milling. That is, the highly reactive fracture surface of the Sm-Fe-Cu-Al alloy might react with pulverization medium of acetonitrile (CH_3CN). The second possibility was the sintering process, as the Sm-Fe-Cu-Al phase might react with the residual acetonitrile enclosed in the interstices between particles during heating. Therefore, the carbon and nitrogen concentrations in the Sm-Fe-Cu-Al button ingot, the milled Sm-Fe-Cu-Al powder, the raw $Sm_2Fe_{17}N_3$ powder and the sintered additive-free $Sm_2Fe_{17}N_3$ compact were measured with carbon and nitrogen analyses. Whereas the carbon and nitrogen concentrations of the Sm-Fe-Cu-Al button ingot were 0.07 wt% and 0.11 wt%, those of the milled powder were 11.61 wt% of carbon and 2.24 wt% of nitrogen. Therefore, the pulverization by wet ball milling was revealed to caused carbonization and nitridization of the binder alloy. In contrast, whereas the carbon and nitrogen conventrations of the raw $Sm_2Fe_{17}N_3$ powder were 0.05 wt% and 3.42 wt%, those of the sintered additive-free $Sm_2Fe_{17}N_3$ compact was 0.17 wt% and 3.45 wt%. Thus, while sintering process seemed to increase the carbon and nitrogen concentrations slightly, these values were within the measurement error range. From this, it can be concluded that most of the carbonization and nitridization occurred during wet ball milling and not during sintering

process.

4.3.3 Wettability of the liquid phase Sm-Fe-Cu-Al to the $Sm_2Fe_{17}N_3$ surface.

As carbonization and nitridization of the binder would improve its melting point, it was strongly suggested that the formation of the grain boundary layer of the Sm-Fe-Cu-Al alloy phase of the milled binder-added $Sm_2Fe_{17}N_3$ compact sintered at 550 ˚C, which was shown in Fig. 3.14 (a) and (b), was caused by surface diffusion effect and not caused by formation of the liquid phase. Therefore, the wettability of the Sm-Fe-Cu-Al liquid on the $Sm_2Fe_{17}N_3$ surface could not be evaluated from aforementioned results. To evaluate wettability, 1 mm diameter large Sm-Fe-Cu-Al grains which was certainly not contaminated was filled with raw $Sm_2Fe_{17}N_3$ powder and sintered at 550 ˚C. Cross-sectional images of the sintered compact were shown in Fig. 4.10. A low magnification image (Fig. 4.10 (a)) showed that large Sm-Fe-Cu-Al grains were connected by narrow Sm-Fe-Cu-Al path. This obviously showed that phase transition of the Sm-Fe-Cu-Al solid phase into liquid phase generated crack due to introduction of strains in the compact and the liquid phase flowed into the crack. In addition, middle-magnification image (Fig. 4.11 (b)) showed that Sm-Fe-Cu-Al liquid phases were permeated into inter particles of the $Sm_2Fe_{17}N_3$. High-magnification image (Fig. 4.11 (c)) showed that the $Sm_2Fe_{17}N_3$ grains were wrapped with Sm-Fe-Cu-Al phase. In case the Sm-Fe-Cu-Al liquid has poor wettability on the $Sm_2Fe_{17}N_3$ surface, liquid phase may not wrap main phase and voids are generated at the grain boundary. Consequently, this result indicated good wettability of the Sm-Fe-Cu-Al liquid on the $Sm_2Fe_{17}N_3$ surface. Therefore, it is suggested that contamination-free Sm-Fe-Cu-Al binder may promote densification of $Sm_2Fe_{17}N_3$ compact.

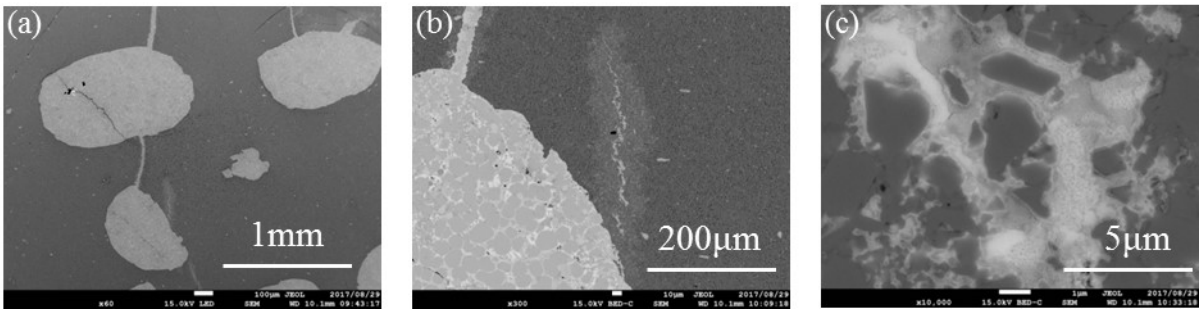

Figure 4.10 SEM cross-sectional images of Sm-Fe-Cu-Al large grain buried $Sm_2Fe_{17}N_3$ 550℃ sintered magnet. (a) low-magnification, (b) middle-magnification and (c) high-magnification image.

4.3.4 Jet milled Sm-Fe-Cu-Al powder added $Sm_2Fe_{17}N_3$ sintered compact

As shown in above, the Sm-Fe-Cu-Al liquid was not permeated into whole inter particles in the large Sm-Fe-Cu-Al grain buried $Sm_2Fe_{17}N_3$ sintered compact. An advanced pulverization method was attempted to produce non carbonized and nitrided Sm-Fe-Cu-Al fine powder. To obtain homogeneously mixed Sm-Fe-Cu-Al alloy added $Sm_2Fe_{17}N_3$ powder, it is desirable to pulverize the Sm-Fe-Cu-Al ingot into about 3μm diameter particles, which is the mean diameter of the raw $Sm_2Fe_{17}N_3$ powder. As pulverization with mortar reached the limit of several tens of diameter powder as shown in Fig. 4.11 (a), this powder was further pulverized with jet milling method. Note that, jet milling method requires much less amount of organic solvent than wet ball milling method. Mean diameter of 1 μm particles were prepared with jet milling.

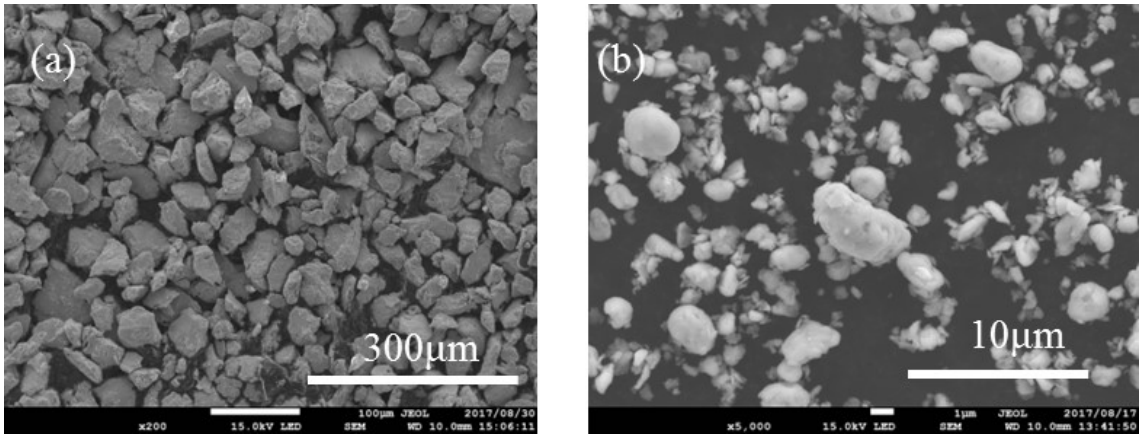

Figure 4.11 SEM images of (a) mortar grinded and (b) jet milled Sm-Fe-Cu-Al powder.

To evaluate whether jet milling prevent carbonization and nitridization of the Sm-Fe-Cu-Al powder, carbon and nitrogen concentration of the jet milled powder was measured with carbon and nitrogen analyses. The result was shown in Table 4.1 with the results of wet ball milled powder and bulk ingot. Amount of carbon and nitrogen in the jet milled powder was much smaller than that of the wet ball milled powder, but slightly higher than that of the bulk ingot. Therefore it was revealed that pulverization with jet milling restrained carbonization and nitridization of Sm-Fe-Cu-Al alloy but it could not prevent completely.

Table 4.1 Weight ratios of carbon and nitrogen in Sm-Fe-Cu-Al bulk ingot and powders.

	Bulk ingot	Wet ball milled powder	Jet milled powder
C (wt%)	0.05	11.61	0.96
N (wt%)	0.02	2.24	0.64

To examine the effect of the jet milled binder powder on the coercivity of sintered $Sm_2Fe_{17}N_3$ compact, the jet milled binder powder was mixed with raw $Sm_2Fe_{17}N_3$ powder by dry ball milling method , which was same as the method described in section 3.2.3, and this mixed powder was sintered at various temperatures. Fig. 4.12 shows the dependences of

coercivity on the sintering temperature of the jet milled binder-added $Sm_2Fe_{17}N_3$ sintered compacts in comparison with that of wet ball milled binder-added and additive-free $Sm_2Fe_{17}N_3$ sintered compacts. The coercivities of the jet milled binder-added sintered compacts were higher than that of additive-free sintered compacts but lower than that of wet ball milled binder-added sintered compacts. The cross-sectional images of the wet ball milled and jet milled binder-added $Sm_2Fe_{17}N_3$ compact sintered at 550 ˚C were shown in Fig. 4.13 (b) and (d). Whereas the wet ball milled binder-added sintered compact showed homogeneously dispersed Sm-Fe-Cu-Al phase at grain boundaries, the jet milled binder-added sintered compact showed uneven distribution of Sm-Fe-Cu-Al phase. This uneven distribution of Sm-Fe-Cu-Al might restrain coercivity improving effect of the Sm-Fe-Cu-Al binder alloy. In addition, the effect of carbon and nitrogen concentration of the binder on the coercivity of sintered compact was difficult to discuss because grain boundary condition was greatly different between wet ball milled binder added compact and jet milled binder added compact.

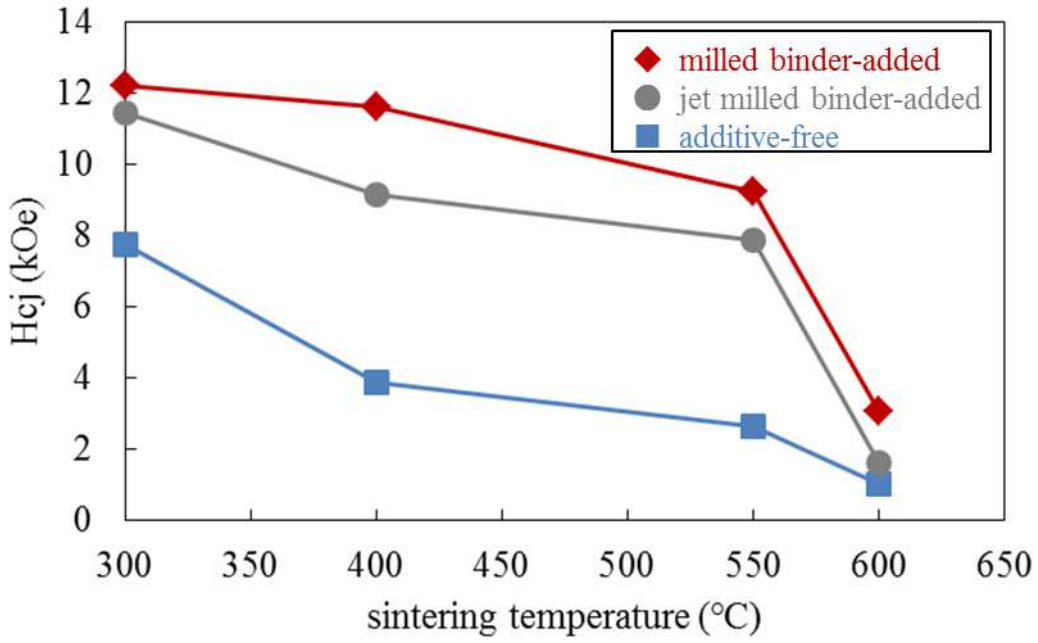

Figure 4.12 Dependence of coercivity on the sintering temperature of the wet ball milled binder-added (red), jet ball milled binder-added (gray) and additive-free (red) $Sm_2Fe_{17}N_3$ sintered compacts.

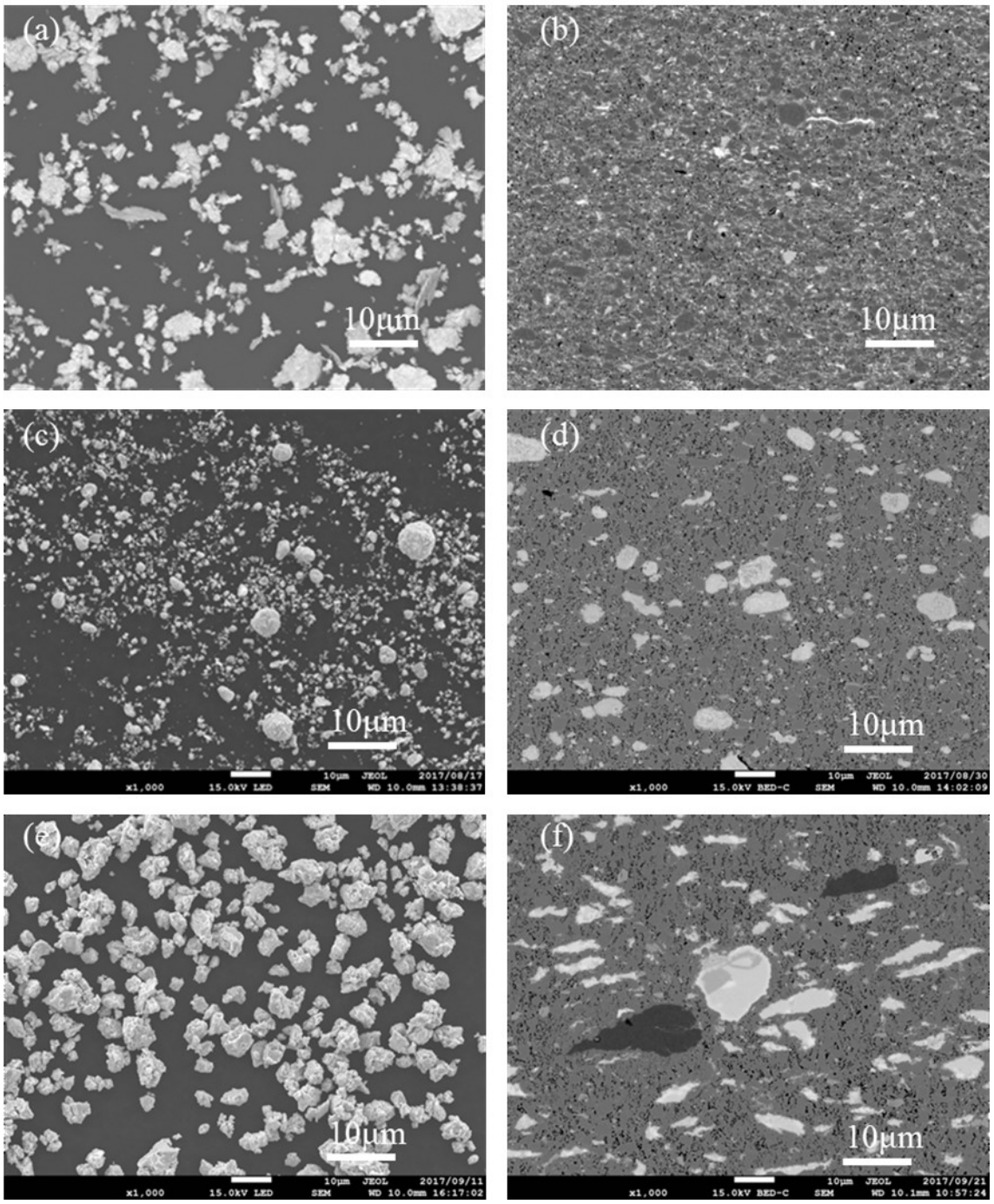

Figure 4.13 SEM images of pulverized powders and cross-sections of binder-added $Sm_2Fe_{17}N_3$ compacts sintered at 550 ˚C. (a) shows wet ball milled Sm-Fe-Cu-Al powder

using acetonitrile as pulverization medium and (b) shows the $Sm_2Fe_{17}N_3$ sintered compacts which was mixed with this powder. (c) shows jet milled Sm-Fe-Cu-Al powder and (d) shows the $Sm_2Fe_{17}N_3$ sintered compacts which was mixed with this powder. (e) shows wet ball milled Sm-Fe-Cu-Al powder using heptane as pulverization medium and (f) shows the $Sm_2Fe_{17}N_3$ sintered compacts which was mixed with this powder.

A hypothesis to explain the differences of binder distribution between wet ball milled binder-added compact and jet milled binder-added compact is proposed as follows. As shown in Fig. 4.13 (a) and (c), while the wet ball milled binder alloys were platelike shape, the jet milled binder alloys were spherical shape. As shown in Fig. 4.14 of the schematic drawing, whereas the spherical shape binder grains might difficult to be pulverized further when it was mixed with $Sm_2Fe_{17}N_3$ powder by dry ball milling method, the platelike shape binder grains might be pulverized further at that time. Therefore, wet ball milled binder-added mixed powder might contain further pulverized fine binder particles and these might be adsorbed on the $Sm_2Fe_{17}N_3$ surface. On the other hand, the jet milled binder particles might not be pulverized further and accordingly the binder particles were unevenly distributed. Actually, as shown in Fig. 4.13 (e) and (f), wet ball milled Sm-Fe-Cu-Al particles using heptane as pulverization medium were spherical shape and the Sm-Fe-Cu-Al phases were unevenly distributed in the sintered compact which was produced from mixed powder of this milled binder and $Sm_2Fe_{17}N_3$ powder. From the above results, it was suggested that to disperse the binder alloy homogeneously in grain boundary of sintered compact, shape of pulverized binder powder is important.

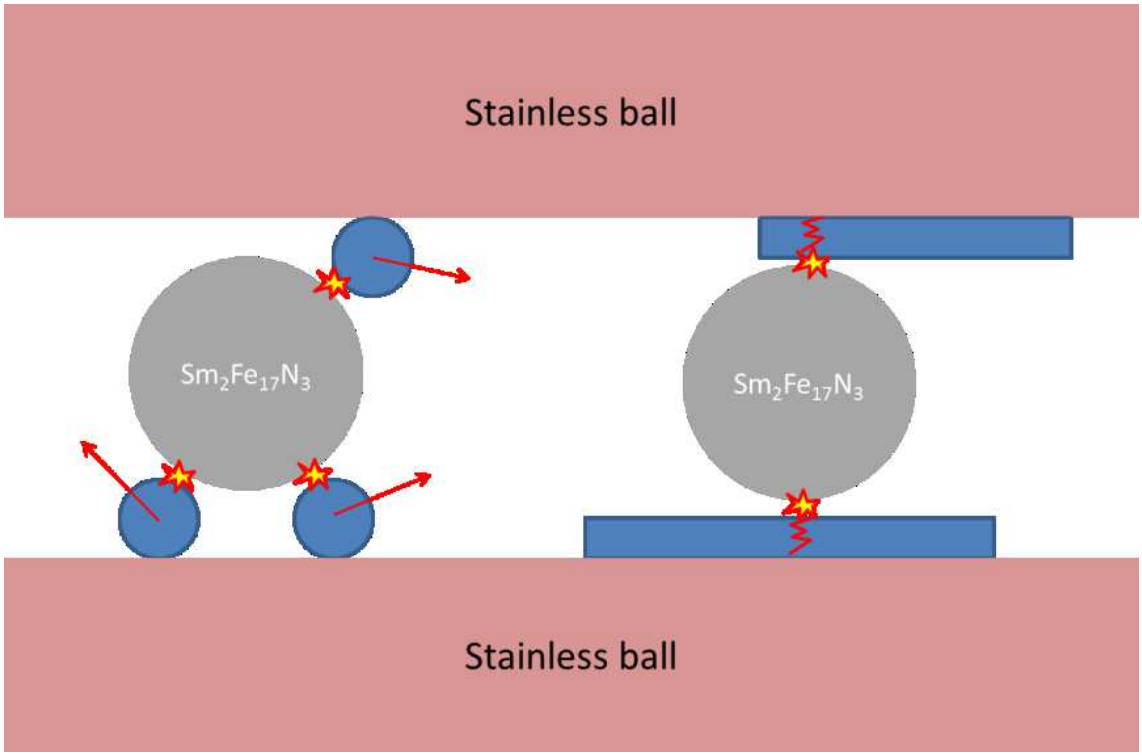

Figure 4.14 Schematic drawing of the hypothesis.

4.3.5 Sm-Fe-Cu-Al sputter coated $Sm_2Fe_{17}N_3$ sintered magnet

The Sm-Fe-Cu-Al alloy was carbonized and nitrided even if it was pulverized with jet milling. To avoid contamination from the organic medium used in pulverization, the Sm-Fe-Cu-Al alloy was directly coated on the surface of raw $Sm_2Fe_{17}N_3$ particles by sputtering. Sputter coating is an ideal method to uniformly add another kind of material to a powder without using an organic solvent. This sputter coated $Sm_2Fe_{17}N_3$ powder is called "binder-coated powder" in the following.

4.3.5.1 Evaluation of Sm-Fe-Cu-Al sputter coated $Sm_2Fe_{17}N_3$ powder

The binder-coated powder was evaluated prior to sinter this powder. The composition ratios of the binder-coated $Sm_2Fe_{17}N_3$ powder and the raw $Sm_2Fe_{17}N_3$ powder were measured by XRF analysis. From the difference between these composition ratios, the additive ratio of the binder alloy was calculated to be 3.4 wt%.

As shown in Fig. 4.15, SEM-EDX Cu-mapping revealed that the binder-coated powders were wholly surrounded by Cu, which is a constituent element of the binder. This suggested that the Sm-Fe-Cu-Al alloy was coated satisfactorily on the $Sm_2Fe_{17}N_3$ particles. Moreover, as shown in Fig 4.16 (a) to (c), the cross-sectional SEM-EDX mappings of Sm and Cu confirmed that Sm and Cu were continuously concentrated on the $Sm_2Fe_{17}N_3$ grain surfaces with thickness of a few to 50 nanometers. These results demonstrated that each of the $Sm_2Fe_{17}N_3$ grains was uniformly coated with the Sm-Fe-Cu-Al alloy.

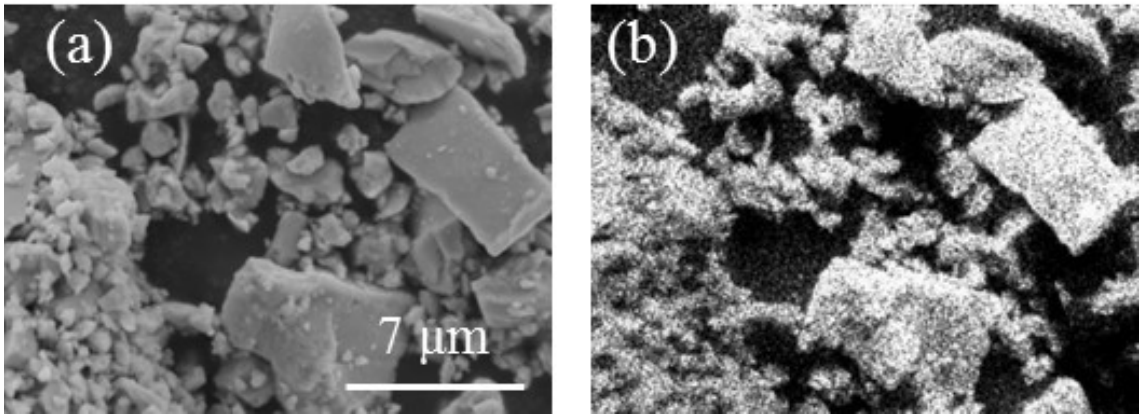

Figure 4.15 Surface SEM images of the Sm-Fe-Cu-Al coated $Sm_2Fe_{17}N_3$ powder. (a) SEM-BSE image and (b) EDX Cu-mapping. This figure is reproduced from "Coercivity Recovery Effect of Sm-Fe-Cu-Al alloy on $Sm_2Fe_{17}N_3$ Magnet" by Otogawa, K; Asahi, T; Jinno, M; Yamaguchi, W; Takagi, K; Kwon, H. *Journal of the Korean Physical Society* **2018**, in press, Korean Physical Society, copyright 2018.

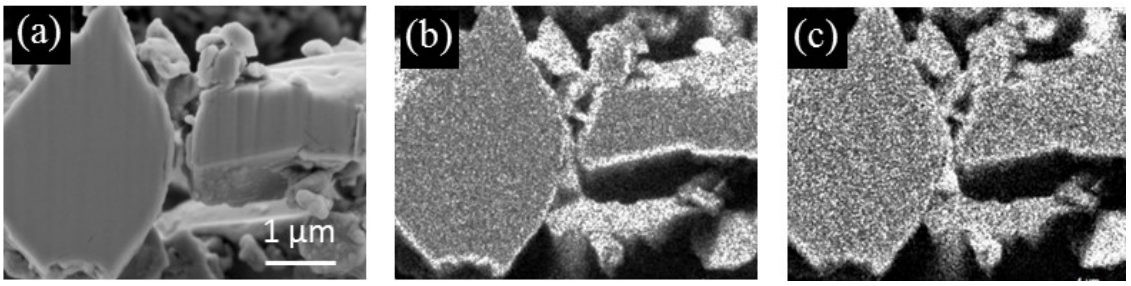

Figure 4.16 Cross-sectional images of the Sm-Fe-Cu-Al coated $Sm_2Fe_{17}N_3$ powder. (a)

SEM-BSE image, (b) EDX Sm-mapping and (c) Cu-mapping. This figure is reproduced from “Coercivity Recovery Effect of Sm-Fe-Cu-Al alloy on $Sm_2Fe_{17}N_3$ Magnet” by Otogawa, K; Asahi, T; Jinno, M; Yamaguchi, W; Takagi, K; Kwon, H. *Journal of the Korean Physical Society* **2018**, in press, Korean Physical Society, copyright 2018.

XPS analysis was performed to collect information about the coated binder layer. Fig. 4.17 shows the XPS spectra of $Sm3d_{5/2}$, $Fe2p_{3/2}$, $Cu2p_{3/2}$ and Al2s acquired from the sputter coated powder. Based on these spectra, the atomic ratio of the surface layer was calculated as Sm : Fe : Cu : Al = 61.8 : 13.5 : 20.5 : 4.2. On the other hand, the composition of the Sm-Fe-Cu-Al mother alloy was Sm : Fe : Cu : Al = 63 : 5 : 22 : 10. That is, the atomic ratio of the surface layer calculated from XPS spectra showed a higher Fe concentration and lower Al concentration than that of the mother alloy. As mentioned above, the thickness of binder layer was not perfectly uniform and the partial thickness was only a few nanometers. Generally, XPS analysis is known to detect photoelectrons emitted from depths of 1 nm to 10 nm. Therefore, the measured atomic ratio of the surface layer might include the atomic information of the $Sm_2Fe_{17}N_3$ phase, resulting in the increase in the Fe ratio. Consequently, while it was difficult to determine the precise atomic ratio of the coating binder layer by XPS analysis, the XPS results suggested that the composition of the coating layer on the $Sm_2Fe_{17}N_3$ grains was at least similar to that of the Sm-Fe-Cu-Al mother alloy.

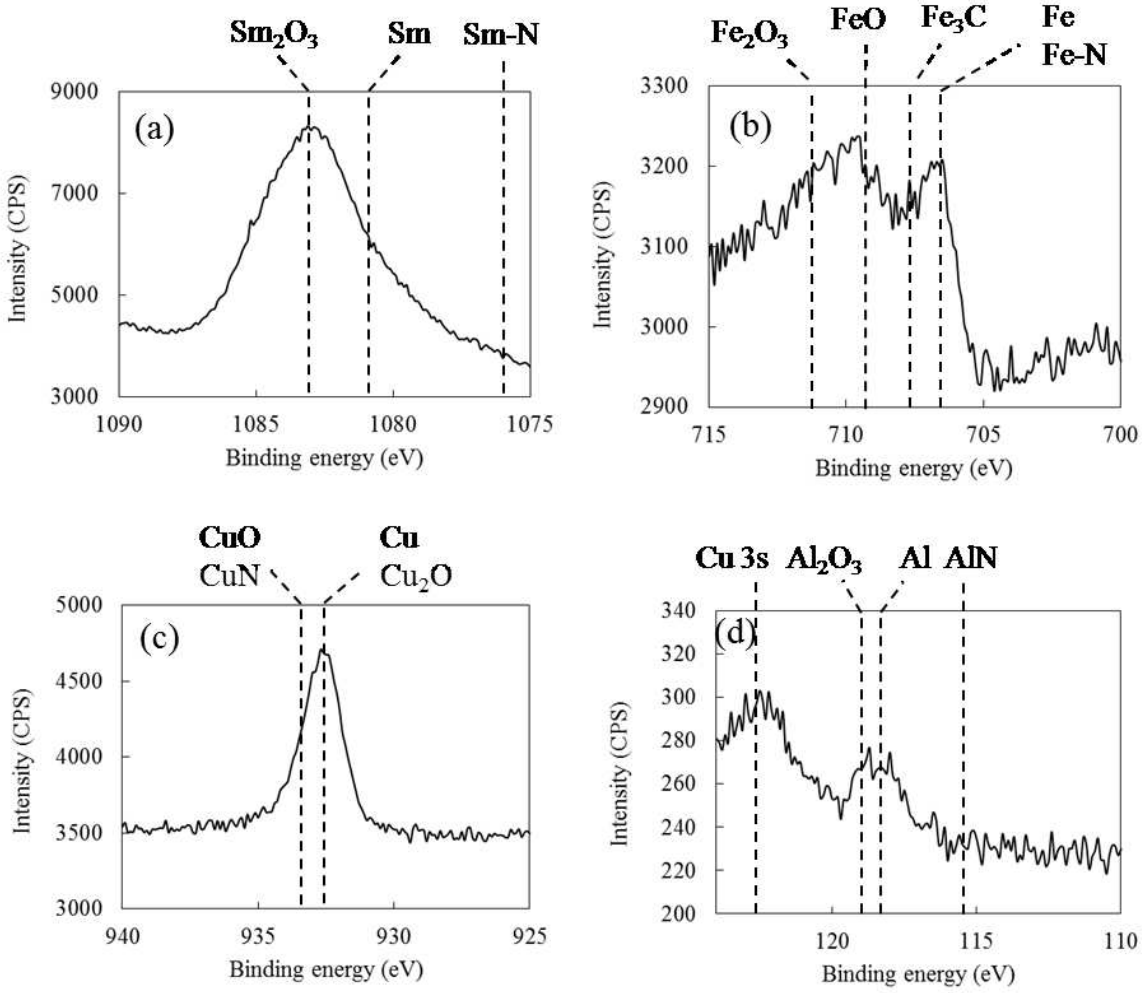

Figure 4.17 XPS profiles of (a) $Sm3d_{5/2}$, (b) $Fe2p_{3/2}$, (c) $Cu2p_{3/2}$ and (d) Al2s for surface of the Sm-Fe-Cu-Al coated $Sm_2Fe_{17}N_3$ powder. This figure is reproduced from "Coercivity Recovery Effect of Sm-Fe-Cu-Al alloy on $Sm_2Fe_{17}N_3$ Magnet" by Otogawa, K; Asahi, T; Jinno, M; Yamaguchi, W; Takagi, K; Kwon, H. *Journal of the Korean Physical Society* **2018**, in press, Korean Physical Society, copyright 2018.

The purpose of sputter coating was to avoid carbonization and nitridization of the added Sm-Fe-Cu-Al alloy. Therefore, the carbonization and nitridization in the binder layer of the sputter coated powder were discussed from the XPS spectra. The values of the binding energies of the compounds which are shown by the broken lines in Fig. 4.17 were taken from the NIST XPS database [6], and that of Sm-N was taken from another reference in the

literature [7]. The peak top of the $Sm3d_{5/2}$ binding energy was determined to be 1083.1 eV, and the peak shape was broadened to the low energy side. Compared with the reference values of metallic Sm and Sm_2O_3, most of the Sm atoms in the coated surface might exist as a Sm oxide. In the preparation of the XPS analysis, the binder-coated powder specimen was transferred from the preservation glove box to the XPS chamber in a transfer vessel to avoid exposure to the air. However, this vessel allows infiltration of slight amount oxygen during transportation. Therefore, the Sm atoms might have been oxidized preferentially before the XPS analysis. Nevertheless, the Sm-N peak (1076 eV) was not observed in the spectrum. This suggested that the Sm atoms in the surface layer were not nitrides. Because the reference value of Sm-C is unreported, the presence of Sm-C could not be identified. Thus, even though carbonization of Sm could not be discussed, it was revealed that Sm was not nitrided during sputtering. The spectrum of $Fe2p_{3/2}$ showed the two peaks at 709.6 and 706.8 eV. Compared with the reference values, the peak of 709.6 eV might be attributed to the peak of FeO, and the peak of 706.8 eV might be attributed to the peak of metallic Fe or Fe-N. The FeO might be derived from oxidation during transportation or from the original surface oxide layer of the raw $Sm_2Fe_{17}N_3$ powder. On the other hand, the peak of 706.8 eV was highly unlikely to be derived from Fe-N, because the XPS spectrum of Sm confirmed no nitridization of Sm, which has higher reactivity than Fe atom. Therefore, the peak of 706.8 eV might be attributed to metallic Fe. Furthermore, as this spectrum showed no peak of Fe_3C, Fe atom might not be carbide. The spectrum of $Cu2p_{3/2}$ showed a single peak at 932.7 eV. Compared with the reference values, this peak might be attributed to the peak of metallic Cu or Cu_2O. Therefore, the Cu atom was expected not to be nitrided. In addition, the literature [8] suggested that the peak of Cu-C is around 933 eV. However, the spectrum of $Cu2p_{3/2}$ showed a single peak without any shoulder peak. Therefore, the Cu might not be carbonized. As the S/N ratio of the spectrum of Al2s was large, peak identification was difficult. However, this spectrum indicated two peaks at 118.2 and 122.5 eV. Compared with the

reference values, the peak of 118.2 eV might be attributed to the peak of metallic Al and the peak of 122.5 eV might be attributed to the peak of the Cu3s. Therefore, the Al was expected not to be nitrided. Because the binding energy of Al-C has not been reported, carbonization of the Al could not be discussed. From the XPS analyses for the four elements, obvious carbonization and nitridization of the coated binder alloy was not found.

4.3.5.2 Evaluation of Sm-Fe-Cu-Al sputter coated $Sm_2Fe_{17}N_3$ sintered compact

Continuously, the binder-coated powder was sintered. At first, to examine the phase transition after sintering, phase identification was conducted by XRD. Fig. 4.18 (a)-(c) showed the XRD profiles of the raw $Sm_2Fe_{17}N_3$ powder, the milled binder-added $Sm_2Fe_{17}N_3$ powder and the binder-coated $Sm_2Fe_{17}N_3$ powder. All the profiles showed only a diffraction peak of the $Sm_2Fe_{17}N_3$ phase. As mentioned in Chapter 3, the diffraction peak of Sm-Cu, which is the main diffraction peak of the Sm-Fe-Cu-Al alloy ingot, is near the $Sm_2Fe_{17}N_3$ peak. Therefore, it is supposed that identification of the diffraction peak derived from the Sm-Fe-Cu-Al alloy was difficult. In any case, however, these results showed no other peaks except $Sm_2Fe_{17}N_3$ peaks. Thus, at least within the range of these XRD results, generation of a new phase by mixing using the dry ball milling method or coating using the sputtering method was not found. Fig. 4.18 (d)-(j) showed the XRD profiles for the compacts sintered from the variously prepared powders at 400 ˚C and 550 ˚C, that is, below and above the melting point of the Sm-Fe-Cu-Al alloy. All the profiles showed only diffraction peaks of the α-Fe and $Sm_2Fe_{17}N_3$ phases. The comparisons of the profiles before and after sintering suggested that no significant phase change except the formation of the α-Fe phase was took place in sintering at both 400 ˚C and 550 ˚C. As precipitation of α-Fe is known to decrease the coercivity of the $Sm_2Fe_{17}N_3$ magnet [4], the α-Fe contents in the sintered compacts were estimated from the peak intensities. The integrated intensities of the (100) peak of α-Fe (52.4°) were determined by an internal reference method with a reference peak of $Sm_2Fe_{17}N_3$

(300) (41.5°). The α-Fe intensity of each sintered compacts increased against the increase of sintering temperature. The intensity ratio of α-Fe of the 400 ˚C sintered compacts was (additive-free sample) : (milled binder-added sample) : (binder-coated sample) = 1: 0.35 : 0.31. In the same way, the peak intensity ratio of the 550 ˚C sintered compacts was (additive-free sample) : (milled binder-added sample) : (binder-coated sample) = 1 : 0.62 : 0.64. The α-Fe intensities of the two types of binder-added compacts that were sintered at 400 ˚C and 550 ˚C were obviously smaller than that of the additive-free compacts. Therefore, the binder-coated sample was also expected to restrain the decrease of coercivity as the milled binder-added sample restrained this property.

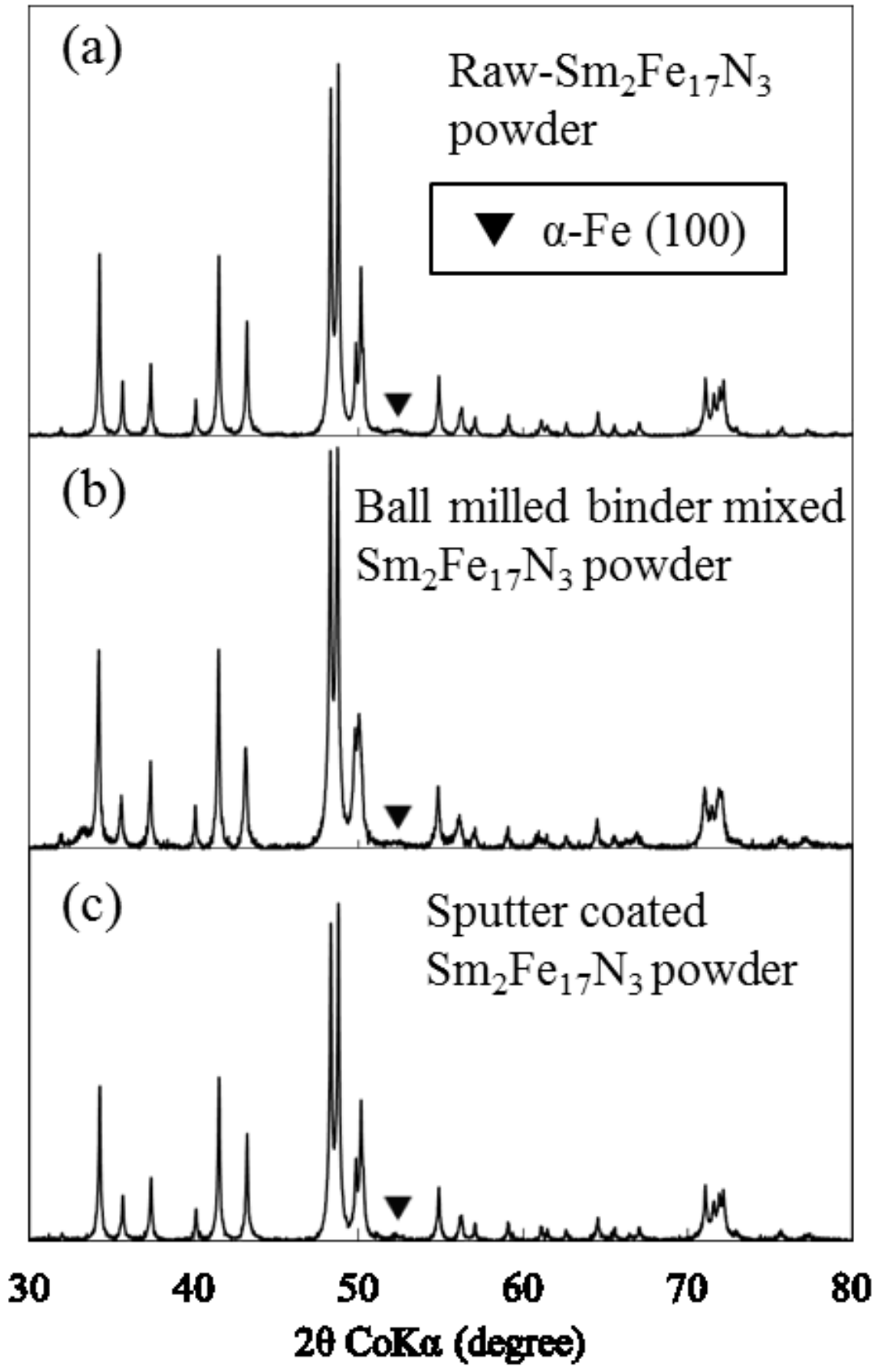
(a)
Raw-Sm2Fe17N3 powder
▼ α-Fe (100)
(b)
Ball milled binder mixed Sm2Fe17N3 powder
(c)
Sputter coated Sm2Fe17N3 powder
30
40
50
60
70
80
2θ CoKα (degree)

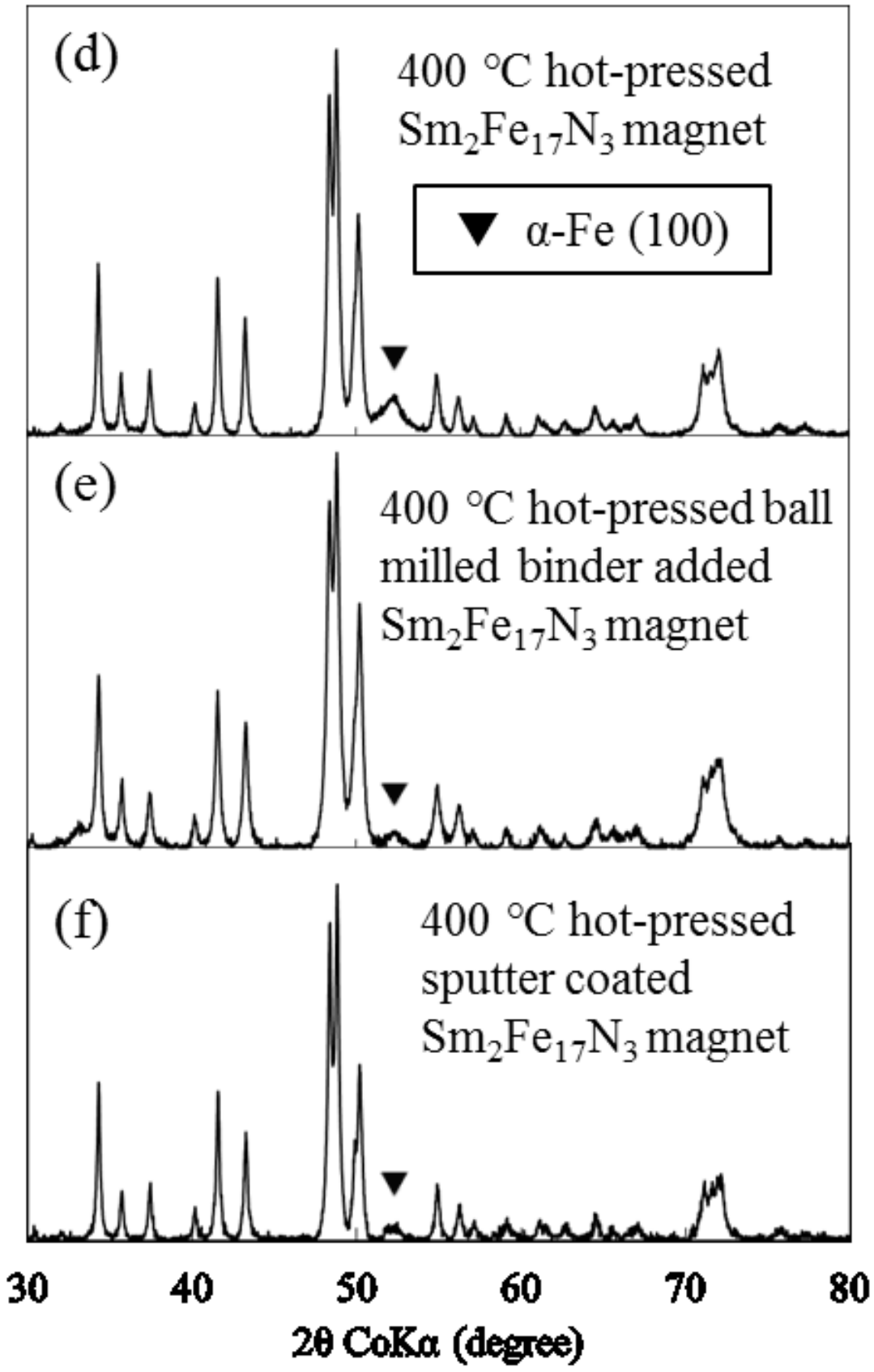
(d)
400 °C hot-pressed
$Sm_2Fe_{17}N_3$ magnet
▼ α-Fe (100)
(e)
400 °C hot-pressed ball
milled binder added
$Sm_2Fe_{17}N_3$ magnet
(f)
400 °C hot-pressed
sputter coated
$Sm_2Fe_{17}N_3$ magnet
30
40
50
60
70
80
2θ CoKα (degree)

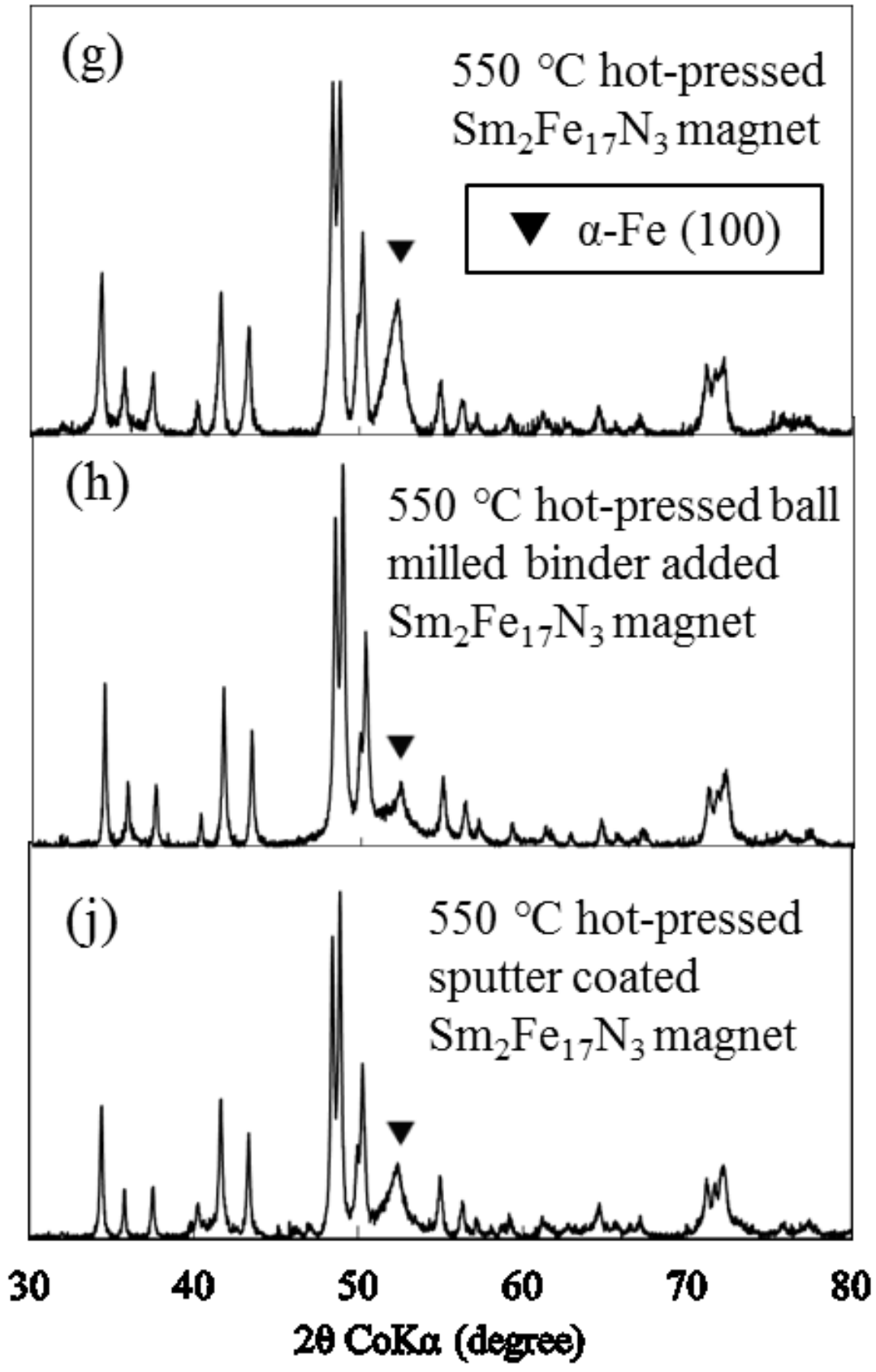

Figure 4.18 XRD profiles for various prepared powders and sintered compacts. (a), (b) and

(c) represent the raw, milled binder-added and binder-coated $Sm_2Fe_{17}N_3$ powders, respectively. (d), (e) and (f) represent $Sm_2Fe_{17}N_3$ compacts that were sintered at 400°C from the raw, milled binder-added and binder-coated $Sm_2Fe_{17}N_3$ powders and (g), (h), and (j) represent the $Sm_2Fe_{17}N_3$ compacts that were sintered at 550°C from the raw and milled binder-added and binder-coated $Sm_2Fe_{17}N_3$ powders. This figure is reproduced from "Coercivity Recovery Effect of Sm-Fe-Cu-Al alloy on $Sm_2Fe_{17}N_3$ Magnet" by Otogawa, K; Asahi, T; Jinno, M; Yamaguchi, W; Takagi, K; Kwon, H. *Journal of the Korean Physical Society* **2018**, in press, Korean Physical Society, copyright 2018.

As shown in Fig. 4.19, the dependence of coercivity on the sintering temperature of the binder-coated $Sm_2Fe_{17}N_3$ compacts was compared to those of the milled binder-added and additive-free compacts. As expected, the binder-coated samples had higher coercivity than the additive-free samples, but the coercivity recovery effect was not large as that of the milled binder-added samples. A comparison of the recovered coercivity of the two types of powders was shown in Fig. 4.20. The coecivity recovered amount was defined as subtraction value of the coercivity of the additive-free $Sm_2Fe_{17}N_3$ compact from that of the binder-added $Sm_2Fe_{17}N_3$ compact sintered at arbitrary temperature. Actually, the milled binder-added samples showed higher recovery amount of coercivity than the binder-coated samples. Simply considered, the reason for this was the fact that the binder-coated samples contained a smaller amount of binder alloy than the milled binder-added samples.

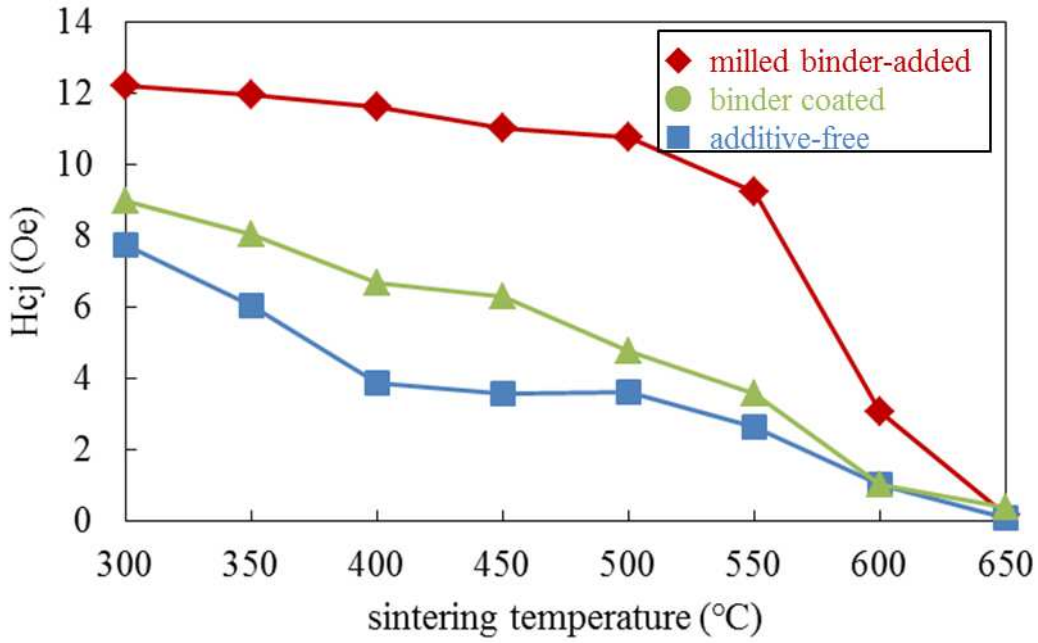

Figure 4.19 Dependence of coercivity on the sintering temperature of the wet ball milled binder-added (red), binder-coated (green) and additive-free (red) $Sm_2Fe_{17}N_3$ sintered compacts. This figure is reproduced from "Coercivity Recovery Effect of Sm-Fe-Cu-Al alloy on $Sm_2Fe_{17}N_3$ Magnet" by Otogawa, K; Asahi, T; Jinno, M; Yamaguchi, W; Takagi, K; Kwon, H. *Journal of the Korean Physical Society* **2018**, in press, Korean Physical Society, copyright 2018.

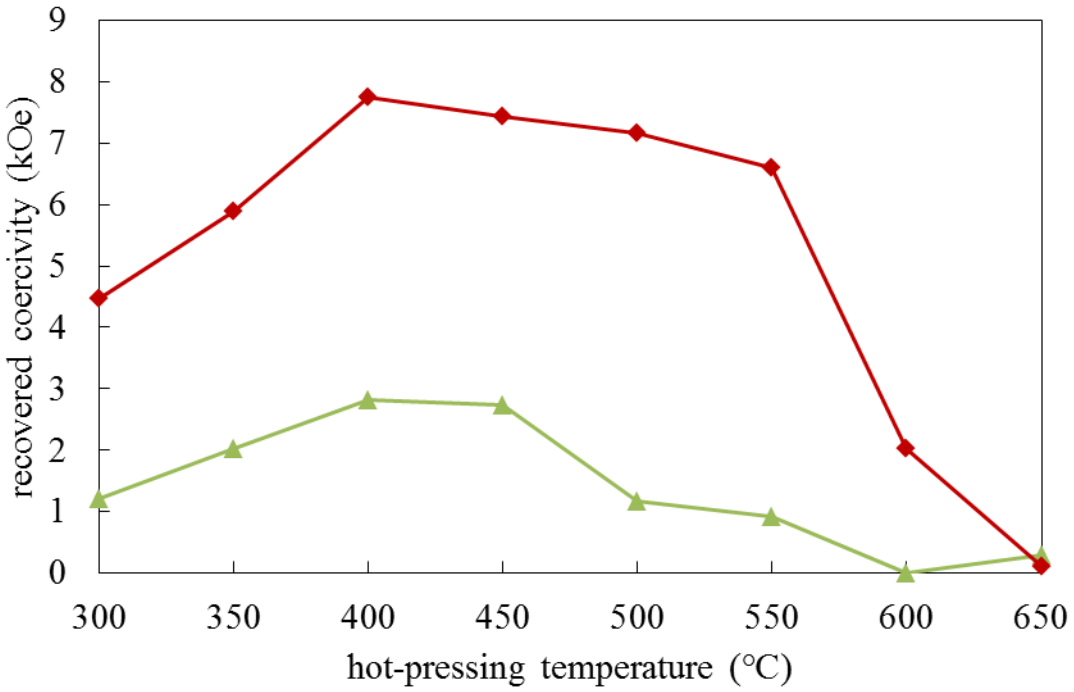

Figure 4.20 Dependence of recovered coercivity on the sintering temperature of the milled binder-added (red) and binder-coated (green) $Sm_2Fe_{17}N_3$ sintered compacts. This figure is reproduced from "Coercivity Recovery Effect of Sm-Fe-Cu-Al alloy on $Sm_2Fe_{17}N_3$ Magnet" by Otogawa, K; Asahi, T; Jinno, M; Yamaguchi, W; Takagi, K; Kwon, H. *Journal of the Korean Physical Society* **2018**, in press, Korean Physical Society, copyright 2018.

To compare the coercivity recovery effect between the milled binder-added and binder-coated sampled by the same standard, the coercivity recovery amount was calculated for the case of a 1nm thick binder layer. Assuming that the binder uniformly surrounded the surface of spherical $Sm_2Fe_{17}N_3$ grains with a diameter of 3 μm, the thicknesses of the binder layers of the milled binder-added and binder-coated compacts were calculated to be 130 nm and 18 nm, respectively. The recovered coercivity values indicated in Fig. 4.20 were divided by these thickness values, and the result was defined as the recovered coercivity per nanometer of thickness of the binder layer (simply called "recovery rate" in the following). Fig. 4.21 compares the dependency of the recovery rate on the sintering temperature between the milled binder-added and binder-coated samples. With the sintering temperature of 450°C,

the recovery rate of the binder-coated samples was larger than that of the milled binder-added samples. This suggested that a binder which is free from carbonization and nitridization can recover coercivity more effectively. Hence, if carbonization and nitridization are constrained, the necessary amount of binder to produce a high coercive $Sm_2Fe_{17}N_3$ magnet can be reduced.

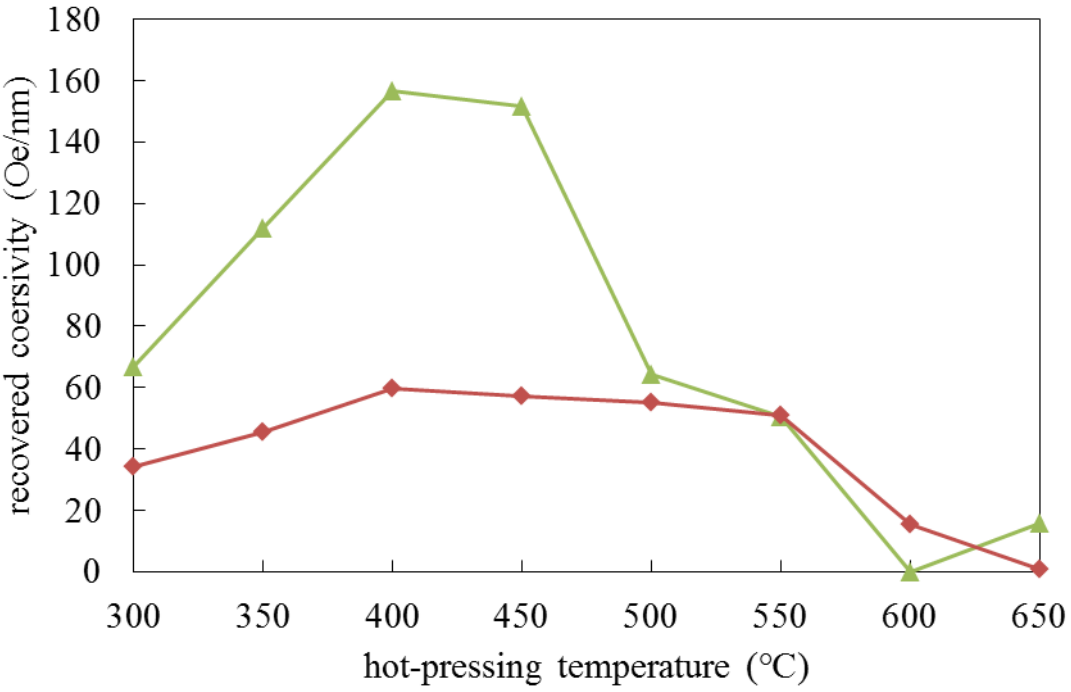

Figure 4.21 Dependence of coercivity recovery rate on the sintering temperature of the milled binder-added (continuous line) and binder-coated (broken line) $Sm_2Fe_{17}N_3$ sintered compacts.

On the other hand, with the compact that was sintered from the binder-coated powder at 500°C, the recovery rate dropped to the same level as the compact produced from the milled binder-added powder. Conversely, the recovery rates of the milled binder-added samples were almost constant up to a sintering temperature of 550°C. These differences in the tendency of the recovery rate are interesting.

A hypothesis to explain these tendencies of the recovery rate is proposed as follows. The metallic Sm in the Sm-Fe-Cu-Al binder naturally has high reactivity. The coercivity recovery effect is observed even when the sintering temperature is lower than the melting temperature of the Sm-Fe-Cu-Al alloy. Since Sm atoms have a high reduction ability, the coercivity recovery effect is presumed to occur because the Sm atoms in the alloy deprive the surface oxide layer of oxygen atoms, and then break up or absorb the oxide layer. The amount of absorbed oxygen might increase as the concentration of unreacted Sm atoms in the binder phase increases. The sputter-coated binder layers must contain a large amount of Sm atoms because the binder layers are neither carbonized nor nitrided. Therefore, the sputter-coated binder layers might remove a large amount of oxygen from the surface of the $Sm_2Fe_{17}N_3$ grains. As a result, the binder-coated powder might exhibit a high coercivity recovery rate at temperatures up to 450°C, as shown in Fig. 8. In the case of the sintering temperatures above 500°C, the coated binder layer might melt into a liquid phase because it did not undergo carbonization or nitridization, and thus retained its original melting temperature of 495°C. Because the diffusion velocity of oxygen atoms in the liquid phase is supposed to be much higher than that in the solid phase, the liquid binder phase might take in a further amount of oxygen atom compared with the solid state of the binder phase. However, because the binder additive ratio of the sputter-coated powder was only 3.4 wt%, rapid absorption of oxygen by the formation of the liquid phase might drastically increase consumption of unreacted Sm. If it reaches this state, the α-Fe phase precipitates derived from the oxidation-reduction reaction can no longer be restrained, resulting in the rapid decrease in the coercivity recovery rate at 500°C. On the other hand, the recovery rate of the milled binder-added samples did not show strong dependency on the sintering temperature. Because the composition shift due to carbonization and nitridization results in a higher melting point, the milled binder layer does not form a liquid phase even above 500°C. Therefore, the binder layer exists as a solid phase in the whole temperature range, resulting in the constant recovery rate.

In addition, the sputter-coated binder is also expected to facilitate densification of the $Sm_2Fe_{17}N_3$ powder because the binder layer forms a liquid phase. At the sintering temperature of 400°C, the absolute density of the binder-coated sample, 5.97 g/cm^3, was lower than that of the additive-free $Sm_2Fe_{17}N_3$ sample, 6.36 g/cm^3. However, when the sintering temperature was raised to 550°C, i.e., above the melting point of the binder, the binder-coated sample exhibited a higher density of 6.61 g/cm^3 than the additive-free sample, 6.45 g/cm^3. Therefore, this binder has the potential for promoting densification of the $Sm_2Fe_{17}N_3$ powder. Further examination, including a comparison of relative density, will be necessary, in order to recognize the densification promotion effect of the Sm-Fe-Cu-Al alloy. This will require the development of a method that enables easier preparation of binder-added powders with various binder contents than is possible by the sputtering method. Nevertheless, from the standpoints of both the coercivity recovery effect and the densification promotion effect, it is essential to develop a process that makes it possible to add a sufficient amount of Sm-Fe-Cu-Al binder without carbonization and nitridization. Although the sputtering method is an ideal way to add a contamination-free binder, it is unfavorable from the viewpoint of throughput.

4.4 Conclusion

The purpose of this chapter was to clarify the potential of the Sm-Fe-Cu-Al alloy binder to improve the magnetic properties of the $Sm_2Fe_{17}N_3$ sintered magnet, and in particular, the coercivity recovery effect of this binder. As shown in Chapter 3, the Sm-Fe-Cu-Al alloy powder, which was pulverized by wet ball milling, restrained the coercivity decrease of $Sm_2Fe_{17}N_3$ powder during sintering. TEM observation of the wet ball milled binder-added $Sm_2Fe_{17}N_3$ sintered compact suggested that the Sm-Fe-Cu-Al binder had the effect of removing the surface oxide layer of the $Sm_2Fe_{17}N_3$ grains. It was presumed that the removal of the surface oxide restrained precipitation of the α-Fe phase by the redux reaction around the surface oxide layer, and as a result, the binder-added $Sm_2Fe_{17}N_3$ compact might restrain the coercivity decrease during sintering. On the other hand, it was also found that pulverization with wet ball milling gave rise to carbonization and nitridization of the Sm-Fe-Cu-Al alloy by the organic solvent used as a pulverization medium. Therefore, pulverizing of Sm-Fe-Cu-Al alloy with jet milling was attempted to prevent carbonization and nitridization of the binder alloy. However, the jet milled binder powder was slightly carbonized and nitride by organic medium which is necessary to avoid aggregation of pulverized particles. The coercivities of the jet milled binder-added $Sm_2Fe_{17}N_3$ sintered compacts were lower than that of wet ball milled binder-added sintered compacts. On the other hand, this jet milled binder powder gives valuable knowledge that to disperse the binder alloy homogeneously in grain boundary of sintered compact, shape of pulverized binder powder is important: platelike shape is better than spherical shape. Continuously, to avoid contamination from the organic medium used in pulverization, the Sm-Fe-Cu-Al alloy was directly coated on the surface of the raw $Sm_2Fe_{17}N_3$ particles by sputtering method. XPS analysis suggested no carbide and nitride in the coated binder. The recovered coercivity per unit binder thickness was significantly improved by using the binder-coated $Sm_2Fe_{17}N_3$ powder. In addition, the absolute densities of the sintered compacts were improved by

Sm-Fe-Cu-Al binder. Thus, it was implied that sufficient addition of a contamination-free Sm-Fe-Cu-Al binder has the potential to reduce the amount of binder which is necessary to produce a high coercive and dense $Sm_2Fe_{17}N_3$ magnet.

4.5 References

[1] M. Katter, J. Wecker, C. Kuhrt, L. Schultz, R. Grössinger, Magnetic properties and thermal stability of Sm2Fe17Nx with intermediate nitrogen concentrations, Journal of Magnetism and Magnetic Materials. 117 (1992) 419–427. doi:10.1016/0304-8853(92)90099-A.

[2] K. Kobayashi, Q. Qi, J.M.D. Coey, Magnetic properties of partially oxidized Sm 2Fe17 Nx, J Magn Magn Mater. 144 (1995) 1077–1078.

[3] C.N. Christodoulou, N. Komada, High coercivity anisotropic Sm2Fe17N3 powders, Journal of Alloys and Compounds. 222 (1995) 92–95. doi:10.1016/0925-8388(94)04924-6.

[4] K. Takagi, H. Nakayama, K. Ozaki, Microstructural behavior on particle surfaces and interfaces in Sm2Fe17N3 powder compacts during low-temperature sintering, Journal of Magnetism and Magnetic Materials. 324 (2012) 2336–2341. doi:10.1016/j.jmmm.2012.02.021.

[5] K. Kobayashi, T. Iriyama, T. Yamaguchi, H. Kato, Y. Nakagawa, Magnetic properties of the single magnetic domain particles of Sm2Fe17Nx compounds, Journal of Alloys and Compounds. 193 (1993) 235–238. doi:10.1016/0925-8388(93)90357-S.

[6] NIST, NIST X-ray Photoelectron Spectroscopy Database, NIST Standard Reference Database 20, Version 4.1. http://srdata.nist.gov/xps/Default.aspx, [Žiūrėta: 2017-05-20]. (2017). http://srdata.nist.gov/xps/Default.aspx.

[7] K.H. Goh, A.S.M.A. Haseeb, Y.H. Wong, Structural characteristics of samarium oxynitride on silicon substrate, Journal of Alloys and Compounds. 722 (2017) 729–739. doi:10.1016/j.jallcom.2017.06.179.

[8] B. Balamurugan, B.R. Mehta, S.M. Shivaprasad, “Nanoparticle route” for the synthesis of a stable and stoichiometric Cu2C2 phase - A semiconductor material, Applied Physics Letters. 82 (2003) 115–117. doi:10.1063/1.1533852.

Chapter 5

Summary and Future Prospects

5.1 Summary

In this theses, new sintering process for $Sm_2Fe_{17}N_3$ using Sm-based eutectic alloy as binder which is capable of preventing the coercivity decrease during sintering as well as facilitating densification due to the same effect as liquid phase sintering was explored.

In chapter 2, low-melting point Sm-based eutectic alloy for sintering binder of $Sm_2Fe_{17}N_3$ was developed. Quaternary $Sm_{63}Fe_5Cu_{22}Al_{10}$ alloy was found to have very low melting temperature of 495°C, which is more than 100°C lower than the thermal decomposition temperature of $Sm_2Fe_{17}N_3$. Therefore, the Sm-Fe-Cu-Al alloy was expected to suitable as a binder for $Sm_2Fe_{17}N_3$ sintered magnet.

In chapter 3, to reveal the effect of the Sm-Fe-Cu-Al binder alloy on the magnetic properties of the $Sm_2Fe_{17}N_3$ sintered compacts, Sm-Fe-Cu-Al bonded $Sm_2Fe_{17}N_3$ sintered compacts were produced and those properties were evaluated. At first, the Sm-Fe-Cu-Al alloy was pulverized into fine powder with wet ball milling method. The Sm-Fe-Cu-Al fine powder was mixed with raw $Sm_2Fe_{17}N_3$ powder and sintered at various sintering temperatures. While the conventional Zn binder decreased the saturation magnetization of sintered compacts due to an excess reaction with $Sm_2Fe_{17}N_3$ phase, the developed Sm-Fe-Cu-Al binder did not affect the magnetization of the $Sm_2Fe_{17}N_3$ sintered compacts adversely. Furthermore, conventional sintering of $Sm_2Fe_{17}N_3$ powder has always resulted in a serious decrease in coercivity against rising sintering temperature, but the binder-added sintered compacts maintained the coercivity of the raw powder over a wide range of sintering temperatures. The main cause of this coercivity maintenance effect was probably due to restrain of α-Fe precipitation by the Sm-Fe-Cu-Al binder.

In chapter 4, the potential of the Sm-Fe-Cu-Al binder for improvement of the magnetic properties of $Sm_2Fe_{17}N_3$ was examined. TEM observation of the wet ball milled binder-added $Sm_2Fe_{17}N_3$ sintered compact, which was prepared in chapter 3, suggested that the Sm-Fe-Cu-Al binder had the effect of removing the surface oxide layer of the $Sm_2Fe_{17}N_3$ grains. It was presumed that the removal of the surface oxide restrained precipitation of the α-Fe phase by the redux reaction around the surface oxide layer, and as a result, the binder-added $Sm_2Fe_{17}N_3$ compact might restrain the coercivity decrease during sintering. On the other hand, it was also found that pulverization with wet ball milling gave rise to carbonization and nitridization of the Sm-Fe-Cu-Al alloy by the organic solvent used as a pulverization medium. To avoid contamination from the organic medium used in pulverization, the Sm-Fe-Cu-Al alloy was directly coated on the surface of the raw $Sm_2Fe_{17}N_3$ particles by sputtering method. The recovered coercivity value per unit binder thickness was significantly improved by using the binder-coated $Sm_2Fe_{17}N_3$ powder. In addition, the absolute densities of the sintered compacts were improved by Sm-Fe-Cu-Al binder

From the above results, it was implied that sufficient addition of a contamination-free Sm-Fe-Cu-Al binder has the potential to reduce the amount of binder necessary to produce a high coercive and dense $Sm_2Fe_{17}N_3$ magnet.

5.2 Future prospects

There are some remained issues to make proposed sintered process practical operation. Major remained issue is that we have to develop a method that enables easier preparation of binder-added powders with various binder contents than is possible by the sputtering method. Nevertheless, from the standpoints of both the coercivity recovery effect and the densification promotion effect, it is essential to develop a process that makes it possible to add a sufficient amount of Sm-Fe-Cu-Al binder without carbonization and nitridization.

Although the sputtering method is an ideal way to add a contamination-free binder, it is unfavorable from the viewpoint of throughput. In addition, the composition of Sm-based alloy has room for consideration. This thesis only focused on lowering melting temperature of Sm-based alloys. However, we should explore other elements to improve magnetic properties of $Sm_2Fe_{17}N_3$ magnet. I believe that further development of the proposed sintering process will realize Dy-free high-performance permanent magnet which surpasses Dy-doped $Nd_2Fe_{14}B$ magnet.

Academic Achievement

Scientific Publication List

○Kohei Otogawa, Kenta Takagi, Toru Asahi, Consolidation of $Sm_2Fe_{17}N_3$ magnets with Sm-based eutectic alloy binder, Journal of Alloys and Compounds, 746C (2018) 19-26.

○Kohei Otogawa, Miho Jinno, Wataru Yamaguchi, Kenta Takagi, Toru Asahi, Hansang Kwon, Coercivity Recovery Effect of Sm-Fe-Cu-Al Alloy on $Sm_2Fe_{17}N_3$ Magnet, Journal of the Korean Physical Society, in press.

Presentations in Scientific Meetings

International Meetings

Kohei Otogawa, Masahito Tanaka, Hiroshi Ogawa, Hiromi Kashiwaya, Hiroyuki Toyokawa, Kenta Takagi, Kimihiro Ozaki, Toru Asahi, Development of magnetic domain observation technique for Sm-Fe-N sintered magnet with photo-emission electron microscope, REPM2016, Darmstadt, Germany, August 2016. (Poster)

Domestic Meetings

乙川光平，高木健太，朝日透，「Sm 基共晶合金をバインダーとした $Sm_2Fe_{17}N_3$ 磁粉の焼結」，粉体粉末冶金協会平成 29 年度秋季大会，京都，2017 年 11 月. (Oral)

乙川光平，田中真人，小川博嗣，柏谷裕美，豊川弘之，高木健太，尾崎公洋，朝日透，「MCD-PEEM による Sm-Fe-N 焼結磁石の磁区観測手法の開発」，粉体粉末冶金協会平成 28 年度春季大会，京都，2016 年 5 月. (Oral)

田中真人，小川博嗣，乙川光平，豊川弘之，高木健太，尾崎公洋，「磁石高性能化の

ための円二色性光電子顕微鏡の開発と磁区観察」，産総研分析計測標準研究部門第 1 回シンポジウム，東京，2015 年 9 月. (Poster)

Acknowledgement

First of all, I would like to express my sincere gratitude to my supervisor Prof. Toru Asahi, belonging to Department of Life Science and Medical Bioscience and Department of Advanced Science and Engineering in Waseda University, during 2012-2018. He is the first person to tell me how interesting scientific research is. My step to the researcher had started from meeting with him. Furthermore, he allowed my selfish request to research at National Institute of Advanced Industrial Science and Technology (AIST). Because he had such a generous heart, I got to where I am now. He always gave me a great support about not only research but also my career. Owing to his effort, I could do the internship in the major company and I could get the job. I am really glad that I could join his laboratory.

My sincere thanks also go to Dr. Kenta Takagi in Magnetic Powder Metallurgy Research Center of AIST. At first, he willingly accepted me to his group. Whereas I was outsider of metallurgical engineering, he politely taught me basic of sintering and magnets. Because he gave me a great research subject; development of $Sm_2Fe_{17}N_3$ magnet, I could realize the pleasure of development for practice applications. I could experience the short term study at Pukyong National University due to his introduction. Furthermore, he rapidly checked my presentation materials and academic paper even on weekend. I could not meet such a kind person. I am terribly sorry that I could not meet his expectations although he evaluates me highly. His research attitude, management ability, consideration to subordinate and so on is very beneficial for me. He will be my ideal image of boss in my future career. I really respect him as one of the best scientific researchers.

I am grateful to Prof. Hansang Kwon in Pukyong National University. He willingly accepted me to short term study at his laboratory. His surpassing knowledge about sintering gratefully refines my academic paper. Also, I would to thank him to be members on judging committee for the doctoral thesis.

I would like to also thank Prof. Takuro Katsufuji for welcoming my lab-rotation work at his laboratory and his sincere efforts as members on judging committee for the doctoral thesis.

I would like to also thank Prof. Makoto Tanaka in AIST. He introduced me the research of $Sm_2Fe_{17}N_3$. If he was not acquainted with Prof. Asahi, I could not write this thesis. Incidentally, I would like to thank his colleagues in Tsukuba. They told me how I should behave as a researcher.

I would like to also thank Wataru Yamaguchi (AIST), Miho Jinno (AIST) for their help on my research during my short term study in Pukyong National University.

I would like to also thank all members of Takagi laboratory for warm acceptance of me as one of laboratory member. The memories of life in Chubu center are my precious treasures.

I would like to also thank Dr. Kimihiro Ozaki (AIST) and Dr. Asaya Fujita for having lunch together every day. Their conversation sometime developed my knowledge about research of magnets.

I would like to also thank members of Kwon laboratory for their all assistance of the works and cultural experiences during my short term study in Pukyoung National University.

I would like to express special thanks to Mr. Masuyama (Mitsubishi Material Co., Ltd.) for very kind teaching during my internship. I made him work hard but he never showed tiresome face. I'm looking forward to research with him.

I would like to also thank staff of leading program for processing my numerous unreasonable offers.

I am also grateful to lab members and staffs in Asahi laboratory. They always support me and often took place enjoyable events. I spend great time at Asahi laboratory.

Finally, I am really grateful to my parents, Mr Katsuyuki Otogawa, Mrs. Yuko Otogawa, and my sister Ms. Yuka Otogawa. They allowed my selfishness and always support me. Owing to their special support, I could find what I want to do in my life.